

Die approbierte Originalversion dieser Dissertation ist an der Hauptbibliothek der Technischen Universität Wien aufgestellt (<http://www.ub.tuwien.ac.at>).

The approved original version of this thesis is available at the main library of the Vienna University of Technology (<http://www.ub.tuwien.ac.at/englweb/>).



TECHNISCHE
UNIVERSITÄT
WIEN
Vienna University of Technology

DISSERTATION

Molecular Dynamics Evidence of a Three-term Kinetic Friction Law for Mixed- and Boundary-lubricated Nanotribological Systems

ausgeführt zum Zwecke der Erlangung des akademischen Grades eines
DOKTORS DER TECHNISCHEN WISSENSCHAFTEN
unter der Leitung von

Ao.Univ.-Prof.i.R. Dr.phil. **Gerhard Betz**
E 134 - Institut für Angewandte Physik
und

Priv.-Doz. Dr.rer.nat. Dipl.-Phys. **András Vernes**
E134 - Institut für Angewandte Physik

eingereicht an der Technischen Universität Wien
Fakultät für Physik

von

Dipl.-Ing. **Stefan Eder**
Matrikelnummer: 9625614
Graf Starhemberg Gasse 29/23, 1040 Wien

Wien, im Juni 2012



TECHNISCHE
UNIVERSITÄT
WIEN
Vienna University of Technology

DISSERTATION

**Molecular Dynamics Evidence of a
Three-term Kinetic Friction Law for
Mixed- and Boundary-lubricated
Nanotribological Systems**

submitted in partial fulfillment of the requirements for the degree of
DOCTOR OF TECHNICAL SCIENCES
under the supervision of

Ao.Univ.-Prof.i.R. Dr.phil. **Gerhard Betz**
E134 - Institute of Applied Physics
and

Priv.-Doz. Dr.rer.nat. Dipl.-Phys. **András Vernes**
E134 - Institute of Applied Physics

at the Vienna University of Technology
Faculty of Physics

by

Dipl.-Ing. **Stefan Eder**
Matriculation No.: 9625614
Graf Starhemberg Gasse 29/23, 1040 Wien

Vienna, June 2012

Kurzfassung

In dieser Arbeit wird ein neues kinetisches Nano-Reibgesetz mit drei Termen vorgestellt und verifiziert. Es beinhaltet den Amontons-Coulomb Term, der den lastabhängigen Beitrag, und den Bowden-Tabor Term, der den haftungsabhängigen Beitrag zur Reibkraft beschreibt, sowie den lastunabhängigen sogenannten Derjaguin-Offset, der durch die Adhäsion im Schmierstoff bedingt ist. Das Reibgesetz reproduziert Nichtlinearitäten und Diskontinuitäten im Last-gegen-Reibkraft Verhalten, die man üblicherweise beobachtet, wenn atomistische Tribosysteme unter Mischreibungsbedingungen geschert werden. Die direkte Festkörperkontaktfläche, die zwischen zwei rauen Festkörperoberflächen entsteht, wenn der Schmierfilm versagt, wird mittels eines selbst entwickelten Smooth Particle (SPM) Ansatzes berechnet, der es erlaubt, diskrete Daten von Molekulardynamik (MD) Simulationen ins Kontinuum abzubilden. Diese SPM+MD Methode wurde erfolgreich angewandt, um den Einlaufvorgang von Nanotribosystemen zu analysieren, die anfangs stark ausgeprägten direkten Festkörperkontakt zeigen, welcher gegen Ende fast vollends verschwindet. Weiters wurde der Versuch unternommen, bei Systemen unter Grenzreibungsbedingungen ohne direkten Festkörperkontakt den Derjaguin-Offset mit dem Grad der Unordnung im Schmierstoff in Relation zu setzen. Diese Unordnung wird durch die konfigurationelle Entropie quantifiziert und mit einem Makromolekül-Ansatz abgeschätzt, der auf Kovarianz(super)matrizen der Kohlenstoffatome im Schmierstoff beruht. Das Hauptresultat dieser Arbeit ist, dass die Reibzahl ihre makroskopische Bedeutung verliert, d.h. sie kann nicht als Verhältnis der Reibkraft zur Last berechnet werden, wenn die Schmierpaltdicke auf wenige Monolagen von Schmierstoffmolekülen reduziert wird, was letztlich zum Versagen des Schmierstoffs und damit zu direktem Festkörperkontakt führen kann. Allerdings können mit der Reibzahl, der effektiven Scherfestigkeit und dem Derjaguin-Offset, die aus dem vorgestellten Reibgesetz folgen, drei lastunabhängige Systemparameter angegeben werden, welche eindeutig die tribologische Reaktion von Nanosystemen charakterisieren.

Abstract

In this work a three-term kinetic friction law at nanoscale is proposed and proven to hold. It includes the Amontons-Coulomb term describing the load-controlled contribution and the Bowden-Tabor term providing the adhesion-controlled contribution to the friction force, as well as the load-independent Derjaguin-offset ascribed to adhesion in the lubricant. The proposed law can reproduce the non-linearities and discontinuities in the load-vs.-friction behavior commonly encountered when shearing atomistic tribological systems under mixed lubrication conditions. The solid-solid contact area occurring between two rough solid surfaces when the lubrication film fails is calculated using a self-developed smooth particle approach (SPM) which allows one to map the discrete data obtained from molecular dynamics (MD) simulations to continuum. This MD+SPM method is successfully applied to analyze the run-in period of nanotribological systems exhibiting strong solid-solid contact at the beginning and almost none at the end. Furthermore, an attempt is made to relate the Derjaguin-offset in boundary lubricated systems without solid-solid contact to the degree of disorder in the lubricant, which is quantified by its configurational entropy and estimated using the single macromolecule approach based on covariance (super)matrices of the carbon backbone atoms in the lubricant. The main finding of this work is that the coefficient of friction loses its macroscopic meaning, i.e., it cannot be identified with the friction force per applied load as the lubrication gap thickness decreases to a few monolayers of lubricant molecules, which eventually may lead to lubricant failure and subsequent solid-solid contact. However, the coefficient of friction, effective shear strength, and Derjaguin-offset following from the proposed three-term kinetic friction law constitute the three load-independent system parameters which uniquely characterize the tribological response of nanosystems.

To Claudia and Gwen with love

Acknowledgement

I would like to start by thanking my supervisor Gerhard Betz for his continued support, his relaxed nature, and his tricky questions. In addition to our biweekly professional discussions and the sharing of each other's travel stories, I learned a lot from the way he faced adversity at a time when we thought we were going to lose him.

My colleague and second supervisor András Vernes and I didn't hit it off too well at the beginning. It took us about two years to get used to the other's madness, but it was a one-week business trip together that eventually showed us how well we complement each other scientifically while having fun along the way. His research ideas, among which was the bit about the configurational entropy featured in this thesis, will probably keep me busy until my retirement. His fine eye for detail has saved me from many stupid mistakes, and his smoking breaks gave me the chance to think up and formulate my counterarguments. Thank you, András, for your hand in producing this work.

A big thank you goes out to the simulation group at AC²T. Many of the people I work with every day have become friends rather than just colleagues. Our group leader Georg Vorlauffer seems to know something about pretty much everything, and whenever I was stuck with a problem, he would usually jot down a couple of formulas and hints on a piece of scrap paper and get me back on track within 10 minutes. My two closest colleagues Davide Bianchi and Sladjan Ilincic are not only helpful whizzes at what they do (whatever that may be), but have also become a part of my private life aside from physics and tribology. Way to go, dudes! I would also like to thank Nikolaj Kundtner for his painstaking effort to visualize and animate the Voronoi-tessellations.

This work was funded by the Austrian "Kplus-Program" and carried out at the "Austrian Center of Competence for Tribology" (AC²T).

Contents

Introduction	1
1 Classical Molecular Dynamics (MD)	5
1.1 Newtonian Dynamics of Atoms	5
1.2 Interaction Potentials	7
1.2.1 Lennard-Jones potential	7
1.2.2 Interaction potentials for metals	8
1.2.3 Interaction potentials for molecules	9
1.3 Integrators	11
1.3.1 Basic and velocity Verlet algorithm	12
1.3.2 rRESPA multi-timescale scheme	13
1.4 Thermostats	14
1.4.1 Temperature of MD systems	14
1.4.2 A simple thermostat	15
1.4.3 Langevin thermostat	15
1.5 Boundary Conditions	16
1.6 LAMMPS	16
2 MD-setup of Nanosystems	19
2.1 System Components	19
2.1.1 Substrate	19
2.1.2 Lubricants	23
2.2 Assembly of a Tribosystem	26
2.2.1 Lubricant coverage	26
2.2.2 Lubricant equilibration	27
2.2.3 Compression	29
2.2.4 Shear	31
3 Analysis Methods	33
3.1 Smooth Particle Post-processing (SPM)	33
3.1.1 SPM basics	34
3.1.2 Determination of SPM-parameters	37

3.1.3	Estimation of the asperity contact area	37
3.1.4	Contact atom counting procedure (CCP)	39
3.1.5	Voronoi tessellation versus SPM	44
3.2	Asperity Deformation During Solid-solid Contact	49
3.3	Contact Force Averaging and Error Estimation	50
3.3.1	Filtering methods	50
3.3.2	Statistical inefficiency	51
3.3.3	Time dependence of contact force	51
3.4	Constitutive System Parameters	54
3.4.1	Three-term kinetic friction law	54
3.4.2	Least squares fitting procedure	55
3.4.3	Convergence of constitutive system parameters	57
3.5	Lubricant Analysis	58
3.5.1	Dynamic cross-correlation maps (DCCM)	60
3.5.2	Configurational entropy	61
4	Results and Discussion	67
4.1	SPM Analysis of Boundary Lubricant Failure	67
4.1.1	Specific system setup	67
4.1.2	Time-dependence of friction force	69
4.1.3	Asperity contact area	69
4.1.4	Cavities	72
4.1.5	Three-term kinetic friction law	74
4.2	Simulation of Nanoscopic Run-in	78
4.2.1	Specific system setup	78
4.2.2	Asperity contact area	78
4.2.3	Asperity deformation	81
4.2.4	Constitutive system parameters	88
4.3	Linking the Derjaguin-offset to Lubricant Disorder	93
4.3.1	Specific system setup	93
4.3.2	Time-dependence of friction force	95
4.3.3	Load-vs.-friction	95
4.3.4	Constitutive system parameters	98
4.3.5	SPM-visualization of lubricant-lubricant interface	98
4.3.6	Derjaguin-offset versus lubricant order	104
	Conclusion	111
	Appendix	113
	A LAMMPS Script	113
	B Potential Parameters	119

C Best-Fit Parameters	123
List of Figures	129
List of Tables	131
Bibliography	133
List of Publications	145
Curriculum Vitae	149

Introduction

Tribology is the science of bodies in relative motion and deals mainly with friction, lubrication, and wear [1]. However simple the concept of friction (and the phenomenological laws describing it) may seem, its atomistic origins are still disputed. Understanding any tribological system will usually require a sound appreciation of a variety of phenomena covering a large spectrum of length and time scales [2]. It is this inherently multiscale nature of tribology that has led to considerable effort in recent years to bridge the gaps between the involved theories and methods.

In this context, atomistic modeling and simulation play an important role as tools for discovery [3]. The method of molecular dynamics (MD) simulations was first applied in the 1950s [4], but its introduction to the field of tribology did not come until the late 1980s [5, 6]. It allows the modeling of the behavior of solids and lubricants in systems where the surfaces come in such proximity that the resulting lubrication gap is of the order of a nanometer. In this case, the molecular/atomistic nature of matter can no longer be ignored, and continuum mechanics fails to correctly reproduce how the systems behave. Nowadays, MD is a well-established tool for studying friction at nanoscale, and several book chapters have been written on how to properly set up and carry out the required simulations [2, 7, 8, 9]. With powerful and flexible MD-codes abounding and often freely available over the internet [10, 11, 12, 13], this basic numerical machinery can thus be used by anyone with access to sufficient computing capacity. However, the art of scientific computing often starts when all the simulations have finished and the data have to be analyzed and interpreted.

My initial efforts in computational tribology were atomistic sliding simulations with unpolar lubricants similar to Refs. [14, 15, 16] aiming at the calculation of a nanoscopic coefficient of friction from the contact forces [17]. However, many tribological systems also involve surfactant-type molecules, which instead of layering laterally in the lubrication gap tend to adsorb to the slider surface and stand more or less upright, forming quasi-crystalline monolayers [18, 19, 20]. Furthermore, the behavior of these systems changes considerably with the nano-roughness of the sliders [21, 22] and the lubricant coverage, i.e., the packing density of the molecular chains on the surface [23, 24]. I therefore studied the relationship between the applied load and the resulting friction force in systems with varying slider roughness, lubricated with monolayers of fatty acids at diverse lubricant coverages [25, 26, 27]. Some of these systems obeyed the Amontons-Coulomb friction law [28, 29], but many, while being linear in their load-vs.-friction behavior, exhibited

a non-vanishing friction force at zero load, an offset first introduced by Derjaguin [30]. In this case, the nanoscopic coefficient of friction must be calculated as the slope of the load-vs.-friction relation for the respective system.

Things are further complicated when the asperities, i.e., the roughness features on the substrate, become as tall as the lubricant film is thick, so that they engage in contact if the lubricant fails to separate the solid surfaces. In a fashion conceptually similar to some work by Gao and co-workers [31], who analyzed the effect of an infinite, barrier-type roughness on a nano-junction lubricated with *n*-hexadecane, I simulated systems lubricated with fatty acids and studied their frictional response to the collisions of large asperities [32, 33, 34]. This leads to non-linearities and discontinuities in the load-vs.-friction relation where asperity contact plays a crucial role. A first approach to quantify the amount of asperity contact using the discrete MD representation of the system yielded a contact atom counting procedure, which proved to be quite simple but almost impossible to automatize and therefore neither reliable nor practical. This difficulty led to the idea of using the asperity contact area as a measure for the amount of asperity contact and calculating it with continuum mechanics.

Therefore, this work initially deals with the question of how MD data can be visualized continuously and how this representation may be used to better analyze simulation results. This constitutes an important step in the direction of multiscale tribology, as concepts for connecting the discrete world of atomistic simulations with continuum mechanics are being developed [35]. I will present a self-developed computational scheme which maps MD data to continuum based on the smooth particle method (SPM) [36]. This approach is then applied to straightforwardly calculate the contact area between two asperities as they touch during the breakdown of the lubricant film.

In a further step, I investigated if the knowledge of the asperity contact area can be incorporated into a nanoscopic kinetic friction law that can correctly reproduce the frictional response of lubricated atomistic tribosystems, i.e., the friction force as a function of the normal load, even if direct contact between the solid sliders occurs. The friction laws commonly in use only apply to systems under very specific conditions. A slightly extended friction law, which under certain circumstances automatically simplifies to well-known and trusted friction laws, could be applied much more generally to all kinds of nanotribological systems. By extending Derjaguin's modified Amontons-Coulomb friction law [30] with the Bowden-Tabor term [37], which includes the asperity contact area, I obtained a new three-term kinetic friction law which can reproduce the distinct non-linearities occurring in the load-vs.-friction behavior of many nanoscopic tribosystems [38, 39]. To my best knowledge, the simultaneous occurrence of the Derjaguin-offset and the Bowden-Tabor term in one friction law is extremely rare in literature. The parameters describing a system's frictional response are obtained from a fitting procedure and turn out to be load-independent system parameters. Several large-scale case studies to test the validity of the SPM-approach demonstrate that the proposed friction law is very well suited not only for characterizing steady-state sliding, but also nanoscopic run-in procedures [40].

A third aspect of this work is the speculation on the origin of the Derjaguin-offset in the proposed three-term kinetic friction law, which occurs predominantly, but not exclusively, in nanoscopic systems and is linked to adhesion in the presence of a thin layer of lubricant. In particular, there seems to be a connection between this offset and the degree of disorder in the lubricant [41], which may be quantified as its configurational entropy [40]. In real nanoscopic systems, e.g., nano-electromechanical systems (NEMS), the friction force is usually dominated by the adhesion-controlled contribution [42]. I will show that the load-independent friction force offset due to lubricant adhesion is reflected in the configurational entropy of the lubricant when disorder is induced by low lubricant coverage.

In chapter 1, I will lay out the theoretical framework to the extent required for understanding the MD simulations in this work. Chapter 2 deals with the components and the employed setup procedures of the simulated nanosystems. The methods for post-processing data analysis will be described in chapter 3. Finally, in chapter 4 I will present several large-scale case studies of MD shear simulations, validating the proposed methods, and discuss the theoretical findings.

Chapter 1

Classical Molecular Dynamics (MD)

In classical molecular dynamics (MD) simulations, atoms are treated as discrete particles characterized by properties such as their position, velocity, mass or charge. By integrating Newton's equations of motion for a set of these particles, the time development of the system can be followed. The forces acting on the particles are calculated as the negative gradient of their total energy, which is determined by the potentials governing the particle interactions.

Although the mathematical background for performing MD simulations has been known for a long time, for its actual application fast computers were necessary to carry out the numerical calculations and handle the large amounts of resulting data. In one of the pioneering works, Alder and Wainwright simulated the phase transition from liquid to solid for a hard sphere system in 1957 [4]. Gibson, Goland, Milgram, and Vineyard were probably the first to use a continuous potential in an MD calculation simulating the defects induced by radiation in 1960 [43]. In 1964, Rahman investigated numerous properties of liquid argon using a Lennard-Jones-type potential (discussed in section 1.2.1), obtaining surprisingly good results with respect to experimental data due to the inertness of the noble gas [44]. In another paper about the properties of argon in 1967, Verlet introduced his time integration algorithm (see section 1.3.1) which is still one of the most-used in MD simulations today [45]. Among the areas of interest to MD nowadays are liquids, fracture mechanics, cluster properties, biomolecules and drug design, and the subject of this work: friction at the nanoscale.

In this chapter I will briefly introduce some basic concepts required for understanding MD simulations. In general, only those aspects of MD which are important for this work will be discussed, for further information the reader is referred to textbooks which address the subject matter in a more comprehensive manner [46, 47, 48, 49, 50].

1.1 Newtonian Dynamics of Atoms

In classical MD, it is important to know why one may apply Newtonian dynamics to systems small enough that one would consider a quantum mechanical approach more

appropriate. In the widest possible sense, any system of particles obeys the rules of relativistic quantum mechanics. The problem is that the associated time-dependent Dirac equations describing the system's behavior are either impossible or extremely time consuming to solve for most systems. Therefore, depending on which sort of questions one wants to answer, certain approximations can be made which allow one to either simulate bigger systems and/or follow them for longer time spans, giving insights into the phenomena of interest. An overview of the hierarchy of approximations which can be made is given in Ref. [35], and a full account of how to derive classical molecular dynamics from quantum mechanics can be found in Ref. [50], but a short summary will be given here.

One can start by neglecting relativistic effects and try to solve the time-dependent Schrödinger equation. A first approximation is to separate the motion of the nuclei from that of the electrons, since the masses of protons and neutrons are almost 2000 times greater than those of electrons. Now it is reasonable to look at the electrons as moving in an effective force field generated by the nuclei, which leads to a system of two coupled equations which constitute the basis of the so-called time-dependent self-consistent field (TDSCF) approach. Taking the classical limit $\hbar \rightarrow 0$ of the time-dependent Schrödinger equation governing the motion of the nuclei, one obtains a set of equations which are isomorphic to the Hamilton-Jacobi formulation of the classical equations of motion. The nuclei now move according to Newton's equations in an effective so-called Ehrenfest potential which results from weighted-averaging the electrons' degrees of freedom with the nuclei held fixed.

In a next step, the calculation of the nuclear positions can be separated from the calculation of the potential energy hypersurface by solving the stationary electronic Schrödinger equation for numerous nuclear configurations. Thus it is possible to sample the Ehrenfest potential, allowing the introduction of an approximative reconstruction of the global energy hypersurface using analytical many-body potentials. Accordingly, Newton's equations of motion for classical MD simulations are written as

$$M_i \ddot{\mathbf{R}}_i(t) = -\nabla_{\mathbf{R}_i} V(\mathbf{R}(t)) , \quad (1.1)$$

where M_i is the mass and $\ddot{\mathbf{R}}_i(t)$ the acceleration of nucleus i , $\nabla_{\mathbf{R}_i}$ is the gradient evaluated at the position of nucleus i , and

$$V(\mathbf{R}(t)) = \sum_{i=1}^N V_I(\mathbf{R}_i(t)) + \sum_{i<j}^N V_{II}(\mathbf{R}_i(t), \mathbf{R}_j(t)) + \sum_{i<j<k}^N V_{III}(\mathbf{R}_i(t), \mathbf{R}_j(t), \mathbf{R}_k(t)) + \dots . \quad (1.2)$$

Here, $\mathbf{R}(t)$ is shorthand for $\mathbf{R}_1(t), \mathbf{R}_2(t), \dots, \mathbf{R}_N(t)$, where N is the total number of nuclei. The expansion in Eq. (1.2) can be further simplified to a two-body (pairwise) potential function V depending only on the distance between nuclei i and j , $|\mathbf{R}_j(t) - \mathbf{R}_i(t)|$. From here on, the explicit time-dependence of $\mathbf{R}(t)$ will be omitted for clarity if not necessary.

1.2 Interaction Potentials

The physics of an MD simulation is described by the potentials which model how the particles interact. The right choice of potentials used for a particular MD simulation is therefore of crucial importance. Potentials come in many classes, each one specialized in its own field of applications. Metals, for example, need to be treated quite differently than organic molecules or noble gases. Due to its simplicity and historical importance, I will first discuss the Lennard-Jones potential. I will then briefly introduce more specialized potentials used for modeling metal substrates in section 1.2.2 as well as for describing organic lubricants in section 1.2.3.

1.2.1 Lennard-Jones potential

The Lennard-Jones (LJ) potential as a simple but very useful two-body (pairwise) potential was introduced in the early 1930s [51],

$$V^{(\text{LJ})}(r_{ij}) = \alpha\varepsilon \left[\left(\frac{\sigma}{r_{ij}} \right)^n - \left(\frac{\sigma}{r_{ij}} \right)^m \right], \quad m < n, \quad m, n \in \mathbb{N}, \quad (1.3)$$

where

$$r_{ij} := |\mathbf{R}_j - \mathbf{R}_i|, \quad (1.4)$$

and

$$\alpha = \frac{1}{n - m} \left(\frac{n^n}{m^m} \right)^{\frac{1}{n-m}} \quad (1.5)$$

is a scaling factor ensuring that the minimum value of the function is $-\varepsilon$, such that the potential energy of a system of N particles is given by

$$V^{(\text{LJ})}(\mathbf{R}) = \sum_{i=1}^N \sum_{j>i}^N V^{(\text{LJ})}(r_{ij}). \quad (1.6)$$

In this work, the LJ potential is used in its most common form, namely with $n = 12$ and $m = 6$, i.e.,

$$V^{(\text{LJ})}(r_{ij}) = 4\varepsilon \left[\left(\frac{\sigma}{r_{ij}} \right)^{12} - \left(\frac{\sigma}{r_{ij}} \right)^6 \right]. \quad (1.7)$$

The term with the exponent 6 represents the van der Waals potential and models the dispersive dipole-dipole interactions between the particles. The other term may be interpreted as one which mimics the Pauli-repulsion of electrons, although the choice of the exponent 12 is not based on any physical law but mainly on numerical simplicity, since the term can then be easily calculated as the negative square of the van der Waals contribution. The energy parameter ε stands for the depth of the potential well, so higher values cause tighter binding and harder materials. The other parameter σ denotes the

zero-crossing of the LJ potential function and is proportional to the equilibrium distance $2^{1/6}\sigma = 1.12\sigma$ between the two particles. In Fig. 1.1 it can be seen that the potential decreases towards zero quite rapidly, so in order to save a considerable amount of computation time it makes sense to introduce a cut-off radius r_c , which is usually of the order of 3σ , beyond which all interactions are neglected. The small jump in the resulting potential, which causes a spike in the potential's gradient and therefore in the inter-particle force, can be remedied by shifting the entire function by $-V^{(\text{LJ})}(r_c)$.

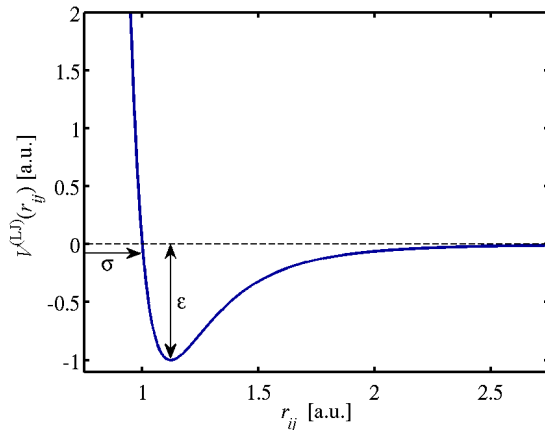


Figure 1.1: The Lennard-Jones potential as given in Eq. (1.7) for $\epsilon = 1$ and $\sigma = 1$.

1.2.2 Interaction potentials for metals

The Lennard-Jones potential cannot adequately reproduce the behavior of metals since it does not use information about the electronic structure. However, explicitly considering electrons would require a quantum mechanical treatment of the system, which is much more complex and would reduce the maximum number of atoms to ~ 1000 . To overcome this difficulty, in the mid-1980s several groups, most notably Daw and Baskes [52], Finnis and Sinclair [53], and Ercolessi, Parrinello, and Tosatti [54], developed potentials based on the general concept of density. As the local surrounding of an atom becomes denser, bonds become weaker, therefore the relationship between cohesive energy and coordination should not be linear anymore, as is the case with pairwise potentials [55]. This changes the form of the attractive part of the potential, while the part modeling the repulsion between atomic cores may remain pairwise.

In the approach by Daw and Baskes, the embedded atom method (EAM), an atom is viewed as an impurity embedded in a host of other atoms [52], and the total potential energy reads

$$V^{(\text{EAM})}(\mathbf{R}) = \sum_i F_i \left(\sum_{j \neq i} \rho_j(r_{ij}) \right) + \frac{1}{2} \sum_i \sum_{j \neq i} \phi(r_{ij}), \quad (1.8)$$

where F_i is the embedding energy as a function of the sum over the electronic densities ρ_j (at the position of, but excluding the contribution of atom i), and ϕ is the repulsive pairwise potential. Although F_i is a multi-body contribution since it depends on all atoms within atom i 's vicinity, the total energy is still a simple function of the positions of the atoms and therefore relatively straightforward to calculate.

The general functional form in Eq. (1.8) also applies to the Finnis-Sinclair potential and the glue model by the other groups mentioned above. However, the method leading to the functions F_i , ρ_j , and ϕ varies greatly between the three approaches.

1.2.3 Interaction potentials for molecules

System components that are truly molecular, i.e., including covalent bonds, feature internal degrees of freedom which are described with a different class of potential. There exist several potentials with associated sets of parameters intended for the description of molecular systems. Some of these are non-reactive, e.g., AMBER [56], CHARMM [57], or OPLS [58], while others such as REBO [59], AIREBO [60], and REAX-FF [61] allow the breaking and forming of bonds, thus being able to describe certain chemical reactions explicitly.

The original Optimized Potential for Liquid Simulations (OPLS) employs a partially united-atom (UA) model [62], where several atoms are grouped together and treated as a single superatom. Although this is computationally attractive since it greatly reduces the number of considered atoms and thus the computation time, the all-atom (AA) version of OPLS [63], which is used throughout this work, adds a considerable degree of exactness with respect to molecular torsions and partial charge distributions. The parameters for the non-bonded and the torsional potential terms, which will be discussed in the following, are either fitted to *ab initio* relativistic Hartree-Fock results or obtained from Monte Carlo simulations [58].

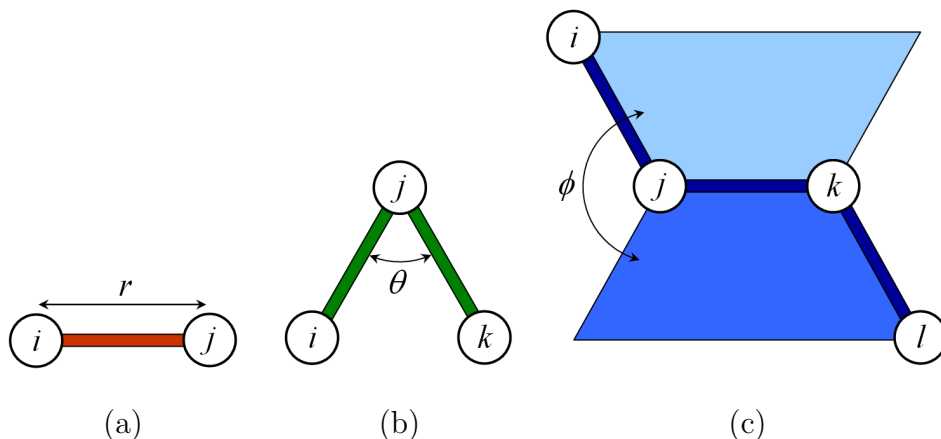


Figure 1.2: Representation of bond stretching (a), angle bending (b), and bond torsion parameters (c).

Intermolecular force field The OPLS-AA force field uses an LJ and a Coulombic potential to describe intermolecular interactions as well as the non-bonded intramolecular ones with more than two bonds between them,

$$\begin{aligned} V^{(\text{inter})}(r_{ij}) &= V^{(\text{LJ})}(r_{ij}) + V^{(\text{Coul})}(r_{ij}) = \\ &= \left\{ 4\varepsilon_{ij} \left[\left(\frac{\sigma_{ij}}{r_{ij}} \right)^{12} - \left(\frac{\sigma_{ij}}{r_{ij}} \right)^6 \right] + \frac{C}{\epsilon} \frac{q_i q_j}{r_{ij}} \right\} f_{ij}, \quad r_{ij} < r_c. \end{aligned} \quad (1.9)$$

Here, ε_{ij} and σ_{ij} are the LJ-parameters and r_{ij} is the distance between atoms i and j , which do not necessarily have to be of the same kind. The parameter q_i denotes the charge of atom i , C is an energy conversion factor depending on the used units, and ϵ is the relative dielectric constant. The scaling factor f_{ij} is zero if atoms i and j are separated by one or two bonds, 0.5 if separated by exactly three bonds, and 1 otherwise. The cut-off radius r_c may be different for the two parts of the potential since the Coulombic term is more long-ranged than the LJ term. LJ parameters for pairs of non-identical atoms ($i \neq j$) are obtained by applying the mixing rules

$$\sigma_{ij} = \sqrt{\sigma_i \sigma_j} \quad \text{and} \quad \varepsilon_{ij} = \sqrt{\varepsilon_i \varepsilon_j} \quad (1.10)$$

to the parameters for pairs of identical atoms.

Bond stretching The simplest internal degree of freedom in molecules is vibrational. This can be described, using Hooke's law, as a harmonic one with the two bonded particles' distance r_{ij} and the average bond length r_0 ,

$$V^{(\text{bond})}(r_{ij}) = K_r (r_{ij} - r_0)^2, \quad (1.11)$$

where K_r is the bond stiffness. Most of the bond stretching parameters tabulated for numerous atomic pairings in OPLS-AA were taken from the AMBER force field [56].

Angle bending Fig. 1.2 (b) shows how the bond angle θ between three neighboring bonded atoms i , j , and k is defined. The OPLS-AA force field includes harmonic oscillations of θ_{ijk} about its equilibrium value θ_0 ,

$$V^{(\text{angle})}(\theta_{ijk}) = K_\theta (\theta_{ijk} - \theta_0)^2, \quad (1.12)$$

with K_θ being the corresponding angle stiffness. As with the bond oscillations, most of the used values originate from the AMBER force field [56].

Bond torsions Perhaps the most important internal degree of freedom in molecules with more than three atoms is the bond torsion, which can be explained by inspecting Fig. 1.2 (c). Groups of three neighboring atoms, (i, j, k) and (j, k, l) , connected by successive bonds (shown in dark blue), define two planes (in lighter shades of blue). The

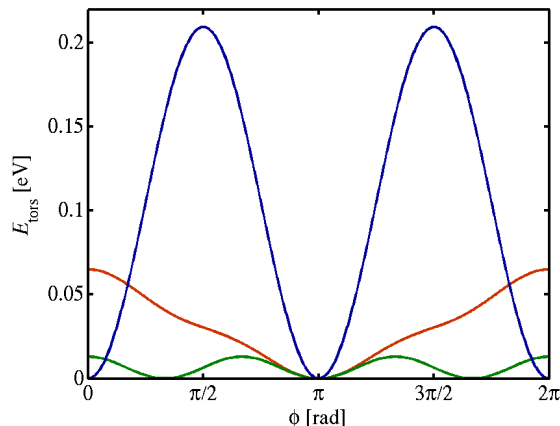


Figure 1.3: Shapes of the OPLS-AA torsional potential functions for the dihedral types C–C–C–C (red), H–C–C–H (green), and O=C–O–H (blue) in fatty acids.

angle between these two planes is the torsion or dihedral angle ϕ_{ijkl} . The group of the four atoms (i, j, k, l) defining ϕ_{ijkl} is called a dihedral.

The potential governing which values ϕ_{ijkl} are energetically favorable is of the general form

$$V^{(\text{tors})}(\phi_{ijkl}) = \frac{1}{2}V_1[1 + \cos(\phi_{ijkl})] + \frac{1}{2}V_2[1 - \cos(2\phi_{ijkl})] + \frac{1}{2}V_3[1 + \cos(3\phi_{ijkl})], \quad (1.13)$$

where the combination of the coefficients V_1 , V_2 , and V_3 determines the symmetry and multiplicity of the respective dihedral. The interplay between all dihedrals within a molecule influences the possible shapes of that molecule at a given temperature, and therefore its physico-chemical properties. Looking at Fig. 1.3, it is clear that the three exemplarily chosen dihedral types occurring in fatty acids favor the *trans*-configuration ($\phi_{ijkl} = \pi = 180^\circ$). The H–C–C–H dihedral has two additional minima allowing *gauche*-conformations ($\phi_{ijkl} = \pm\pi/3 = \pm 60^\circ$), while the O=C–O–H dihedral allows switching between the *trans*- and the *cis*-configuration ($\phi_{ijkl} = 0$), although only at high energetic cost. Note that this definition of ϕ_{ijkl} is conform to the IUPAC-convention, which differs from the so-called polymer-convention by a phase angle of $\pi = 180^\circ$ [50].

1.3 Integrators

In order to calculate the trajectories of the interacting particles in an MD simulation, their equations of motion, Eq. (1.1), must be integrated using a time integration algorithm. Time is discretized into finite time steps Δt , and knowing the configuration space of the system at a given time t , the algorithm calculates the configuration space at a time $t + \Delta t$. The iteration of this scheme then yields the system’s time development. There

exists an abundance of time integration algorithms, an overview of which can be found in Refs. [46, 50], but I will briefly discuss the ones used in this work in the following.

1.3.1 Basic and velocity Verlet algorithm

The Verlet algorithm has come to be one of the most widely used time integrators in MD. Although it was first applied on a computer to calculate the phase diagram of argon in 1967 by Verlet [45], the algorithm itself dates back to Størmer (1921) [64] and even Delambre (1790) [65].

We start out from two Taylor expansions of particle i 's positions $\mathbf{R}_i(t)$ at the times $t + \Delta t$ and $t - \Delta t$,

$$\begin{aligned} \mathbf{R}_i(t + \Delta t) &= \mathbf{R}_i(t) + \dot{\mathbf{R}}_i(t)\Delta t + \frac{1}{2}\ddot{\mathbf{R}}_i(t)\Delta t^2 + \frac{1}{6}\dddot{\mathbf{R}}_i(t)\Delta t^3 + \mathcal{O}(\Delta t^4) \\ \mathbf{R}_i(t - \Delta t) &= \mathbf{R}_i(t) - \dot{\mathbf{R}}_i(t)\Delta t + \frac{1}{2}\ddot{\mathbf{R}}_i(t)\Delta t^2 - \frac{1}{6}\dddot{\mathbf{R}}_i(t)\Delta t^3 + \mathcal{O}(\Delta t^4) \end{aligned} \quad (1.14)$$

Adding these two expressions and rearranging the terms yields

$$\mathbf{R}_i(t + \Delta t) = 2\mathbf{R}_i(t) - \mathbf{R}_i(t - \Delta t) + \ddot{\mathbf{R}}_i(t)\Delta t^2 + \mathcal{O}(\Delta t^4), \quad (1.15)$$

which constitutes the basic form of the fourth-order accurate Verlet algorithm. Here, the acceleration $\ddot{\mathbf{R}}_i(t)$ of the particle is computed using Newton's second law by dividing the negative gradient of the interaction potential $V(\mathbf{R}(t))$ by the particle's mass M_i ,

$$\ddot{\mathbf{R}}_i(t) = -\frac{1}{M_i}\nabla_{\mathbf{R}_i}V(\mathbf{R}(t)), \quad (1.16)$$

which is equivalent to Eq. (1.1). The first and third time derivatives of $\mathbf{R}_i(t)$ in Eq.(1.15) have canceled each other out, which means that the particle velocity $\dot{\mathbf{R}}_i(t)$ is not explicitly calculated in this formulation. Since it is necessary to compute the system's kinetic energy, the velocity may be obtained using

$$\dot{\mathbf{R}}_i(t) = \frac{\mathbf{R}_i(t + \Delta t) - \mathbf{R}_i(t - \Delta t)}{2\Delta t}, \quad (1.17)$$

but this expression is only second-order accurate.

The situation can be resolved by reformulating the Verlet algorithm to its velocity formulation, which explicitly produces the position, the acceleration, and the velocity of a particle at the time $t + \Delta t$,

$$\begin{aligned} \mathbf{R}_i(t + \Delta t) &= \mathbf{R}_i(t) + \dot{\mathbf{R}}_i(t)\Delta t + \frac{1}{2}\ddot{\mathbf{R}}_i(t)\Delta t^2 \\ \ddot{\mathbf{R}}_i(t + \Delta t) &= -\frac{1}{M_i}\nabla_{\mathbf{R}_i}V(\mathbf{R}(t + \Delta t)), \\ \dot{\mathbf{R}}_i(t + \Delta t) &= \dot{\mathbf{R}}_i(t) + \frac{1}{2}\left[\ddot{\mathbf{R}}_i(t) + \ddot{\mathbf{R}}_i(t + \Delta t)\right]\Delta t \end{aligned} \quad (1.18)$$

while being numerically more stable than the basic formulation.

1.3.2 rRESPA multi-timescale scheme

A problem commonly encountered when dealing with truly molecular systems which explicitly feature hydrogen atoms is that due to these atoms' small masses, the respective bond oscillations are of high frequency. In order to sample these oscillations sufficiently for ensuring energy conservation, the time step of the simulation would need to be set to ~ 0.5 fs, slowing down the entire calculation by a factor of ~ 4 compared to, e.g., a purely metallic system. It is therefore desirable to implement a multi-timescale scheme which allows the treatment of the computationally cheap bond oscillations using a shorter time step than for the much more expensive non-bonded interactions (LJ, EAM/FS).

The reversible REference System Propagator Algorithms (rRESPA) [66], which is related to predictor-corrector integrators, constitutes such a scheme and permits either the separation of time scales or of forces into short and long range components. For disparate mass systems, the “fast” and “slow” degrees of freedom are labeled ξ and ζ , respectively. The Liouville operator can be decomposed as

$$iL = iL_\xi + iL_\zeta , \quad (1.19)$$

with

$$iL_\xi = \dot{\xi} \frac{\partial}{\partial \xi} + F_\xi(\xi, \zeta) \frac{\partial}{\partial p_\xi} \quad (1.20)$$

and

$$iL_\zeta = \dot{\zeta} \frac{\partial}{\partial \zeta} + F_\zeta(\xi, \zeta) \frac{\partial}{\partial p_\zeta} . \quad (1.21)$$

The discrete time propagator $G_{\xi\zeta}(\Delta t)$ is factorized (Trotter-factorization [67]) as

$$G_{\xi\zeta}(\Delta t) = \exp \left[iL_\xi \left(\frac{\Delta t}{2} \right) \right] \exp [iL_\zeta(\Delta t)] \exp \left[iL_\xi \left(\frac{\Delta t}{2} \right) \right] . \quad (1.22)$$

Here, the “fast” propagator is further factorized as

$$\exp \left[iL_\xi \left(\frac{\Delta t}{2} \right) \right] = \left[\exp \left(\frac{\Delta t}{2} F_\xi \frac{\partial}{\partial p_\xi} \right) \exp \left(\delta t \dot{\xi} \frac{\partial}{\partial \xi} \right) \exp \left(\frac{\Delta t}{2} F_\xi \frac{\partial}{\partial p_\xi} \right) \right]^{\frac{n}{2}} , \quad n \in \mathbb{N} , \quad (1.23)$$

where $\delta t = \Delta t/n$. The middle propagator can also be factorized as

$$\exp [iL_\zeta(\Delta t)] = \exp \left(\frac{\Delta t}{2} F_\zeta \frac{\partial}{\partial p_\zeta} \right) \exp \left(\Delta t \dot{\zeta} \frac{\partial}{\partial \zeta} \right) \exp \left(\frac{\Delta t}{2} F_\zeta \frac{\partial}{\partial p_\zeta} \right) . \quad (1.24)$$

The velocity Verlet integrator is then employed for n small steps δt for the fast degrees of freedom, and only for one large step Δt for the slow degrees of freedom.

In this work, rRESPA is used to differentiate between bond, angle/dihedral, and non-bonded interactions. Bonds are updated every 0.5 fs, which sufficiently samples the H-bond oscillations, angles and dihedrals are updated every 1.0 fs, and non-bonded interactions every 2.0 fs. This leads to a ~ 2.5 -fold speed-up compared to using a constant time step of 0.5 fs for all interactions.

1.4 Thermostats

If a thermally isolated system has a constant number of particles, constant volume, and constant internal energy, then the equations of motion in Eq. (1.18) yield an isokinetic simulation, known in statistical physics as microcanonical or NVE-ensemble. Such thermodynamical conditions are difficult to maintain in real-world experiments, where it is usually the temperature which can be controlled via a heat bath.

1.4.1 Temperature of MD systems

The equipartition theorem states that the mean translational kinetic energy of a system and its temperature are linked as follows

$$\langle E_{\text{kin}} \rangle = \frac{3N}{2} k_{\text{B}} T , \quad (1.25)$$

where N is the number of particles in the system ($3N$ is the total number of degrees of freedom), k_{B} is the Boltzmann constant, and T is the temperature. By rearranging Eq. (1.25), the temperature is obtained as

$$T = \frac{1}{3Nk_{\text{B}}} \left\langle \sum_{i=1}^N M_i \dot{\mathbf{R}}_i^2 \right\rangle . \quad (1.26)$$

However, this definition is only accurate if the mean velocity of all particles is zero. This does not hold true for most tribological simulations as, *per definitionem*, the bodies are in relative motion. For this case, Eq. (1.26) has to be adjusted according to the local rest frame [68],

$$T = \frac{1}{3Nk_{\text{B}}} \sum_{i=1}^N M_i \left[\dot{\mathbf{R}}_i - \langle \mathbf{v}_{\text{reg}}(\mathbf{R}_i) \rangle \right]^2 , \quad (1.27)$$

where $\langle \mathbf{v}_{\text{reg}}(\mathbf{R}_i) \rangle$ is the mean velocity in a region around \mathbf{R}_i (“advection velocity”) and well-defined as long as it changes sufficiently slowly. Problems arise in simulations when the difference in the mean velocity between adjacent molecules starts becoming comparable to thermal velocities, in which case the temperature is not well-defined anymore. Care must therefore be taken that advection (e.g., shear) velocities remain below 10% of the speed of sound in order to prevent artifacts in the structure of the molecular systems or the friction forces [7].

1.4.2 A simple thermostat

The easiest and fastest way to thermostat a molecular system is based on explicitly rescaling the velocities of the particles with a scaling factor [50]

$$\vartheta = \left[\frac{T^{(\text{target})}}{T^{(\text{current})}} \right]^{\frac{1}{2}} = \left[\frac{E_{\text{kin}}^{(\text{target})}}{E_{\text{kin}}^{(\text{current})}} \right]^{\frac{1}{2}} \quad (1.28)$$

every ~ 100 time steps. This is done to allow the system's evolution during this rescaling interval. A more gentle way to change the velocities using a damping term has been proposed by Berendsen [69]. However, one needs to be aware that none of these methods comply with any known thermodynamic ensemble, so it is not possible to extract meaningful thermodynamic data from MD simulations which have been treated in this fashion. Moreover, these methods cannot remove unwanted or local correlations in the movement of the particles. They still constitute a very useful approach to quickly equilibrate a given system to the desired temperature before switching to a more sophisticated thermostatting scheme.

1.4.3 Langevin thermostat

A way to control the temperature of a system according to a thermodynamic ensemble such as the canonical (or NVT) ensemble is by extending the Hamiltonian of the system with an additional degree of freedom representing a heat bath. Several methods have been published to achieve this, notably the one proposed by Nosé and extended by Hoover [70, 71].

A related thermostat used throughout this work is the Langevin thermostat as described in Ref. [72]. Mathematically, it models an interaction with a background implicit solvent and, coupled with a suitable time integration scheme, performs Brownian dynamics on a system. In this case, the force \mathbf{F}_i acting on each atom i consists of three contributions,

$$\mathbf{F}_i = \mathbf{F}_i^{(c)} + \mathbf{F}_i^{(f)} + \mathbf{F}_i^{(r)}, \quad (1.29)$$

where $\mathbf{F}_i^{(c)}$ is the conservative force calculated from the pairwise potentials,

$$\mathbf{F}_i^{(f)} = -\frac{M_i}{\lambda} \dot{\mathbf{R}}_i \quad (1.30)$$

is a viscous damping force, with M_i being the mass and $\dot{\mathbf{R}}_i$ the velocity of atom i , and λ is the damping time constant inversely proportional to the simulated heat conductivity. $\mathbf{F}_i^{(r)}$ is a uniform (non-Gaussian) random force [73], for which

$$|\mathbf{F}_i^{(r)}| \propto \sqrt{\frac{k_B T_{\text{bath}} M_i}{\Delta t \lambda}} \quad (1.31)$$

holds true. Here, k_B denotes Boltzmann’s constant, T_{bath} is the heat bath temperature and Δt is the time step. In order not to influence the motion of the atoms in the directions of shear or compression through the thermostat, one can choose to apply it only in the direction normal to these directions.

1.5 Boundary Conditions

The type of boundary conditions for the simulation box have to be specified for each Cartesian direction. With periodic boundary conditions, particles interact across the boundary, and they can exit the simulation box on one end and re-enter from the other end. These cyclic boundary conditions must be applied to both faces of a spatial dimension. The alternative to periodic boundary conditions is fixed ones. This means that the box is non-periodic, so that particles do not interact across the boundary and do not move from one side of the box to the other. The position of the simulation box face is fixed, so if an atom moves outside it is usually lost. This can be remedied by employing a variation of fixed boundary conditions, where the position of the face is set so as to encompass the atoms in that dimension (“shrink-wrapping”), no matter how far they move.

In the tribological simulations in this work, two surfaces are moved with respect to each other. The two directions which span these surfaces, x and y , require periodic boundary conditions in order to minimize boundary effects, while the third direction along which the normal force is applied, z , requires fixed or shrink-wrapped boundary conditions, where the latter represent the safer solution since atoms cannot be lost even during severe loading conditions.

1.6 LAMMPS

The code used to perform all simulations in this work is LAMMPS, the Large-scale Atomic/Molecular Massively Parallel Simulator developed at Sandia National Labs [10, 74]. It runs on a single processor or in parallel and supports distributed-memory message-passing parallelism (MPI) via spatial decomposition of the simulation domain. Written in C++, it is available under the GNU Public license and is relatively easy to extend with new features and functionality.

LAMMPS features numerous particle and model types and includes several force fields. It supports various thermodynamic ensembles, thermostats, boundary conditions, and integrators, and has highly customizable output options. LAMMPS usually runs from an input script and requires users to do most of their pre- and post-processing externally. It does not feature a built-in graphical user interface, but it can be linked with interactive MD (IMD) clients such as the VMD visualization program [75].

Finally, there is a large world-wide community of LAMMPS users who will help each other out, most notably the main developers who answer most of the questions themselves.

There are near-daily updates and bugfixes, and major revisions can be expected about every 6 months.

Some technical aspects of LAMMPS are covered in the discussion of a typical script file used for MD shear simulations which can be found in appendix A.

Chapter 2

MD-setup of Nanosystems

In this chapter, all of the nano-systems treated in this work will be described. They differ in overall size, the type and the amount of lubricant used, as well as the crystal structure, thickness and the roughness of the solid substrates. I will first introduce all system components including the constraints on the system necessary to ensure the desired sliding conditions, i.e. either constant or periodic friction force, and then go through all steps necessary for system assembly. The setups of the specific systems are explained in the respective sections of chapter 4.

2.1 System Components

2.1.1 Substrate

All tribological nanosystems in this work have solid sliders consisting of pure Fe as an approximation for a steel surface. Although a Fe oxide such as hematite (Fe_2O_3) may constitute an even better approximation, its dynamic modeling, particularly in the case of plastic deformation, is very difficult and affected by a high degree of uncertainty. The Fe-Fe interactions are governed by a Finnis-Sinclair potential (formally equivalent to the embedded atom method, EAM [52]) as introduced in section 1.2.2, with the parameters taken from Ref. [76], which will be referred to as the EAM-FS potential. The cutoff-radius intrinsic to this set of parameters is 0.53 nm. The used potential can describe the substrate and the asperities much more accurately than any type of pair potential [55]. This is important since the simulations in this work include solid-solid contact with plastic deformation and material transfer, which otherwise would not be handled correctly. Most considered substrates are amorphous in order to model tribologically pre-worn surfaces, but section 4.3 also features crystalline bcc Fe(100) surfaces which can be interpreted as a model of the α -ferrite phase of steel [77].

The large Fe substrates designed for studies focusing on asperity shape and contact area have lateral dimensions of 26×13 lattice constants. With the lattice constant of $a_{\text{Fe}} = 0.2855$ nm used in the EAM-FS potential, this is equivalent to an apparent contact

area of $7.42 \times 3.71 = 27.56 \text{ nm}^2$. The small substrates intended for studies of boundary lubricant performance and disorder have lateral dimensions of 13×13 lattice constants, leading to a nominal contact area of $3.71 \times 3.71 = 13.78 \text{ nm}^2$.

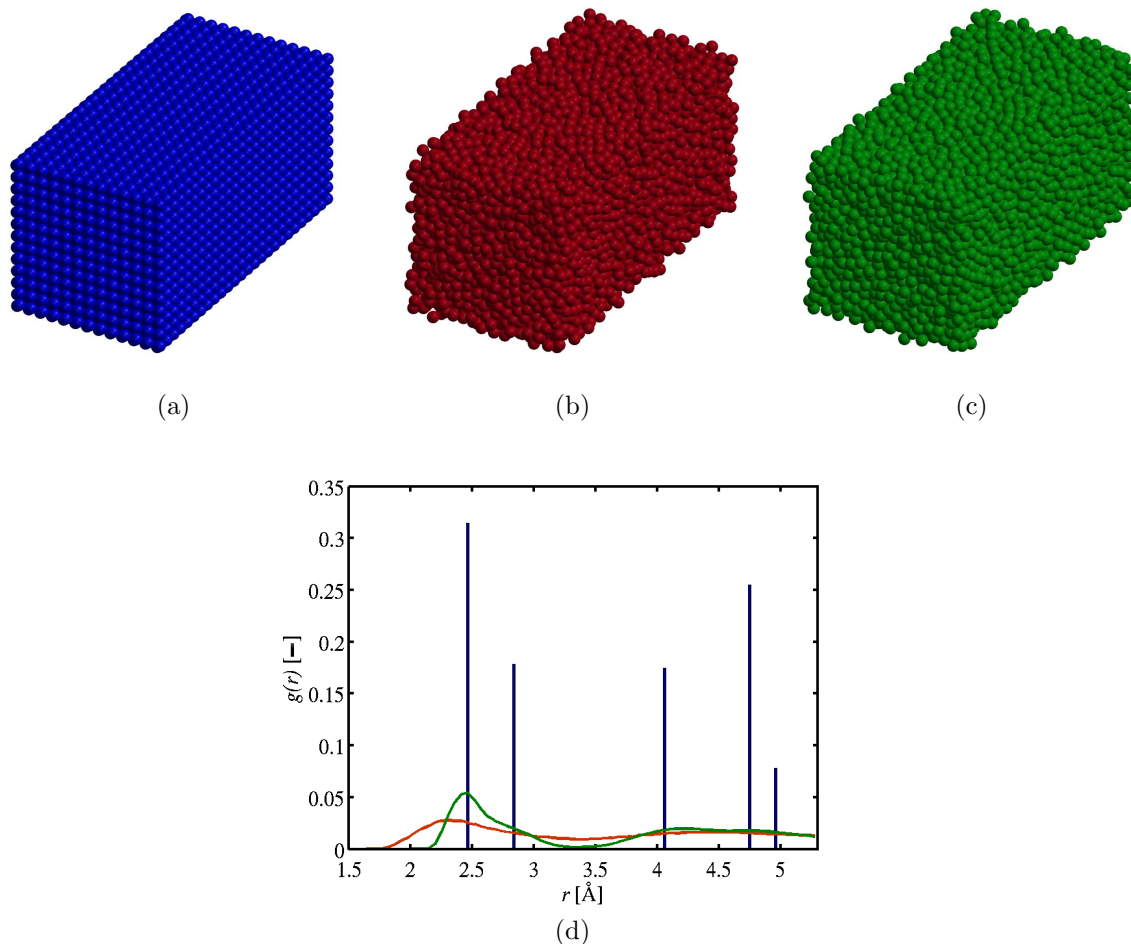


Figure 2.1: Amorphization of a bcc Fe crystal. (a) perfect crystal at 0 K, (b) fluid Fe at 5000 K, (c) amorphous solid Fe at 300 K, (d) normalized radial distribution function $g(r)$ of the system at 0 K (blue), 5000 K (red), and 300 K (green).

Amorphization procedure The iron is amorphized by setting up a bcc Fe crystal of $26 \times 13 \times 13$ lattice constants for the large systems, see Fig. 2.1 (a), and $13 \times 13 \times 6$ lattice constants for the small systems. Using periodic boundary conditions in all three spatial directions in order to simulate bulk behavior, this crystal is heated to 5000 K, well beyond the boiling point of Fe, see Fig. 2.1 (b). It is kept at this temperature for 5 ps using a crude velocity-rescaling scheme, cf. section 1.4. The Fe is then quenched by linearly reducing the temperature to 300 K within 0.25 ps. This results in the formation of an

amorphous solid, which is relaxed at 300 K for another 5 ps, see Fig. 2.1 (c). Fig. 2.1 (d) shows the normalized radial distribution function $g(r)$ [46] of the system at the three temperatures, which quite clearly confirms the expected order in all structures. From the shape of the green curve which denotes $g(r)$ at $T = 300$ K, it is obvious that the system has not recrystallized but remains in the amorphous state.

Large asperities The substrates with large asperities are generated by carving the desired geometry from the amorphous block of Fe. The three different asperity types treated in this work are characterized as follows:

- Semi-sphere, see Fig. 2.2 (a). Geometrical parameters: $x_C = 5.568$ nm, $y_C = 1.856$ nm, $r_{\text{asp}} = 1.5$ nm, see Fig. 2.2 (b), 606 atoms.
- Truncated cone, see Fig. 2.2 (c). Geometrical parameters: $x_C = 5.568$ nm, $y_C = 1.856$ nm, $r_{\text{base}} = 1.6$ nm, $h_{\text{asp}} = 1.8$ nm, $\omega = 65^\circ$, see Fig. 2.2 (d), 707 atoms.
- Slanted pyramid, see Fig. 2.2 (e). Geometrical parameters: $x_C = 5.568$ nm, $y_C = 1.856$ nm, $d_x = 3.0$ nm, $d_y = 2.0$ nm, $d_z = 1.8$ nm, $\alpha = 40^\circ$, $\beta = 70^\circ$, $\gamma = \delta = 75^\circ$, see Fig. 2.2 (f), 443 atoms.

The asperity base center coordinates x_C and y_C are chosen in such a way that if the upper slider is moved in positive x -direction at the constant shear velocity of 4.0 m/s = 4.0 nm/ns, while the bottom slider is held fixed in space, the two asperities may start touching after approximately 0.75-1.25 ns, depending on their geometry.

Multiple small asperities The small crystalline systems are given nanoscopic roughness by placing three nominally cylindrical islands on the exposed bcc (100) surface of each slider with radii of 3.5, 5.25, and 7 Å, and with center coordinates of (28.55, 11.42) Å, (7.57, 7.57) Å, and (17.13, 25.70) Å, respectively, see Fig. 2.3. The height is varied equally for all islands from 1–4 monolayers (ML) of bcc Fe, where 1 ML corresponds to a roughness of $R_a = 1.43$ Å. The higher cylindrical islands (3–4 ML) blunt to a more pimpled shape within several ps of surface relaxation at $T = 300$ K.

Constraints and thermostat In the large systems, the topmost 676 atoms of the top slider as well as the bottommost 676 atoms of the bottom slider, corresponding to 2 ML of bcc Fe(100), are kept rigid at all times in order to account for the underlying bulk solid and to facilitate the movement control of the respective counteracting bodies, see the light parts of the substrates in Fig. 2.2. For the smaller systems, the number of rigid atoms per slider is 507, corresponding to 3 ML of bcc Fe(100) in the crystalline substrates. The rigid part of the lower slider is held fixed in space, while the rigid part of the upper slider is not allowed to move perpendicular to the directions of load and shear, i.e., in y -direction.

A Langevin thermostat, discussed in section 1.4.3, with a damping time constant of $\lambda = 0.5$ ps keeps all non-rigid Fe atoms at 300 K, allowing the lubricant molecules to

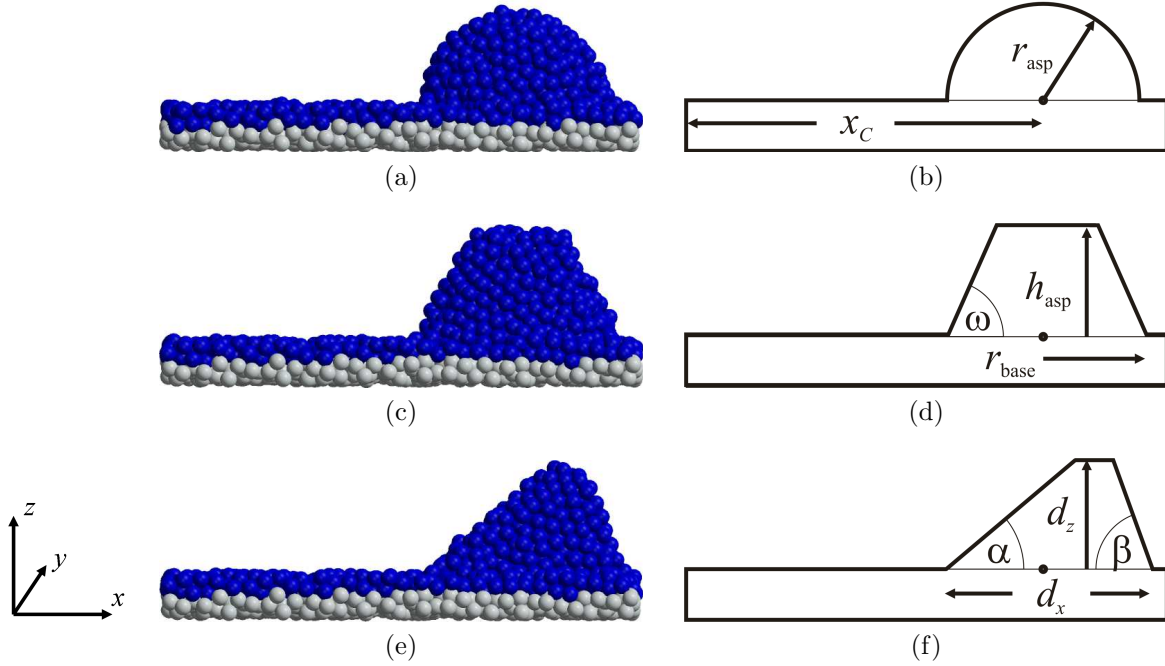


Figure 2.2: The three large asperity types used in this work: (a, b) semi-sphere, (c, d) truncated cone, (e, f) slanted pyramid. In the MD-snapshots in the left column, the blue parts of the substrate are treated dynamically, i.e. the atoms interact via the EAM-FS potential, and are thermostatted, while the gray parts are kept rigid throughout the simulations. The sketches in the right column are annotated to explain the meaning of the geometrical asperity parameters used in the text. The lengths y_C and d_y as well as the slanted pyramid aperture angles γ and δ lie perpendicular to the paper plane and should be interpreted accordingly.

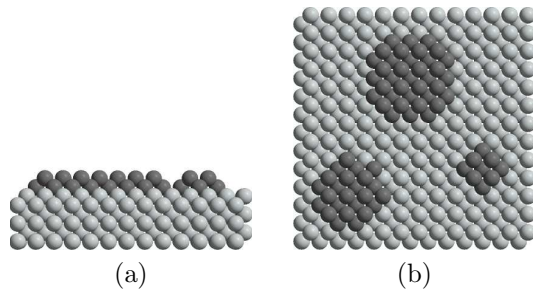


Figure 2.3: Side (a) and top view (b) of the small substrates with roughness corresponding to 2 ML of bcc Fe(100). The roughness islands are shown in dark gray.

remain unthermostatted. The frictional heat generated in the lubrication gap during sliding is therefore transported towards the substrate and hence to the heat bath via phononic heat transfer. In analogy to Refs. [78, 79, 80, 81], this thermostat is applied only in the y -direction to prevent any influence on shear (in x -direction) and compression (in $-z$ -direction). Although a more sophisticated thermostating procedure [82, 83] might lead to a more realistic temperature distribution within the nanotribological systems, the employed Langevin thermostating method remains sufficiently appropriate as long as the shear velocity does not exceed 10 m/s [84], which is not the case here as described in section 2.2.4.

2.1.2 Lubricants

All model lubricants simulated in this work interact via the Optimized Potential for Liquid Simulations – All Atom (OPLS-AA) introduced in section 1.2.3, which includes bond stretching, angle bending and dihedral (torsional) parameters for intramolecular interactions, as well as van der Waals and Coulombic terms. The OPLS-AA force field treats all atoms in the molecules explicitly, ensuring a very exact description of the lubricant, and is in widespread use for the analysis of the tribological properties of lubricants, e.g., Refs. [78, 79, 80, 81]. However, chemical reactions such as the breaking and forming of bonds are not described in this force field. The cutoff-radii for the LJ and Coulombic interactions are 1.0 and 1.8 nm, respectively. These values are a good compromise between accuracy and computational efficiency. All potential parameters used throughout this work can be found in appendix B.

It is not intended in this work to model any high-molar, industrially applied lubricants, but rather to simulate simple representants of several lubricant categories, namely unpolar hydrocarbons, fatty acids, and esters, shown in Figs. 2.4–2.7.

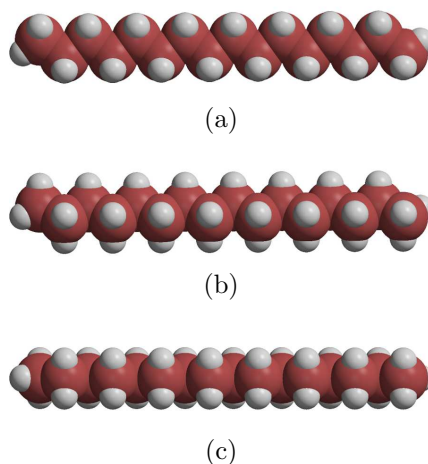


Figure 2.4: *n*-hexadecane (alkane): $\text{CH}_3(\text{CH}_2)_{14}\text{CH}_3$, (a) side view, (b) 45-degree view, (c) front view. Carbon atoms are shown in brick red, hydrogen atoms in white.

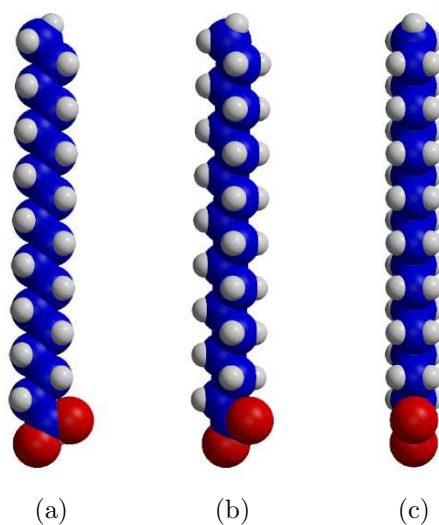


Figure 2.5: stearic acid (saturated fatty acid): $\text{CH}_3(\text{CH}_2)_{16}\text{COOH}$, (a) side view, (b) 45-degree view, (c) front view. Carbon atoms are shown in blue, hydrogen atoms in white, and oxygen atoms in red.

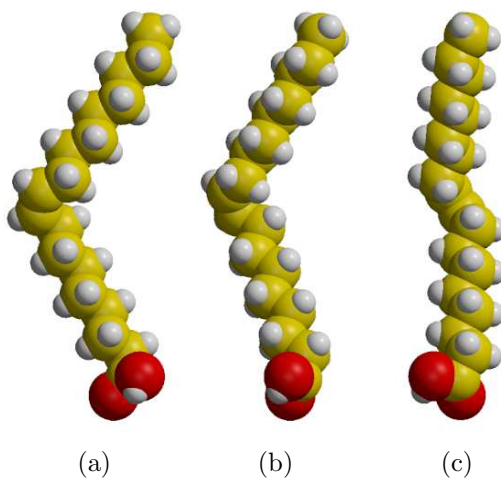


Figure 2.6: oleic acid (monounsaturated omega-9 fatty acid): $\text{CH}_3(\text{CH}_2)_7\text{CH}=\text{CH}(\text{CH}_2)_7\text{COOH}$, (a) side view, (b) 45-degree view, (c) front view. Carbon atoms are shown in yellow, hydrogen atoms in white, and oxygen atoms in red.

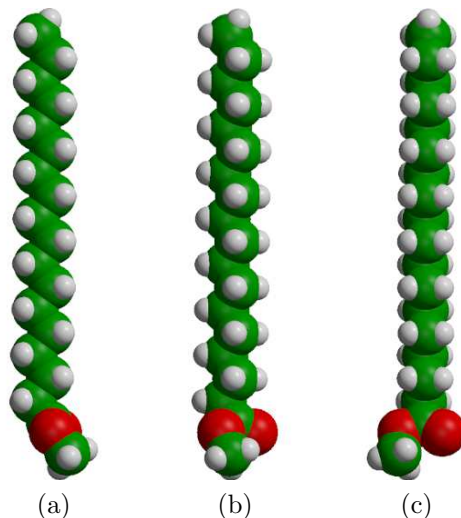


Figure 2.7: stearic acid methyl ester (methyl stearate): $\text{CH}_3(\text{CH}_2)_{16}\text{COO}-\text{CH}_3$, (a) side view, (b) 45-degree view, (c) front view. Carbon atoms are shown in green, hydrogen atoms in white, and oxygen atoms in red.

The molecule chosen to represent the first of these categories is *n*-hexadecane, or cetane, a linear alkane with the chemical formula $\text{CH}_3(\text{CH}_2)_{14}\text{CH}_3$, which can be seen in Fig. 2.4. It has been widely used in nanotribological MD-simulations, e.g., [15, 85, 86, 87], due to its relative simplicity as well as its well-defined and experimentally well-known properties. In this work, *n*-hexadecane was employed as a model lubricant in preliminary simulations [17] and as a base lubricant in section 4.3. The representatives of the second lubricant category, fatty acids, are stearic acid, $\text{CH}_3(\text{CH}_2)_{16}\text{COOH}$, cf. Fig. 2.5, and one of its mono-unsaturated versions, oleic acid, $\text{CH}_3(\text{CH}_2)_7\text{CH}=\text{CH}(\text{CH}_2)_7\text{COOH}$, cf. Fig. 2.6. Both are polar surfactant-type molecules which can adsorb to the sliders with their carboxylic (COOH) head groups and form well-ordered monolayers, thus protecting the surface against wear and/or modifying its frictional properties. The main difference between the two is the double C=C bond in the middle of oleic acid which introduces a layer of defects in its surface films. Finally, stearic acid methyl ester, or methyl stearate with the chemical formula $\text{CH}_3(\text{CH}_2)_{16}\text{COO}-\text{CH}_3$, cf. Fig. 2.7, represents the lubricant category of esters. It also forms monolayers on slider surfaces, which again have slightly different frictional properties, mainly due to its bulkier head group which has a methyl group attached. The color scheme in Figs. 2.4–2.7 uses different colors for the C-atoms in different types of lubricants, making their distinction in section 4.3 easier. In sections 4.1 and 4.2, where only stearic acid is used as a lubricant, a different color scheme was used for better contrast between the lubricant layers, see Fig. 2.12.

Solid-lubricant interaction The interaction between the lubricant and the solid is governed by an LJ potential, which is constructed by first assuming some “dummy” LJ

parameters for the substrate atoms (“dummy” because they are used only for constructing the lubricant-solid potential, not for the actual calculation of solid-solid interactions) and then applying the geometric mixing rules $\varepsilon_{ij} = \sqrt{\varepsilon_i \varepsilon_j}$ and $\sigma_{ij} = \sqrt{\sigma_i \sigma_j}$ from section 1.2.3 to these and the non-bonded OPLS-AA parameters of the lubricant. These “dummy” parameters were chosen in such a way that they yield values for the interaction between the substrate and the aliphatic tails of the lubricant comparable to those in Refs. [88, 89]. In a similar fashion to Ref. [19], the interaction potential for O and Fe was then modified so that it is roughly five times stronger than the C-Fe interaction, yielding $\varepsilon_{O-Fe} = 0.1$ eV and $\sigma_{O-Fe} = 0.29$ nm.

2.2 Assembly of a Tribosystem

In this section I will discuss which general steps are necessary to successfully assemble an MD-nanosystem from the components introduced above. The solid surfaces may be atomically flat or nanoscopically rough, in which case the lubricant molecules need to be rearranged to obtain a more or less uniform boundary layer with all lubricant molecules attached to the substrate. I will finally explain the equilibration, compression and shear procedures used throughout this work.

2.2.1 Lubricant coverage

Uniform lubricant film For many of the simulations in this work, a uniform cover of lubricant molecules adsorbed to the solid surface is desired. For flat and slightly rough substrates, this can be achieved by placing molecules on a regular two-dimensional mesh, with the functional groups pointing towards the substrate, see Fig. 2.8 (a). Note here that periodic boundary conditions in the lateral dimensions lead to seemingly disconnected molecules. This highly ordered film is then positioned so that it is initially at a distance of several Ångströms to the surface. Typical maximum achievable lubricant coverages η , i.e., the number of molecules per unit area, for the small sliders range from $\simeq 60$ to 80 molecules per slider, depending on lubricant type, which is equivalent to an available substrate area of $\simeq 17\text{--}23$ Å² per head group.

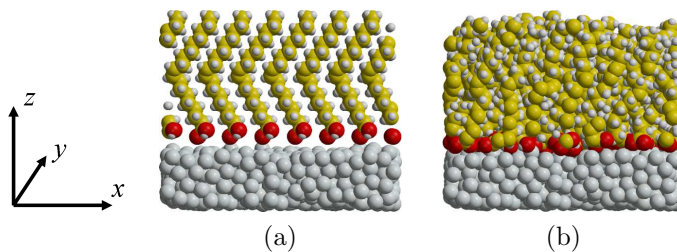


Figure 2.8: Equilibration of a boundary layer of 7×8 oleic acid molecules on a flat amorphous Fe surface. (a) initial configuration, (b) after 100 ps of equilibration.

Surface roughness adaptation With growing surface corrugation, especially for the case of a single large asperity, it becomes increasingly difficult to achieve uniform coverage in a reasonable amount of time ($\simeq 100$ ps) using the approach described above. This is due to the fact that the film would have to be initially placed far enough from the solid surface so as not to overlap with the highest asperity. The lubricant then tends to clot together and/or lose its orientation before it can form a film. This problem can be remedied by searching for the surface atom with the highest z -value in the area allocated to each lubricant molecule, thus coarsely meshing the surface. This representation of the substrate may then be used to place every individual lubricant molecule at the same z -distance to the surface, thus reproducing the surface topography with the lubricant film. This allows much faster film formation on substrates with roughness exceeding $\simeq 5$ Å.

2.2.2 Lubricant equilibration

With the solid and the lubricant assembled into one MD system as described above and as shown in Figs. 2.8 (a) and 2.10 (a), one may now simulate film formation on the substrate using the solid-lubricant interaction potential discussed in section 2.1.2. Film formation is usually straightforward for sufficiently flat substrates, but with growing surface roughness it may become necessary to add a moderate force to the lubricant molecules in $-z$ direction for the first ps to accelerate the process and ensure that all molecules adsorb to the surface. Depending on the lubricant type and the lubricant coverage η , the molecules assume a typical tilt angle with respect to the surface normal [23]. Fig. 2.9 shows how the tilt angle develops during film adsorption to a flat slider with high (a) and one with low η (b). Here, the tilt angle is defined as the angle of the vector between the two second-to-outermost C-atoms in every lubricant molecule with the z -axis. After approximately 100 ps, most films have adsorbed to the substrate as shown in Figs. 2.8 (b) and 2.10 (b), which may be verified by monitoring the energy contributions of the lubricant as well as the pressure and the volume of the system.

Pre-worn boundary lubricant For simulations of mixed lubrication, it can make sense to construct a lubricant layer so that it represents a pre-worn film of boundary lubricant which has already been subjected to tribological stress. In these cases, lubricant coverages lie well below the experimentally observed [90] or calculated [23] ones for perfectly ordered monolayers. Furthermore, in order to analyse systems where the boundary lubricant is at the verge of failing, as will be discussed in section 4.1, it is of interest to find the lubricant coverage for each system where the occurrence of direct asperity contact depends on the applied load. This coverage is a function of asperity size and shape, and must be found empirically. If set too high, direct asperity contact might never occur during shear. Likewise, if set too low, asperity contact might always occur, irrespective of load. To find a coverage in the narrow transition regime in between, configurations with a range of lubricant coverages are simulated at various loads. As an example, the first simulations may be carried out with 50, 60, 70 and 80 molecules per slider. If solid-solid

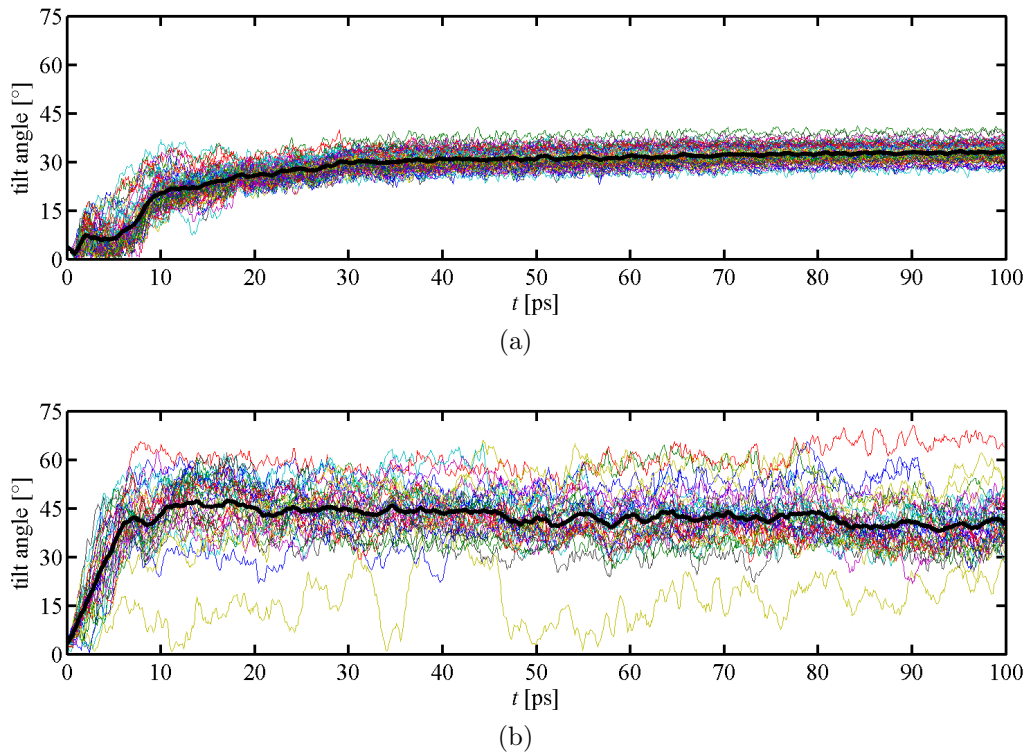


Figure 2.9: Equilibration development of the individual molecular tilt angle on a flat substrate with 7×9 (a), and one with 5×7 stearic acid molecules (b). The bold black curves are averages over all the molecules in the film.

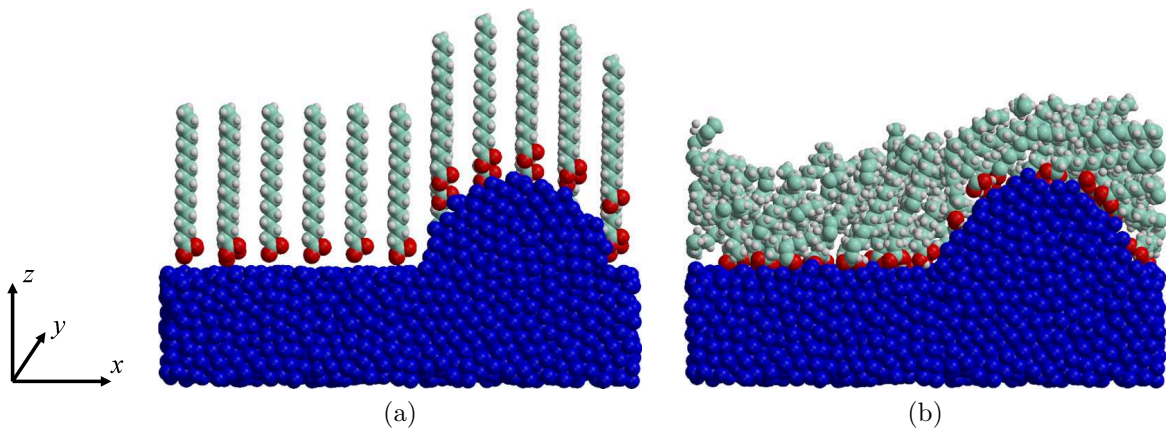


Figure 2.10: Equilibration of a boundary layer of 66 stearic acid molecules on an amorphous Fe-slider with semi-spherical asperity. (a) Initial configuration with the stearic acid molecules positioned using surface roughness adaptation. (b) After 100 ps of equilibration.

contact occurs at all loads for the system with 60 molecules, but no contact occurs at 70 molecules per slider, the systems with 62, 64, 66 and 68 molecules per slider are tested as well. If the system with 66 molecules exhibits solid-solid contact at high loads, but not at low loads, the coverage of interest has been found.

In order to obtain a pre-worn lubricant film, the number of molecules is controlled by first uniformly covering the surfaces with lubricant molecules using the method discussed above and then removing molecules one by one, starting from the top of the asperity moving downward. A reasonable choice for the reference atom is an O-atom in the functional group of the molecule, as it is very close to the substrate and least likely to be shifted by molecular tilting. So, to generate a configuration with 70 molecules per surface, one can start out with a uniform grid of 11×8 molecules and then remove the 18 topmost molecules from the asperity. This approach is motivated by previous simulations [32] which showed that the molecules on the tips of asperities are the first to be sheared off as a result of previous tribological loading. Fig. 2.11 illustrates that the desorbed molecules are among the ones originally located near the top of the asperities, in particular on the sides facing each other.

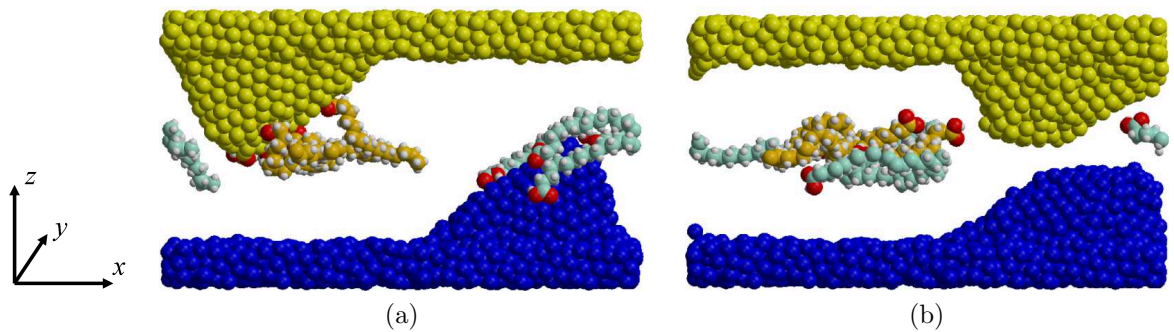


Figure 2.11: Lubricant molecules desorbed from the asperities due to shear: (a) initial configuration and (b) after asperity contact. For clarity, no molecules which remain adsorbed to the surface throughout the shear simulation are shown. Colors: Fe (top)—yellow, Fe (bottom)—blue, C (top)—orange, C (bottom)—light blue, H—white, O—red. Different colors for Fe and C in the top and bottom halves of the system only serve to better show the sliding interface as well as material transfer.

2.2.3 Compression

As soon as a film of lubricant has equilibrated on the lower substrate, this entire system is duplicated, with the upper slider flipped upside-down and placed above the lower one so the lubricant films face each other. The equations linking the atom positions of the upper slider $(x, y, z)_{\text{hi}}$ to the ones of the lower one $(x, y, z)_{\text{lo}}$ read

$$x_{\text{hi}} = 2x_{C,\text{box}} - x_{\text{lo}}, \quad y_{\text{hi}} = y_{\text{lo}}, \quad z_{\text{hi}} = 2z_{C,\text{box}} + D_z + \delta_{z,\text{offset}} - z_{\text{lo}}, \quad (2.1)$$

where $(x, y, z)_{C,\text{box}}$ is the position of the simulation box center and D_z is the z -dimension of the box. A distance $\delta_{z,\text{offset}}$ must be kept between the two halves of this new system so no molecules can overlap, which would lead to very high initial forces due to close proximity and subsequent disintegration of the system. A distance of $\delta_{z,\text{offset}} = 0.3$ nm is usually sufficient between the topmost lower lubricant and the bottommost upper lubricant atom centers. However, for highly corrugated surfaces, different values may apply depending on the respective configuration. The atom velocities of the entire system are usually re-assigned randomly according to the Maxwell-Boltzmann velocity distribution in order to decouple the thermodynamics of the two sliders. If this is not wanted, the momentary velocities of the lower-slider atoms must be transformed as well via the equations

$$v_{x,\text{hi}} = -v_{x,\text{lo}}, \quad v_{y,\text{hi}} = v_{y,\text{lo}}, \quad v_{z,\text{hi}} = -v_{z,\text{lo}}. \quad (2.2)$$

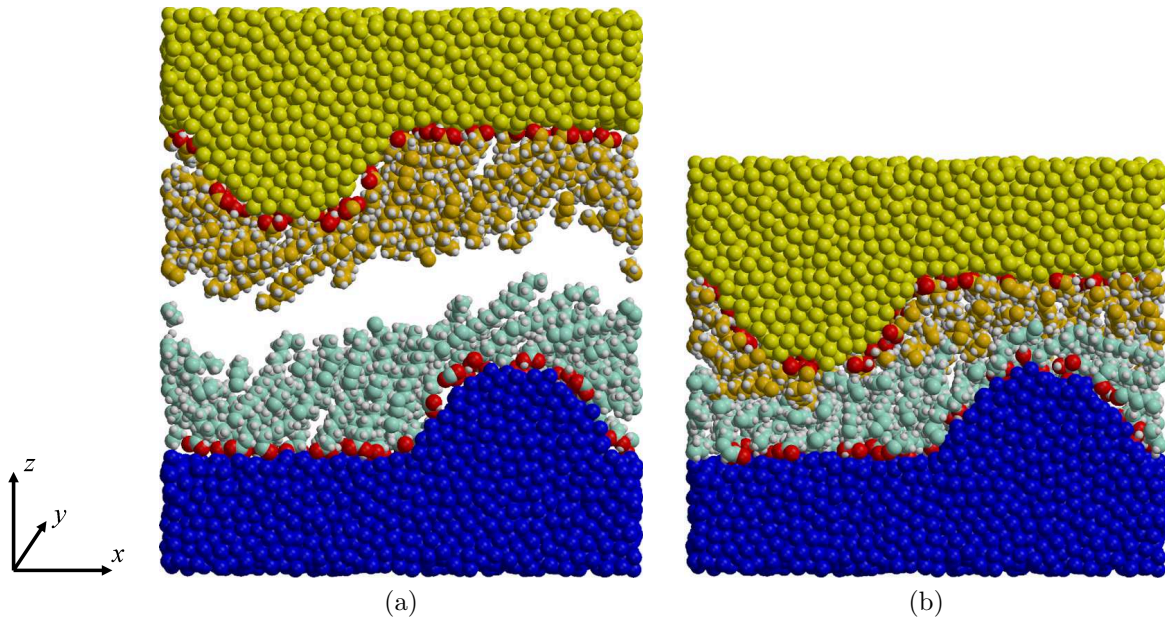


Figure 2.12: Compression of a semi-spherical asperity system. (a) Before compression. (b) Compressed to $L = 22.04$ nN (0.8 GPa). The color scheme is the same as in Fig. 2.11.

With the position of the lower slider of the system kept stationary, the compression velocity $-v_z$, applied to the rigid portion of the upper slider, is ramped from 0–35 m/s over a period of 22 ps and then kept at this maximum value for another 170 ps.

During the compression period, the relevant thermodynamic properties such as the energetic contributions, the system volume, temperature and pressure, as well as the reaction forces in the system are monitored (more information on calculating forces can be found in section 3.3). For systems with very small surface roughness and well-ordered boundary lubricant films, one can observe a period of adhesion between the lubricant layers before the proximity of the sliders leads to repulsion, see Fig. 2.13(b). The compression

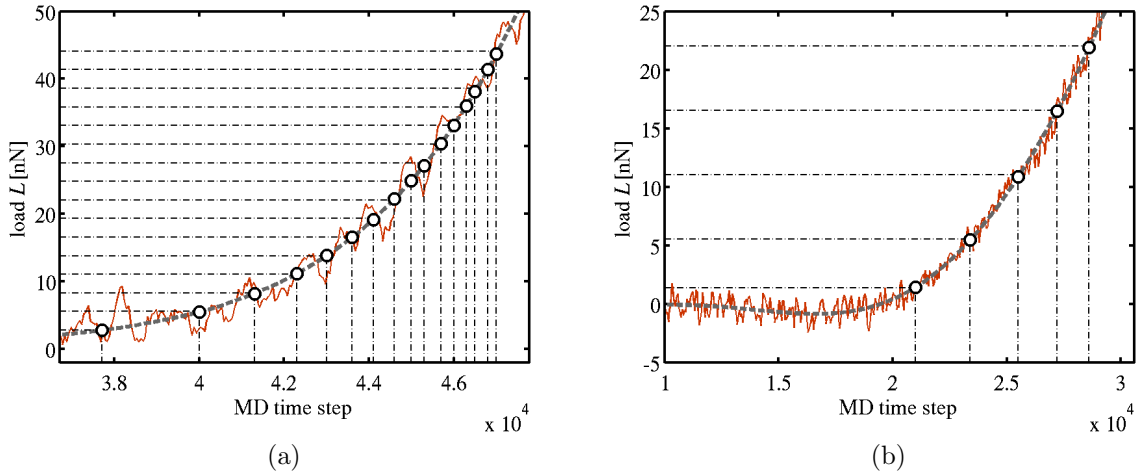


Figure 2.13: Compression curves (red) showing the load L as a function of the MD time step at a constant compression velocity of 35 m/s. (a) Semi-spherical asperity system. (b) Oleic acid system with high lubricant coverage and low roughness. The dashed grey curves are polynomial fits to the data.

of the system is continued well beyond the point where the maximum desired load occurs. Depending on the type and size of the system, the compression simulation will usually crash (because atoms are lost due to the occurring high forces) at a load of several hundred nN, which is roughly a factor 10 higher than the maximum load of interest for shear simulations ($\lesssim 50$ nN).

Initial MD configurations close to the loads at which the shear simulations should be carried out are then found by fitting a 7th–13th-order polynomial to the load-vs-time curve of the compression simulation, which at constant compression velocity is equivalent to a load-vs-approach curve, see Fig. 2.13. Since this relationship is bijective for the loads of interest considered in this work, a unique system configuration consisting of all atom positions and velocities can usually be found for any desired load. Horizontal dashed-and-dotted lines in Fig. 2.13 mark which loads should be simulated, black circles mark the best intersection points with the dashed grey fit according to the available time step resolution, which in turn yield the time steps with the initial configurations for the respective loads.

2.2.4 Shear

With the initial system configurations obtained as described above, individual simulation runs are carried out for each load/configuration to ensure maximum comparability over the load spectrum. For each of these runs, the system is initially kept at constant separation for 1.25 ps by keeping the rigid parts of both sliders stationary, thus allowing the lubricant molecules a short recovery after the sudden end of the compression. This constraint is

then released and replaced with the chosen constant load applied to the rigid part of the upper slider in $-z$ -direction, causing small oscillations in the slider separation. The shear velocity, applied to the same atoms as the load, is ramped from 0–4 m/s over 9.75 ps in 40 equal steps. After a dynamic equilibration period of 0.5 ns, which corresponds to 2 nm of sliding distance, steady-state sliding is assumed and simulation data is collected for analysis. Note the formation of an even sliding interface between the boundary lubricant layers in Fig. 2.14 (c). The chosen sliding velocity lies at the upper end of the range of technically relevant values while still being computationally feasible as well as easily and reliably thermostatable, cf. [82]. Unless stated otherwise, the data acquisition period after equilibration for all sliding simulations in this work lasts 2 ns.

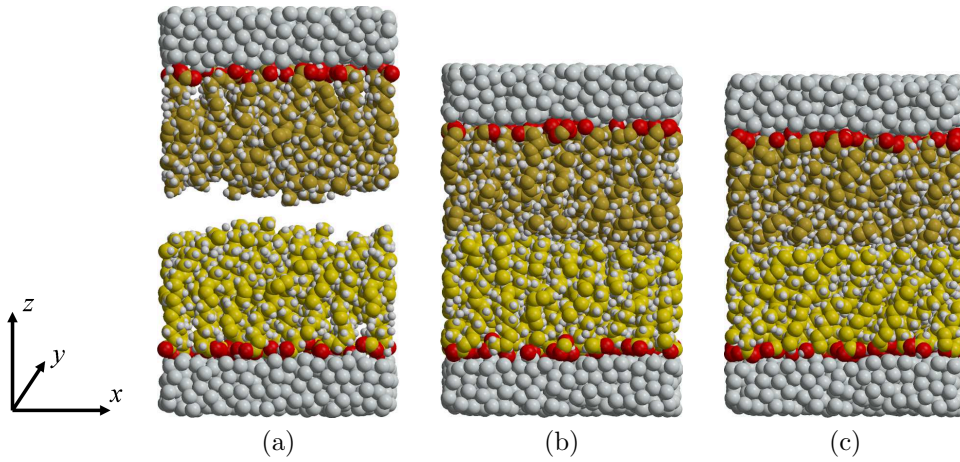


Figure 2.14: Compression and equilibration of the oleic acid system with 7×8 molecules per slider on a flat amorphous substrate. (a) Before compression. (b) Compressed to $L = 11.02$ nN (0.8 GPa). (c) After 0.5 ns of shear (dynamic equilibration period).

Chapter 3

Analysis Methods

In this chapter I will discuss methods which are applied to analyze the output data of MD simulations. First, I will propose a self-developed visualization scheme based on the smooth particle method which can be used for mapping discrete MD data to continuum as well as for defining and determining the asperity-asperity contact area in a mixed-lubrication simulation. I will then introduce the theoretical concepts and explain the numerical methods required for calculating contact forces in MD shear simulations. These forces and the contact area will then serve as a basis for obtaining the tribologically relevant system parameters. Finally, I will discuss certain ways to analyze and quantify lubricant (dis)order.

All theoretical and computational aspects covered in this chapter will be exemplified with data from three nanotribological systems, and some numerical results required to validate the employed methods are presented. These systems are prepared following the general guidelines for large substrates in chapter 2. The thickness of the amorphous Fe substrates is 1.96 nm, which is equivalent to 4050 atoms or ~ 12 monolayers of bcc Fe(100). Only stearic acid is used as boundary lubricant, and the lubricant coverage of 66 molecules per slider is the same for all three asperity types (semi-spherical, truncated cone and slanted pyramid). Snapshots of two of the three systems can be seen at the beginning of section 4.2. The 62 applied loads L range from 2.07 to 44 nN in steps of 0.69 nN, corresponding to nominal pressures between 75 MPa and 1.6 GPa in steps of 25 MPa.

3.1 Smooth Particle Post-processing (SPM)

Discrete simulation methods like MD are very well suited to follow the time development of atomistic systems. The data they produce are either of a global nature (energies, temperatures, etc.) or are relevant for individual atoms (positions, velocities). However, it is not computationally or even conceptually straightforward to calculate spatially continuous quantities based on discrete data.

Continuum mechanics (CM), on the other hand, is ideal for treating problems in which the properties of matter change continuously and differentially in space, but mesh-based methods do not treat individual particles very well. The introduction of particle-based methods to CM was initially an attempt to increase the efficiency of solving ordinary or partial differential equations [36]. When simulating anisotropic and/or inhomogeneous systems, the division of space into macroscopic pseudoparticles can greatly reduce the number of the degrees of freedom.

The smooth particle method (SPM), also called smoothed-particle hydrodynamics (SPH), has been used in astrophysics and hydrodynamics since the late 1970s [91]. It has also been used to study impact fracture in solids, where it is referred to as smooth-particle applied mechanics (SPAM) [36]. The method works by smoothing physical quantities known at irregular points in space over a typical spatial distance called the smoothing length via kernel functions such as Gaussians or cubic splines—for a recent overview see Ref. [92].

In this work, some of the concepts of SPM were taken up to devise a method which can map discrete MD data to continuum. This allows the definition and the calculation of the irregularly shaped contact area between two solid asperities $A_{\text{asp}}(L)$ in a fast and computationally reliable manner. Thus a novel application of SPM in conjunction with MD is introduced, which was so far restricted to improving the convergence of Ewald sums [93].

3.1.1 SPM basics

By partitioning the continuum into a finite number of representative subsystems of mass M_j and density ρ_j concentrated at $\vec{R}_j(t)$, the smooth-particle interpolation rule for an arbitrary quantity Q reads

$$Q(\vec{r}) = \sum_{j=1}^{\mathcal{N}} \frac{M_j}{\rho_j} Q_j w(\vec{r} - \vec{R}_j, h_j) = \sum_{j=1}^{\mathcal{N}} Q_j W(\vec{r} - \vec{R}_j, h_j) , \quad (3.1)$$

where Q_j is the value of Q for the j th pseudoparticle temporarily situated at \vec{R}_j , w is the smoothing kernel (weight function) which has the dimension of an inverse volume and should rapidly fall with distance, $W = wM_j / \rho_j$, and h_j stands for the spatial smoothing length defining the influence domain of w . In Eq. (3.1), the summation is performed over all pseudoparticles for which \vec{r} is in their kernel support.

This formalism may be used to map the discrete momentary positions \vec{r}_i of atoms as obtained from an MD simulation to a continuous representation. The definition of a material density

$$\rho(\vec{r}) = \sum_{i=1}^N w(\vec{r} - \vec{r}_i, h_i) , \quad (3.2)$$

where N is the total number of atoms in the simulation domain, is the simplest way to associate each atom with a smooth particle. The kernel function used throughout this work reads

$$w(\vec{r} - \vec{r}_i, h_i) = \frac{1}{h_i^3} \beta^{(3)}\left(\frac{\vec{r} - \vec{r}_i}{h_i}\right), \quad (3.3)$$

where $\beta^{(3)}(x)$ is a symmetric cubic B-spline [94] and acts as a partial material density distribution which does not take into account the mass of the individual atoms. Considering mass would not add any useful information in this case, as we are only interested in the spatial extent of the atoms, which does not depend on the number of protons and neutrons in the nucleus, but rather on the electronic configuration of an atom, which in turn has hardly any impact on the mass distribution. Thus the resulting smoothed pseudoparticles are continuous and time-dependent material densities characterized by a dimensionless smearing factor c_{smear} , which determines the amount of smoothing applied to the particle boundaries by setting the spatial smoothing length to $h_i = c_{\text{smear}} r_i^{(\text{LJ})}$. Here $r_i^{(\text{LJ})} = \sigma_i/2$ represents the Lennard-Jones radius of the atom i (with σ_i used in the sense as introduced in section 1.2), which is usually not identical for atoms of different types and may therefore be used as a measure for the atoms' spatial extent.

In practice, to transform an atomistic nano-system, where the coordinates of the atoms' center positions as well as the atom radii are known (see Fig. 3.1 (a)), to its SPM representation, a mesh of size d is laid over the simulation cell (Fig. 3.1 (b)). It must be fine enough ($d = 40$ pm throughout this work) to sufficiently resolve the continuous distribution of the total material density and to keep the mapping error of the atom centers below $d/2$, see the difference in position between the green dots and the green squares in Figs. 3.1 (a) and (b). Next, one generates a 3D-histogram for each atom type which counts the number of atom centers of that type in each mesh element. Since in our case the mesh size is considerably smaller than the interatomic distances, the only values occurring in these histograms are 0 and 1. They are then convolved in all spatial dimensions (using periodic boundary conditions) using the convolution kernel from Eq. (3.3), see Fig. 3.1 (c).

The resulting partial material densities of the different atom types can be superimposed in various combinations to yield scalar material density fields for any desired configuration. Surfaces and volumes of interest may then be visualized by plotting iso-surfaces at a chosen material density threshold ρ_0 (e.g. , the bold red curve in Fig. 3.1 (d)). So for visualizing the surfaces of the solids, one would superimpose the partial material densities of the upper and the lower slider and show the iso-surface at ρ_0 . Alternatively, for visualizing cavities in the lubricant, one would superimpose all available partial material densities, so the iso-surfaces at ρ_0 mark the locations where material is absent.

Note that this visualization of surfaces and volumes of various parts of the nanotribological system is to some extent similar to that used in the rolling ball algorithm to envelop macromolecules [95, 96]. In this work, however, an approximation of e.g. the total cavity volume at a given time is calculated by integrating over the volume which has a material density below the threshold ρ_0 . By integrating over the faces of the iso-surfaces, surface areas may be determined as well.

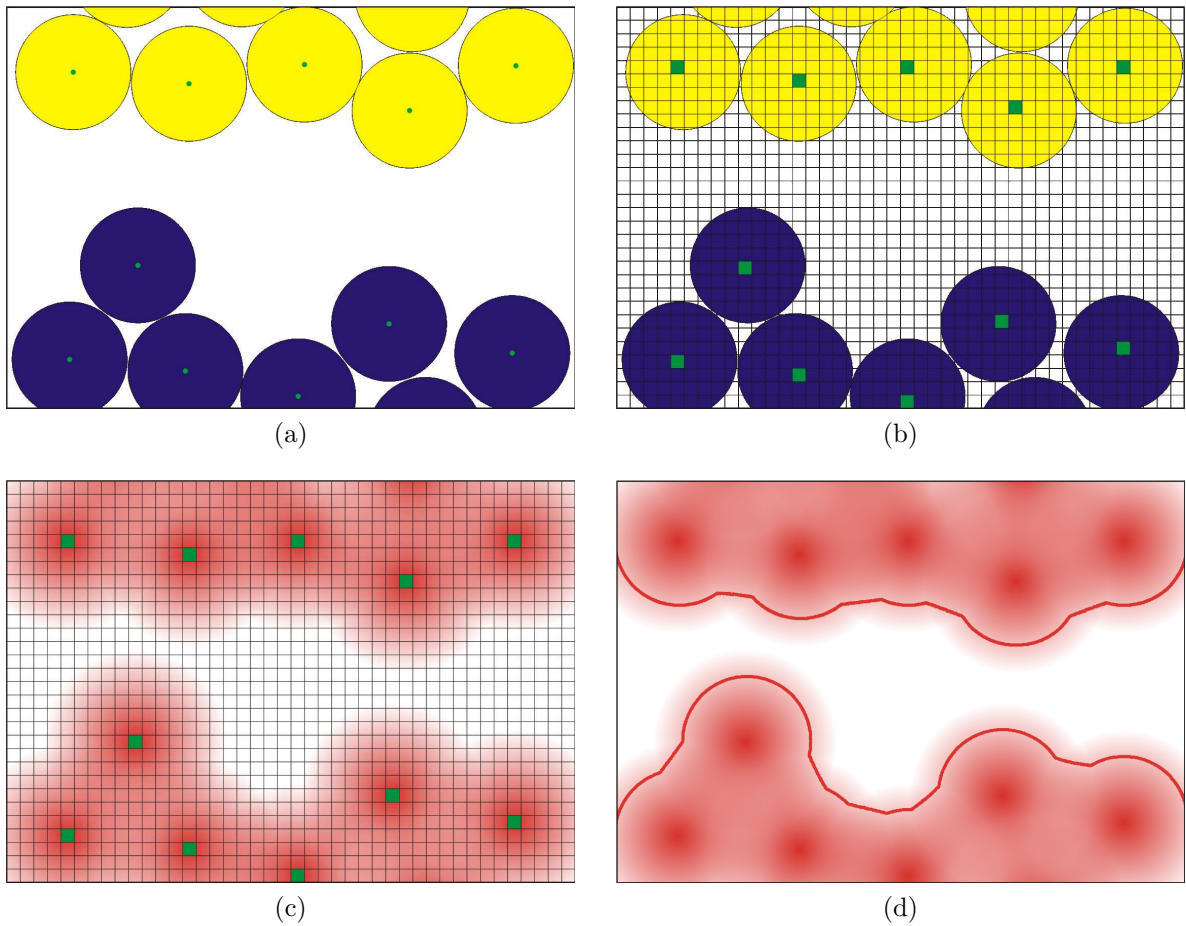


Figure 3.1: From MD to continuum with SPM, illustrated in 2D for identical surface atoms. (a) Discrete representation of MD nanosystem. (b) Meshing of the simulation box; the green squares are the atomic center elements. (c) Convolution of the center element distribution with the kernel function yields a quasi-continuous material density distribution. (d) Surface visualization as an iso-surface at the density threshold ρ_0 (bold red line).

3.1.2 Determination of SPM-parameters

To find a set of parameters c_{smear} and ρ_0 which is valid for all systems treated in this work, and to estimate the parameter dependence of $A_{asp}(L)$, a systematic parameter variation study was undertaken. As a first overview, $A_{asp}(L)$ was calculated with c_{smear} taking the values 1.1, 1.3, 1.5, 1.75, and 2.0, while ρ_0 was varied logarithmically between 0.001 and 0.09 \AA^{-3} . This was done for the semi-spherical asperity shape at a low load of 1.38 nN which favors cavities and a high load of 28.1 nN where asperity contact occurs. The results for $A_{asp}(L)$ were then compared to the data from the contact atom counting procedure discussed in section 3.1.4. At $L = 1.38 \text{ nN}$, where $A_{asp}(L)$ should be equal to zero, all parameter pairings which indicated asperity contact were discarded. At $L = 28.1 \text{ nN}$, only those pairings were kept in consideration which yielded contact times in rough agreement ($\pm 20 \text{ ps}$) with the counting algorithm. The remaining valid parameter sets suggest that there exists, with a certain bandwidth, a linear dependence of the general form

$$\rho_0 = k (c_{smear} - 1) . \quad (3.4)$$

From the initial data, the slope k of this curve was expected to be in the range 0.02–0.04 \AA^{-3} . To refine the first guess of $k = 0.03 \text{ \AA}^{-3}$, a second parameter study was carried out. This time, the fit parameter k was varied from 0.02 to 0.04 \AA^{-3} in steps of 0.002 \AA^{-3} , and c_{smear} was varied between 1.3 and 1.75 in steps of 0.05. Accordingly, ρ_0 ranged from 0.006 to 0.03 \AA^{-3} . The goal was to find the k producing values for $A_{asp}(L)$ that are independent of c_{smear} . For this, the relative error σ_{Aasp} of $A_{asp}(L)$ with respect to changes in c_{smear} was calculated as a function of k and the load L . Fig. 3.2 shows the results of this study for three different asperity types. The pronounced minimum value of σ_{Aasp} for $k \approx 0.024 \text{ \AA}^{-3}$, regardless of asperity shape, means that for this slope in the linear dependence between c_{smear} and ρ_0 , $A_{asp}(L)$ will typically change by no more than 1% of its value for any c_{smear} in the range of 1.3 to 1.75. This means that c_{smear} can be set to any value within these bounds producing a practicable degree of smoothing without any impact on the results obtained for $A_{asp}(L)$. Furthermore, σ_{Aasp} is small enough to be negligible and therefore does not enter the least-squares fitting procedure discussed in section 3.4.2. Unless stated otherwise in chapter 4, the values used throughout this work are $c_{smear} = 1.6$ and $\rho_0 = 0.0144 \text{ \AA}^{-3}$.

3.1.3 Estimation of the asperity contact area

Fig. 3.3 (a) shows an SPM-representation, as discussed in section 3.1.1, of the system with the truncated cone asperity at a load $L = 31.7 \text{ nN}$ at $t = 1.8 \text{ ns}$ during asperity contact. For calculating the asperity contact area, one can exploit the fact that the upper slider is sheared in x -direction only, so one may consider xz -slices of the system and find the shortest distance between the two non-Fe domains which occur during asperity contact. Fig. 3.3 (b) and (c) show two such xz -slices at the edge and the center of the contact zone, respectively. At those values for y where the two asperities touch, the Fe-domain (shown

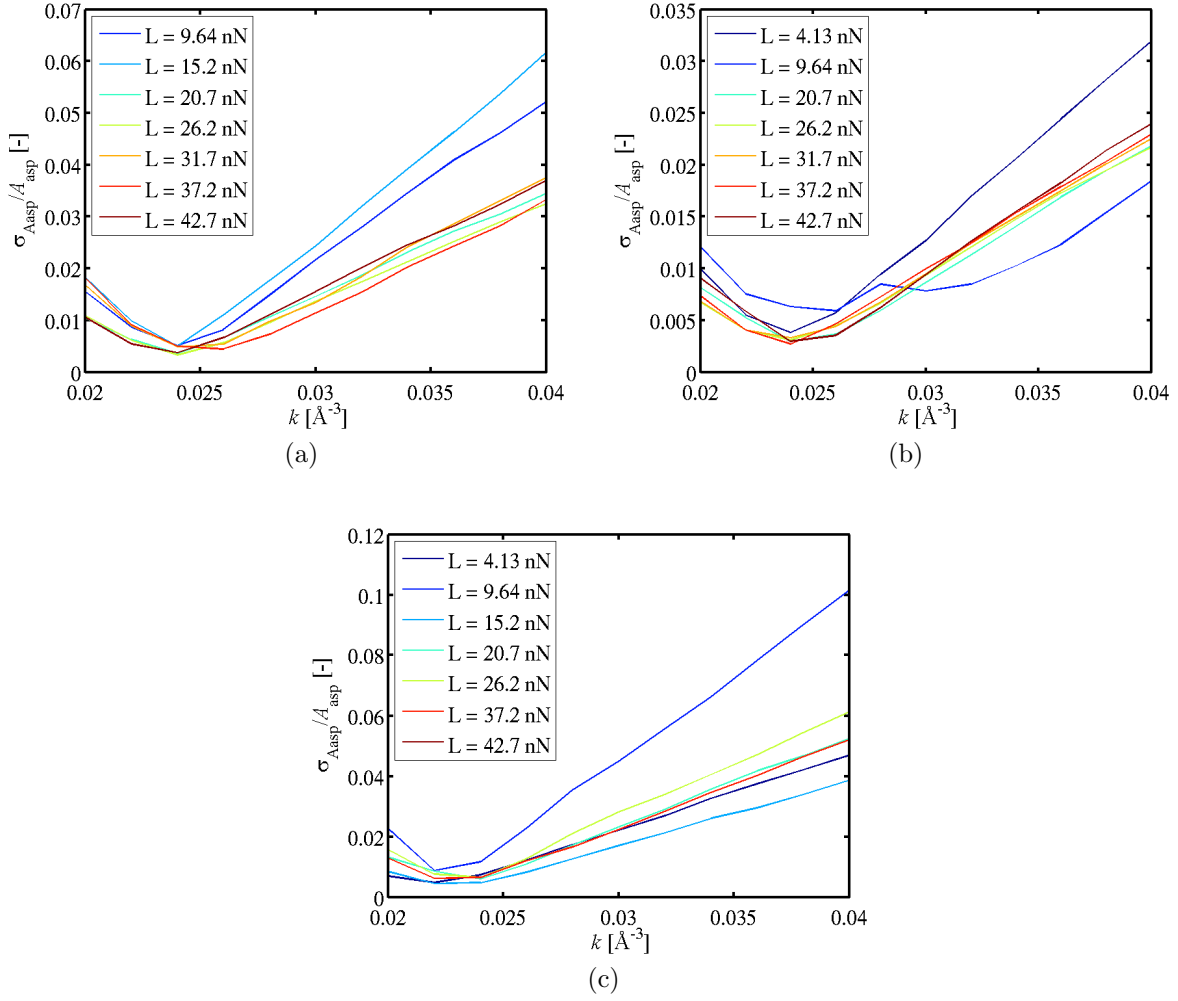


Figure 3.2: Relative error $\sigma_{A_{asp}}$ over c_{smear} of the asperity contact area $A_{asp}(L)$ as a function of the slope k from Eq. (3.4) and the load L , calculated for a semi-spherical (a), truncated cone (b), and slanted pyramid asperity (c). For each system, one load was omitted which led to high relative errors because there was no asperity contact.

in dark red) becomes simply connected, while the non-Fe-domain (i.e., the lubricant domain) splits in two. Each xz -slice contributing to the contact area is then treated in the following way:

- generate a logical mask where 0 represents Fe and 1 represents non-Fe areas
- identify the two separate non-Fe domains and treat the left (Ψ_1) and the right (Ψ_2) domain individually
- perform a Euclidean distance transform [97] on the binary matrix representation of Ψ_1 , thus assigning each matrix element a number that is the distance between it and the nearest nonzero element, then keep only those values which lie within Ψ_2 (and vice versa), see Fig. 3.3 (b) and (c)
- find the coordinates of the absolute minima in the two resulting matrices and calculate the length of the vector connecting them

The green lines in Figs. 3.3 (b) and (c) connect the two points of nearest approach, shown for the edge of the contact zone in Fig. 3.3 (b) and for its center in Fig. 3.3 (c). The coordinates of all points bounding the contact zone are now known, as shown by the green curve in Fig. 3.3 (d). This iso-surface has been made semi-transparent to allow a view of the far side of the contact zone. Summing up these segments multiplied by the length element in y -direction ($d = 40$ pm) yields the minimum cross-section of the contact zone, defining the asperity contact area $A_{\text{asp}}(L)$. Note that this approach does not find the zone of minimum contact boundary (as an elastic band would), and that it does not yield any information about the interior structure of the contact zone, since it neglects the asperity affiliation of the individual atoms. However, as will be shown in the following two sections, this greatly increases the reliability of the method since its accuracy does not depend on the success of determining the asperity affiliation of each atom at every moment during material transfer.

The limitations of this method would emerge if the solid bridge between the asperities deformed in y -direction in such a way that there exists no xz -slice through the system yielding a simply connected Fe area. However, since one constraint to all systems in this work is that the sliders may not move in y -direction, this is not an issue here.

3.1.4 Contact atom counting procedure (CCP)

The proposed smooth particle post-processing method may be validated via a comparison to the number of atoms participating in asperity contact, which is expected to be proportional to the asperity contact area $A_{\text{asp}}(L)$. In the contact atom counting procedure (CCP), two atoms belonging to different asperities are considered in contact if their centers are closer to each other than a certain contact distance d_{cont} . To define d_{cont} , which will depend on the lattice constant or the mixed Lennard-Jones radius, as well as the crystal structure and the temperature, one can study the radial distribution function of

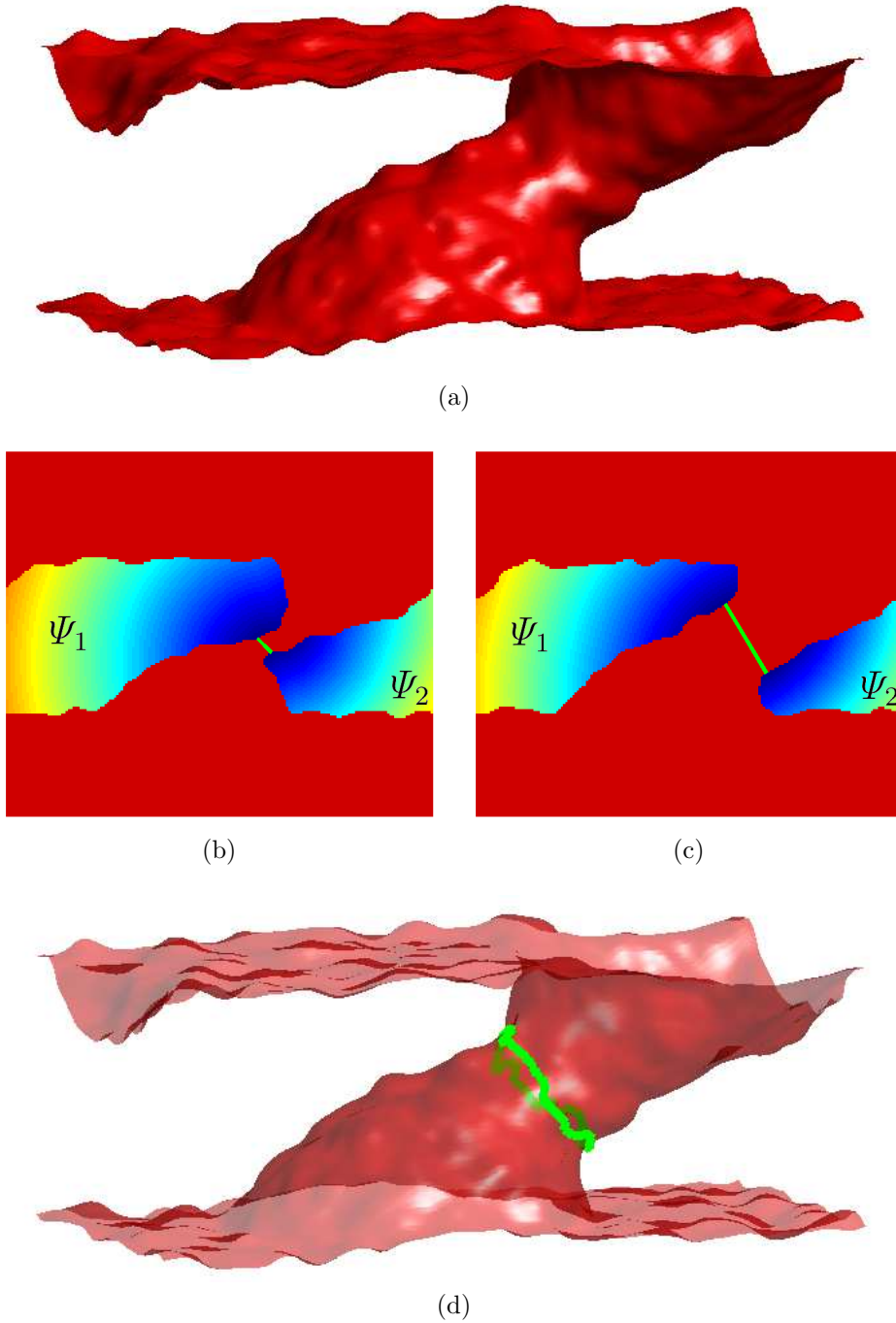


Figure 3.3: Calculation of $A_{\text{asp}}(L)$. (a) 3D SPM representation of an MD nanosystem during asperity contact. (b) Masked 2D Euclidean distance transform of an xz -slice near the edge and (c) near the center of the contact zone. The color code is rainbow-style with blue denoting low and red denoting high values. Straight green lines connect the minima. (d) Same as (a), but with the minima of the Euclidean distance transforms of all xz -slices within the contact zone connected by a green curve bounding the contact area $A_{\text{asp}}(L)$. The surface is semi-transparent to allow a view of the far side of the contact zone.

the substrates during a typical simulation run. In the systems in this work, the shortest distance between two Fe atoms at 300 K is 0.21 nm, while the first local minimum in the radial distribution function of amorphous Fe lies at about 0.33 nm, recall the green radial distribution function in Fig. 2.1 (d). To consider almost the entire first peak of this curve, which represents the immediate neighborhood of a given atom, as contact atoms, d_{cont} was set to 0.3 nm in this work. As can also be seen in Fig. 2.1 (d), this choice of d_{cont} would consider first and second neighbors in contact in a bcc lattice. However, some atoms usually transfer from one asperity to the other during the period of contact. In the following, these atoms will be referred to as deserters. For the above-mentioned contact criterion to work properly, care must therefore be taken that all deserters are associated with the correct asperity at every time step. Failure to change the asperity affiliation of a deserter will falsely lead to a higher number of contact atoms. This is most obvious at the end of the contact period, when the solid bridge has obviously already broken apart, but the CCP erroneously reports a constant number of atoms which are still in contact.

The distinction between deserters and non-deserters is made by analysing the difference between their initial and their final mean velocities in sliding direction Δv_x . For deserters, $\Delta v_x \approx \pm 4\text{m/s}$, while non-deserters have a value close to zero (see the bar graph in Fig. 3.4 (a)). Once a deserter has been identified, its asperity affiliation is changed at the time step when it first reaches half the sliding velocity. Fig. 3.4 (b) gives a breakdown of the number of contact atoms into contributions from the upper and the lower asperity, proving that they are equal on average, as expected. Also shown is the total share of deserters, which amounts to a little less than half in the beginning, and a little more than half towards the end of contact. From this one can conclude that atoms which are still in contact while the contact zone is breaking apart are slightly more likely to change asperity sides than those involved during contact formation. Figs. 3.4 (c) and (d) show the running average (window size $\Delta t_{\text{avg}} = 0.5\text{ ns}$) of the velocity component in shear direction of all contact atoms that are non-deserters or deserters, respectively. The bold lines illustrate the average change in advection velocity for atoms that are initially affiliated with the upper (yellow) or the lower (blue) asperity. It can be seen clearly that the average non-deserter is accelerated (or decelerated) by $\sim 1\text{ m/s}$ (1/4 of the sliding speed) during contact before finally relaxing onto its original slider.

The total number of deserters n_{des} is split up into those atoms that change from the lower asperity to the upper one and vice versa. Fig. 3.5 compares these two groups by showing the difference in unidirectional deserter numbers Δn_{des} divided by the total number of deserters for all three asperity types as a function of load. The spread of these values is quite high and there are instances where all deserters change asperities in the same direction, which is quite likely if only few atoms are involved in material transfer. However, when one calculates the cumulative sum of Δn_{des} over all loads and divides by the sum of n_{des} , one obtains 11%, 12%, and 15% for the semi-spherical, the truncated cone, and the slanted pyramid asperity, respectively. This could be either because not enough loads were simulated and the statistics are therefore not yet sufficient, or possibly due to the fact that the upper slider may oscillate in z -direction while the lower one is held

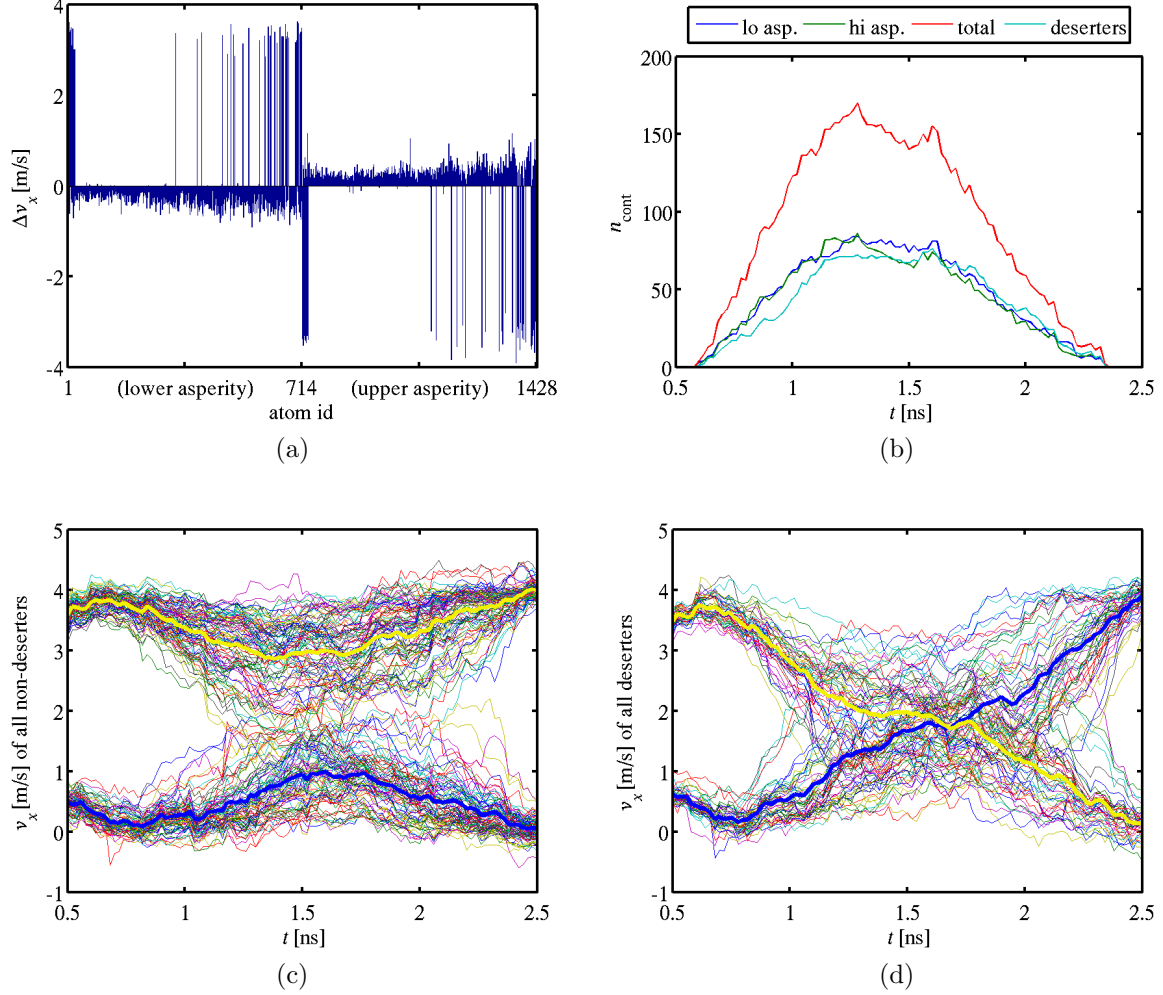


Figure 3.4: Material transfer in the system with the truncated cone asperity at $L = 31.7$ nN. (a) Bar graph of Δv_x for all asperity atoms; those with $\Delta v_x \approx \pm 4$ m/s transfer from one asperity to the other during the simulation. (b) Time development of the number of contact atoms belonging to the upper and the lower asperity compared to the total, as well as number of deserters participating in contact. (c) and (d) v_x of all non-deserting (c) and deserting (d) contact atoms (running average, $\Delta t = 0.5$ ns, the bold yellow and blue curves are asperity averages).

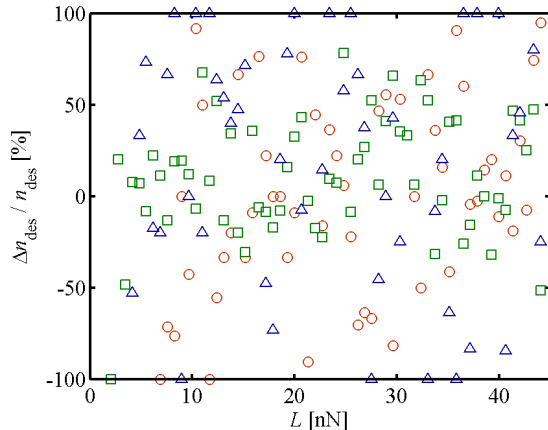


Figure 3.5: Directional material transfer balance in the systems with semi-spherical (red circles), truncated cone (green squares), and slanted pyramid asperities (blue triangles) as a function of load.

completely fixed in space. Generally, material transfer may still be considered sufficiently balanced.

Fig. 3.6 (a) shows the load-dependence of the number of contact atoms n_{cont} for the semi-spherical asperity calculated using the CCP. In this figure one also observes that while there is (almost) no contact at all until a load of about 4 nN is reached, the number of contact atoms increases rapidly until 15-20 nN where it starts to level off. Similar behavior can be seen for the truncated cone asperity in Fig. 3.6 (b), but here contact already occurs at the second simulated load. The flat top of this asperity type results in a much steeper increase of n_{cont} with load, so for $L > 10$ nN, the values remain virtually constant.

A comparison of the asperity contact duration with the total number of contact atoms and the number of deserters yields a quadratic dependence in the first case and a cubic one in the second, independently of asperity geometry, see Figs. 3.7 (a) and (b). One can therefore expect a linear dependence of the number of deserters on the product of the total number of contact atoms with the contact duration. Fig. 3.7 (c) shows that this is indeed the case independent of asperity shape, although data for different geometries are found in different regions along the linear fit with a correlation coefficient of 0.974. The data in Fig. 3.7 (b) also suggests that there seems to be a minimum contact duration of ≈ 360 ps to allow material transfer.

Finally, in Fig. 3.7 (d), the mean asperity contact area, calculated with the smooth particle approach is plotted over the mean number of contact atoms. The linearity of this relation is evident, where $A_{\text{asp}}(L) \simeq 0.02 \langle n_{\text{cont}} \rangle$ when $A_{\text{asp}}(L)$ is measured in nm^2 , and the correlation coefficient of 0.994 strongly supports the validity of the employed methods. As in Fig. 3.7 (c), this proportionality applies to all data points universally, irrespective of load and asperity geometry. Some deviations from the linearity of the data

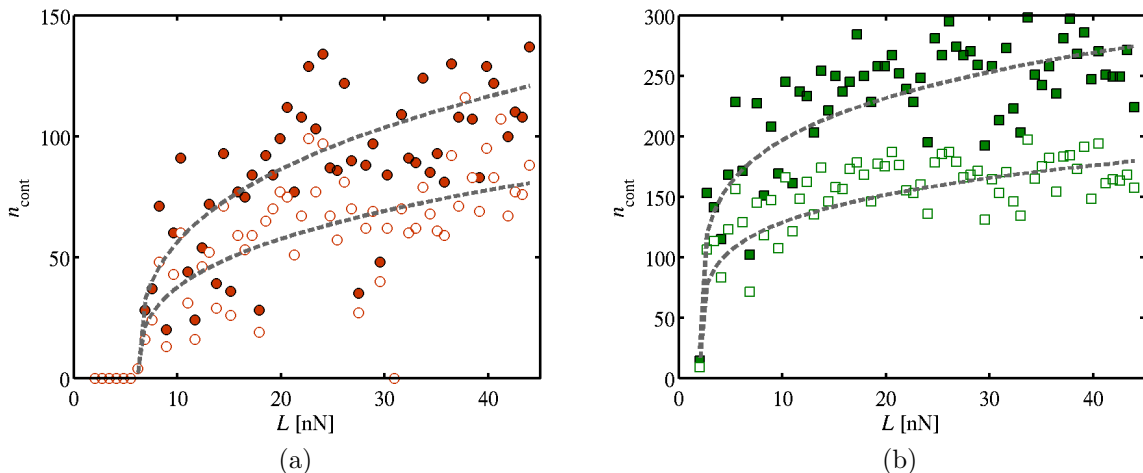


Figure 3.6: Number of contact atoms in the case of a nanotribological system with semi-spherical (a) and truncated-cone (b) asperities as a function of load. Empty symbols give the maximum instantaneous number of contact atoms, a value corresponding to the maximum of the red curve in Fig. 3.4 (b). Filled symbols give the total number of contact atoms, which is the sum of all atoms that are part of the contact zone at any time (not only at the time of maximum contact) during the simulation. The dashed curves only serve to guide the eye.

in Fig. 3.7 (d) may arise from the fact that the number of contact atoms is always an integer, while the asperity contact area can change continuously. This may lead to large relative errors for small asperity contact areas. Another difficulty lies in the exactness of coincidence of onset and end of asperity contact between the two calculation methods. In some cases, one method may indicate contact where the other does not, resulting in an infinite momentary error. All of these issues are greatly resolved by time-averaging, but they can still have an effect on the variance for small contact areas, which may lead to some of the deviations between the original and the fitted data in the load-vs.-friction behavior discussed in section 4.1.

3.1.5 Voronoi tessellation versus SPM

Voronoi tessellation (VT) is an alternative method to SPM for uniquely filling the space around some punctiform particles, called generators, based on their momentary positions [98]. The Voronoi cell (polyhedron) associated with a set of punctiform particles i ($i = 1, 2, \dots, N$) at a given moment t is the set of all spatial points $\vec{r}(t)$,

$$\Omega_i = \{ \vec{r}(t) \in \mathbb{R}^3 \mid |\vec{r}(t) - \vec{r}_i(t)| \leq |\vec{r}(t) - \vec{r}_j(t)|, \forall j \neq i \} , \quad (3.5)$$

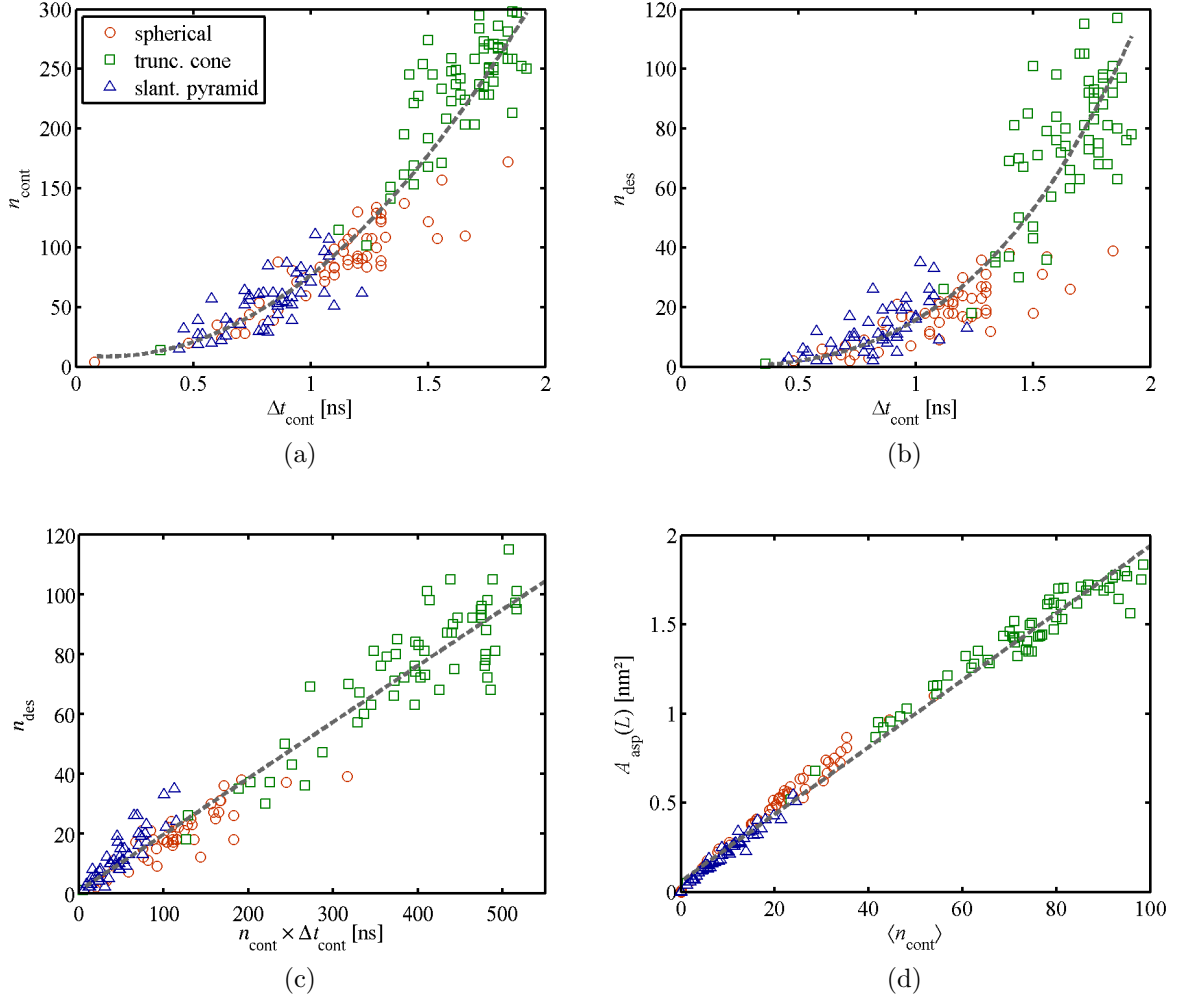


Figure 3.7: (a) The total number of contact atoms over the asperity contact duration for the three different asperity types. The dashed curve is a quadratic fit to the data. (b) The total number of deserters (atoms transferred to the other asperity during contact) over the asperity contact duration. The dashed curve is a cubic fit to the data. (c) The number of deserters as a function of the number of contact atoms and the contact duration. The dashed line is a linear fit to all data points. (d) Comparison of the results obtained using SPM and the CCP proposed in this work. The dashed line is a linear fit to all data points.

which are at least as close to the position $\vec{r}_i(t)$ of the i th particle as to any other particle $j \neq i$ situated at $\vec{r}_j(t)$ ($j = 1, 2, \dots, N$). The union of all so-resulting closed and convex Voronoi polyhedra then defines the VT,

$$\Omega_{\text{tot}} = \bigcup_{i=1}^N \Omega_i, \quad \text{such that} \quad \bigcap_{i=1}^N \Omega_i = 0. \quad (3.6)$$

Partitioning a finite spatial domain into Voronoi cells always yields information about the shape of dominant regions and about the relationship between neighbors, even when these are irregularly placed. These main features of VT make this construction method so successful in many research fields from natural to social sciences [99]. Particularly in condensed matter physics, the Voronoi construction is well established and has been widely used for eight decades leading to Wigner-Seitz cells in real space and Brillouin zones in reciprocal space. Both cells are translationally and rotationally invariant unit cells centered around a single lattice node in one of the dual spaces [100].

Thus, by performing a VT of two asperities coming into contact, those nearest neighbors within the solid-solid interaction zone which belong to different asperities and share a common face Σ_{ij} can be immediately identified,

$$\Sigma_{ij} = \Omega_i \cap \Omega_j \neq 0, \quad \forall i = 1, \dots, N_{\text{asp}}^{(k)}, \quad \forall j = 1, \dots, N_{\text{asp}}^{(l \neq k)} \quad (k, l = 1, 2), \quad (3.7)$$

where $N_{\text{asp}}^{(k)}$ denotes the total number of particles in one of the two asperities. Having determined these common faces, the asperity contact area $A_{\text{asp}}^{(\text{VT})}(L)$ due to the VT for a given load L is straightforwardly calculated as

$$A_{\text{asp}}^{(\text{VT})}(L) = \frac{1}{2} A \left(\bigcup_{i \neq j} \Sigma_{ij} \right) = \frac{1}{2} \sum_{i \neq j} A(\Sigma_{ij}), \quad (3.8)$$

with $A(\Sigma_{ij})$ denoting the area of Σ_{ij} .

Note that with the pairwise connection of the position of the punctiform particles whose Voronoi cells share a common edge, a dual structure of the VT is obtained. This structure can contain triangles and non-triangular polygons. If all non-triangular polygons are then partitioned into triangles with non-intersecting line segments, an additional tessellation called Delaunay triangulation results. Similarly to SPM, see section 3.1, the Delaunay triangulation can also provide a good estimate for the solvent-accessible surface around a solute and hence can be seen as a proper construction method to analyze contact areas in MD simulations [101].

The results obtained for $A_{\text{asp}}(L, t)$ with SPM were compared with those from a VT of the simulation cell. For the VT, the MD geometry data for each time step is modified in accordance with the CCP described in section 3.1.4, changing the asperity affiliation of those atoms which migrate from one asperity to the other during contact at the appropriate time step. This ensures that single atoms or small groups of atoms which have left their initial asperity cannot falsely contribute to $A_{\text{asp}}(L, t)$.

Next, a Delaunay triangulation of the simulation box is performed for each time step from which the Voronoi cells are calculated. Based on the modified affiliation tables mentioned above, those Voronoi cells are determined which belong to one asperity and neighbour a cell belonging to the other one.

When all contacting cells are known, the total Voronoi cell contact surface can be calculated. However, when comparing the time development of this quantity with the results obtained with SPM, one notices that the Voronoi method estimates the contact area $\sim 50\%$ higher on average and up to $\sim 250\%$ higher towards the end of contact, cf. Fig. 3.8 (a). This is hardly surprising, as the SPM-based $A_{\text{asp}}(L, t)$ is defined only by the contact zone's boundary, whereas the Voronoi-based $A_{\text{asp}}^{(\text{VT})}(L, t)$ is calculated taking into account the topography of the contact zone, where its roughness enters into the result.

The comparability between the results obtained with the two methods is greatly improved by calculating, weighting and averaging the normal vectors of all Voronoi cell faces contributing to the contact zone and then projecting the entire contact zone onto the average contact plane defined by the resulting normal vector. This eliminates the contact topography from the Voronoi approach. Fig. 3.8 (a) compares the results for the time development of the asperity contact area (for a load $L = 22.04$ nN and the semi-spherical asperity geometry) calculated with the Voronoi-method (total and projected) to those from SPM. On average, the asperity contact areas for the three methods are 2.009, 1.184, and 1.185 nm², respectively, so the relative difference between the projected Voronoi method and SPM is below 0.1% in this example.

Although the average and the maximum values for the asperity contact area in Fig. 3.8 coincide, one can see that at the onset of contact, SPM yields higher values than projected Voronoi, while from 1.5 ns on, the opposite is the case. This may be attributed to the increasing discrepancy between the position of the contact plane onto which the total Voronoi contact zone is projected and the position of the contact zone obtained with SPM, which does not take into account asperity affiliations, but only searches for the smallest solid cross-section. Figs. 3.8 (b) and (c) compare the time development of the normal vectors defining the average contact planes yielded by the two methods. The average SPM contact plane is a best-fit plane of the bounding points. Evidently, the two normal vectors behave very similarly until maximum contact is reached, but as the solid bridge between the asperities is drawn out horizontally, the SPM normal vector starts rotating about the y -axis and ends up pointing in x -direction when contact ends, while the Voronoi normal vector, though also slightly rotating about the y -axis, remains much more parallel to the z -axis (cf. Fig. 3.8 (f)). The differences in definition of the asperity contact area between the Voronoi method and SPM are therefore most evident towards the end of contact, explaining the behavior of the curves in Fig. 3.8 (a). The verticals in Figs. 3.8 (a)–(c) indicate the points in time which are shown in the 3D illustrations in the right column of Fig. 3.8.

Taking into account that SPM can estimate $A_{\text{asp}}(L, t)$ roughly ten times faster than the Voronoi method and that it does not require any asperity affiliation tables (which cannot always be reliably calculated, especially when considering multiple pass contact),

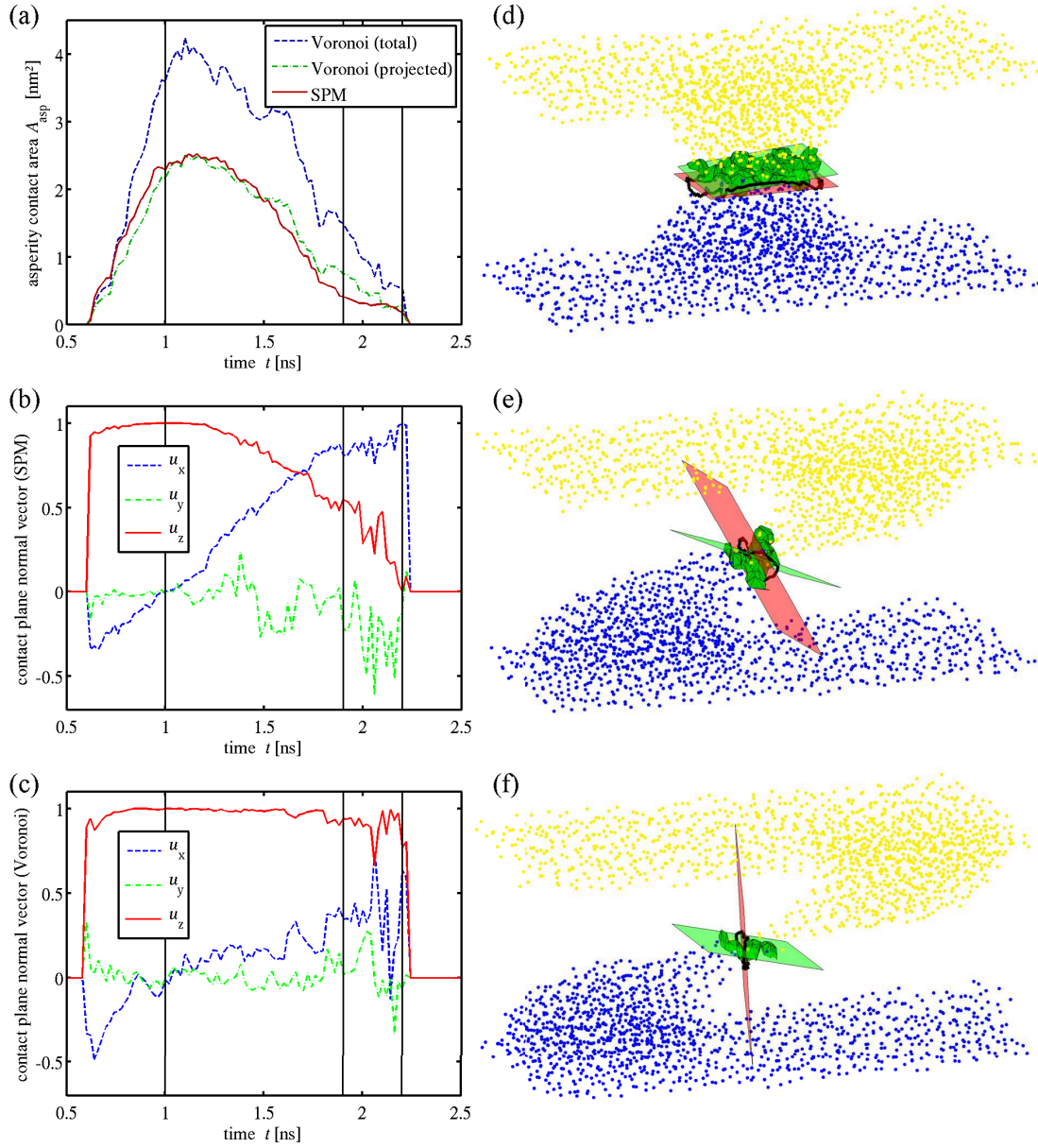


Figure 3.8: (a) Comparison of the results for the asperity contact area for a semi-spherical asperity obtained with the Voronoi method (total and projected) and SPM. (b) Time development of the components of the normalized normal vector \vec{u} of the average SPM contact plane. (c) Time development of the components of the normalized normal vector \vec{u} of the average Voronoi contact plane. (d)–(f) 3D-illustrations of the boundary lubrication simulation at 1.0, 1.9 and 2.2 ns, respectively, as indicated by the verticals in (a)–(c). Lubricant molecules have been deleted for clarity. Fe atoms of the lower slider are shown in blue, those of the upper slider in yellow. The Voronoi contact area is shown as a set of dark green polygons, encompassed by the average Voronoi contact plane as a light green rectangle. The boundary of the SPM contact zone is shown as a black band, with the average SPM contact plane shown as a light red rectangle.

it is absolutely feasible to calculate $A_{\text{asp}}(L, t)$ with SPM if no information about the internal structure of the contact zone is required.

3.2 Asperity Deformation During Solid-solid Contact

A simple discrete approach was taken for visualizing and quantifying deformation in the solid. The standard deviations of the positions σ_{pos} over a time interval of 2.5 ns, as well as the difference Δ_{pos} between the initial and the final positions (averaged over 0.2 ns each) were calculated for each Fe atom in the dynamically treated parts of both sliders. The sliding and compression movements of the upper slider were suppressed by subtracting the movement of one of the top rigid atoms at every time step. Fig. 3.9 (a) shows an illustration of which atoms are involved in plastic deformation (in x -direction) to which degree.

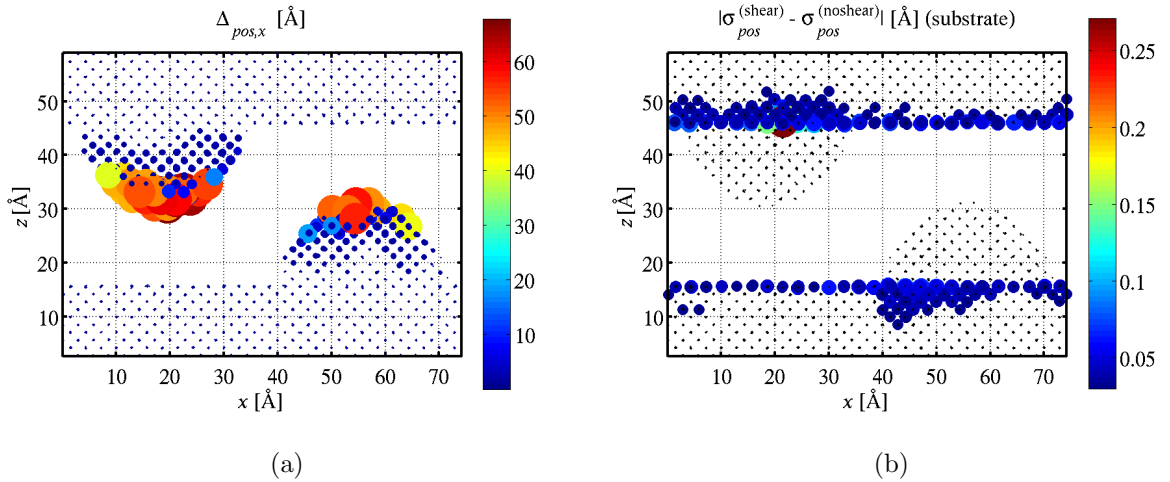


Figure 3.9: Visualization of the plastic deformation in the asperities (a) and of the elastic deformation in the substrates (b) of a crystalline bcc Fe tribosystem with a semi-spherical asperity. The size and color of the atoms, projected onto the system's initial configuration, denote the value of the quantity in the panel title. In the right panel, the deformation of the asperities is not shown in order not to overshadow the much smaller differences in the substrate.

An important application of this approach is to investigate up to which depth into the substrate the Fe atoms are involved in elastic deformation. By comparing σ_{pos} of the Fe atoms in a crystalline bcc Fe tribosystem ($L = 44.08$ nN, semi-spherical asperity), once sheared in x -direction and once without any shear, it is obvious up to which depth σ_{pos} is influenced by shear. Fig. 3.9 (b) shows an illustration of how $|\sigma_{pos}^{(\text{shear})} - \sigma_{pos}^{(\text{noshear})}|$ changes with depth for the substrate atoms. It can be seen that virtually anywhere within the

substrate, its value lies below 0.20 Å. Deeper than 5 ML into the substrate, the difference drops below 0.03 Å and becomes negligible. This is in good agreement with the rule of thumb proposed in Ref. [102] stating that the elastically treated substrate layer should be as thick as the asperity is wide.

3.3 Contact Force Averaging and Error Estimation

The contact forces are calculated by block-averaging over 50 time steps the net force exerted on the lower stratum of rigid atoms by all other atoms in the system. The obtained force vector $\mathbf{F}(t)$ can be decomposed into the load $L(t) = F_z(t)$, the friction force $F(t) = F_x(t)$ and the component perpendicular to the directions of load and shear $F_y(t)$.

3.3.1 Filtering methods

The time-resolved force output can be quite noisy due to thermal fluctuations, which can make filtering necessary. Depending on the resolution required for the respective analysis, several filtering methods come into consideration. The simplest one is the block average, where the data is divided into n_b blocks of length Δt such that $n_b \Delta t = t_{\text{run}}$ is the total run time of the simulation. All data points within a block are then arithmetically averaged.

Another simple filtering method is the central running average, where the block length Δt is chosen so that it contains an odd number n_{filt} of data points. If there are n_{run} force data points F_i in the entire simulation run, then the central running average data values can be calculated as

$$F_i^{(\text{avg})}(n_{\text{filt}}) = \frac{1}{n_{\text{filt}}} \sum_{k=i-I}^{i+I} F_k, \quad \text{with } I = \frac{n_{\text{filt}} - 1}{2} \in \mathbb{N}. \quad (3.9)$$

Since the central running average scheme averages over data from the past and the future, $i \in [I + 1, n_{\text{run}} - I - 1]$ and data is lost at the beginning and the end of $F_i^{(\text{avg})}$.

With the more sophisticated method of Gauss-windowing [103], the average of the force is obtained from its values modulated in amplitude by a Gauss-pulse

$$w_G(u) = e^{-\alpha u^2}, \quad u \in [0, 1], \quad (3.10)$$

whose duration is fixed in accordance with the desired time window

$$\Delta t = t_{\text{run}} \sqrt{\frac{\pi}{\alpha}}, \quad (3.11)$$

where α is a damping parameter which controls the amount of smoothing.

3.3.2 Statistical inefficiency

A general method to estimate the accuracy of any time-dependent quantity produced in MD simulations is based on the concept of the statistical inefficiency as introduced in Ref. [46]. For this, the data of the friction force $F(t)$ is split up into n_b blocks of length t_b such that $n_b t_b = t_{\text{run}}$, the total run time of the simulation. The variance of the mean values $\langle F \rangle_b$ of these blocks,

$$\sigma^2(\langle F \rangle_b) = \frac{1}{n_b} \sum_{b=1}^{n_b} (\langle F \rangle_b - \langle F \rangle_{\text{run}})^2 \quad (3.12)$$

is expected to be proportional to t_b^{-1} for large t_b , where $\langle F \rangle_{\text{run}}$ is the mean value over t_{run} . In order to estimate its behavior under these circumstances, one defines the statistical inefficiency as

$$s = \lim_{t_b \rightarrow \infty} \frac{t_b \sigma^2(\langle F \rangle_b)}{\sigma^2(F)} , \quad (3.13)$$

which represents the fraction of the sampled configurations that are statistically relevant. Here, $\sigma^2(F)$ is obtained assuming uncorrelated Gaussian statistics. This information may then be used to calculate the numerical accuracy of the run average as

$$\sigma_{\text{si}}(\langle F \rangle_{\text{run}}) = \left(\frac{s}{t_{\text{run}}} \right)^{1/2} \sigma(F) , \quad (3.14)$$

where the subscript in σ_{si} denotes that the standard deviation was calculated using the statistical inefficiency. The challenge lies with stably automating the task of identifying the plateau value of the limit in Eq. (3.13), as it may be obscured by many outliers for large values of t_b . This can be remedied by not allowing less than $n_b \simeq 20$ blocks so that fewer outliers are produced. One needs to be aware, however, that the error $\sigma_{\text{si}}(\langle F \rangle_{\text{run}})$ estimated in this way is a factor of ~ 2 smaller than when larger blocks are allowed, but this factor can be multiplied in afterwards. Thus the slightly compromised accuracy of the method to estimate the statistical inefficiency is by far outweighed by the benefit of higher reliability.

3.3.3 Time dependence of contact force

To justify the use of the method explained above to estimate the error made when calculating the contact forces, further efforts were undertaken to analyze the time dependence of $\mathbf{F}(t)$ over a simulation run. This was achieved by Gauss-windowing $\mathbf{F}(t)$, as briefly discussed in section 3.3.1, with the smoothing window size Δt varying from 0.1 ps to 10 ns and then calculating the standard deviation of the three force components. The results obtained for three systems with different asperity geometries at varying loads can be seen in Fig. 3.10. When comparing these figures, it is evident that the thick yellow lines for σ_y and σ_z which denote the load-averaged smoothing behavior of F_y and F_z are

almost independent of the asperity shape, whereas the load-averaged smoothing behavior of F_x as well as its variance with respect to the load vary considerably between the three systems.

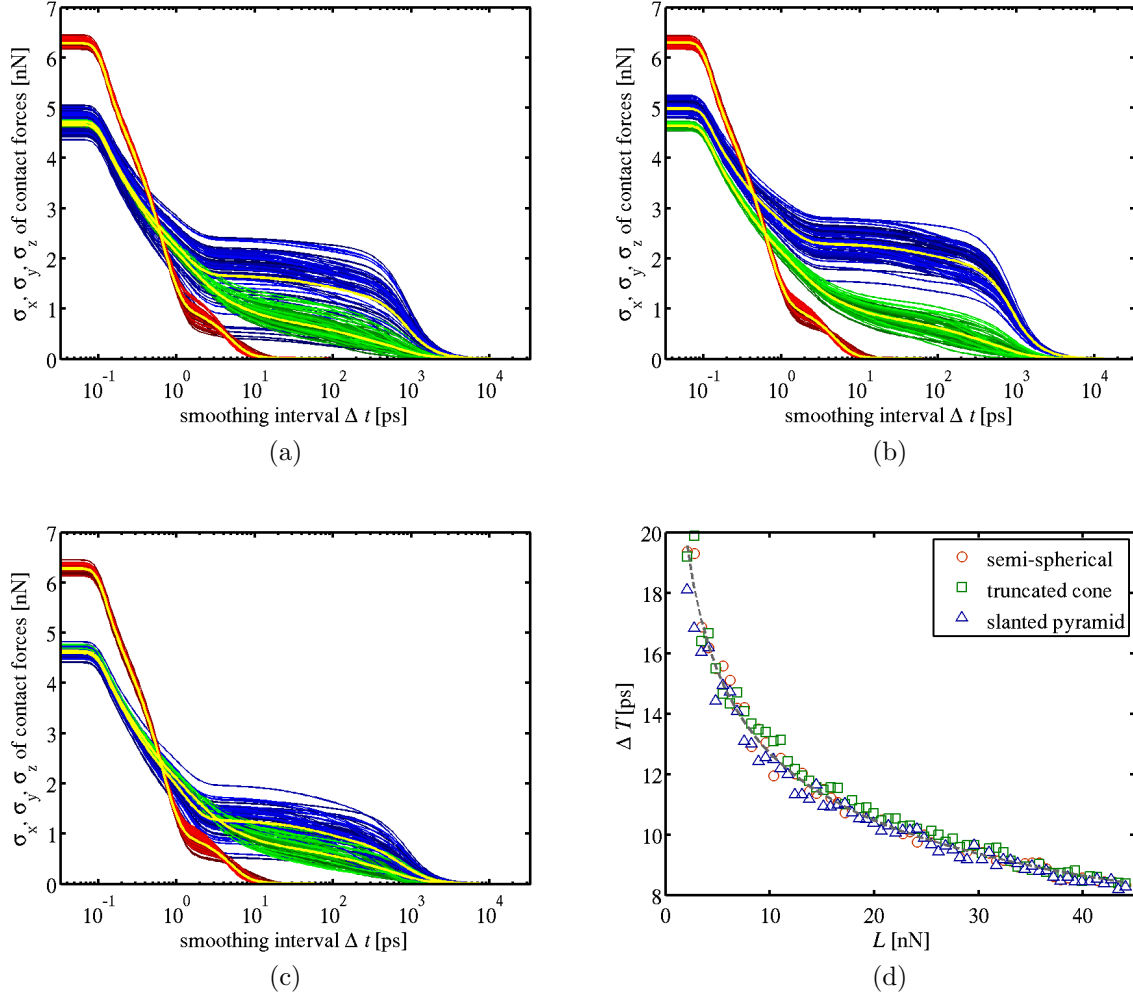


Figure 3.10: The standard deviations σ_x , σ_y and σ_z of the contact force components as a function of the smoothing window size Δt for a system with a semi-spherical (a), a truncated cone (b), and a slanted pyramid (c) asperity. Note the logarithmic scale on the Δt -axis. Curves in hues of blue, green and red denote σ_x , σ_y and σ_z , respectively, with darker curves for lower loads and lighter ones for higher loads. The thick yellow lines show the load-averaged behavior. Panel (d) shows the load dependence of the lubricant compressibility induced vibrations in z -direction. The dashed grey curve is an exponential fit to the data points.

For Δt smaller than 0.1 ps no changes can be expected as this value is smaller than the sampling interval of the contact forces, leading to constant values for σ_x , σ_y and σ_z on

the far left of Fig. 3.10 (a)–(c). Likewise, for Δt greater than 2.5 ns (the total simulation length), all force fluctuations must have averaged out, leading to vanishing values on the far right in all three figures. The area where Δt is increased from 0.1 to 1 ps is dominated by a sharp drop of all three components of σ as the thermal fluctuations in the contact force is filtered out. It can also be observed for all three asperity types that the initially higher value of σ_z decreases at a faster rate than the other two components, dropping below their values around $\Delta t = 0.5$ ps.

The unusual behavior of σ_z between $\Delta t = 1$ and $\simeq 10$ ps may be explained with some inertial vibrations in z -direction, which are likely due to the compressibility of the lubricant. According to a multiresolution analysis (MRA) [104] of the time-development of the z -dimension of the simulation box, these vibrations have a period of $\Delta T \simeq 8\text{--}20$ ps, decreasing non-linearly with the load, $\Delta T = 24.02 L^{-0.277}$, regardless of asperity shape, see Fig. 3.10 (d). It can therefore be assumed that this is a purely lubricant-related effect.

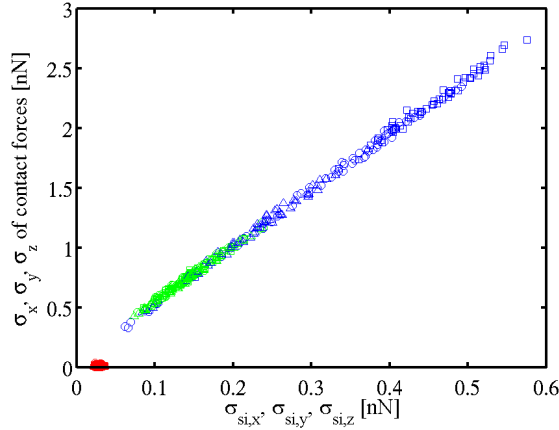


Figure 3.11: The errors σ_{si} obtained from the statistical inefficiency versus σ calculated as in Figs. 3.10 (a)–(c) for all three asperity types at $\Delta t = 32$ ps. Blue symbols denote the x , green the y , and red the z -components.

At $\Delta t = 3$ ps, the sharp decline of σ_x comes to a halt and its value remains almost constant for the next two orders of magnitude of Δt , which suggests that there are only very few features in the time development of the friction force which have typical times between 3 and 150 ps. At $\Delta t = 10$ ps, σ_z has virtually vanished, which means that the load may be considered constant with this amount of smoothing. Between $\Delta t = 5$ ps and 2.5 ns, σ_y decreases monotonously at a slower pace than for higher frequencies, and its value always lies between those of σ_x and σ_z .

In order to simplify the system parameter fitting procedure discussed in section 3.4.2, a value for Δt can be chosen so that the average value of σ_z/F_z lies below a threshold of 0.1% and may be treated as zero. At the same time, Δt should still be in the area where σ_x has its plateau, retaining as many features in the time development of $F_x(L, t)$ as possible, which leads to $\Delta t = 32$ ps. When comparing the values of σ_x , σ_y and σ_z to the

corresponding values of σ_{si} calculated via the statistical inefficiency based on Eq. (3.14), one immediately sees the excellent linear correlation for σ_x and σ_y , see Fig. 3.11. However, at very small values for σ_z , the corresponding statistical inefficiency does not vanish, as it still retains information about the unfiltered signal variance. Note also that the correlation does not remain constant for the three components of $\boldsymbol{\sigma}$ for all values of Δt (not shown here).

It can be concluded that for the systems treated in this work one may use the statistical inefficiency as a means for estimating the error in the friction force while at the same time neglecting any variance in the load, simplifying the fitting procedure for the system parameters discussed in section 3.4.2.

3.4 Constitutive System Parameters

Tribologists are usually interested in characterizing the frictional properties of a given system with the coefficient of friction μ . In the macroscopic world, this system parameter is often sufficient to calculate a friction force F from the applied load L with the Amontons-Coulomb friction law $F(L) = \mu L$ [28, 29]. For all its simplicity, this law proves very accurate in many applications.

In the nanoscopic regime, especially in mixed and boundary lubrication, one often has to deal with non-linearities as well as with adhesive effects that prevent F from vanishing when no load is applied. These issues require the introduction of one or two more load-independent system parameters which make it possible to predict friction forces.

For the systems treated in this work, I found it most convenient to use the three-term friction law proposed in this section. There may be certain cases where it simplifies to well-known special forms, but whenever lubrication gaps of the order of a few lubricant monolayers are present and/or solid-solid contact may occur—in short, for the atomistic treatment of mixed- or boundary-lubricated systems—this form of nanoscopic friction law always holds true.

3.4.1 Three-term kinetic friction law

The three-parameter friction law at nano-scale applied to the mixed- and boundary-lubricated tribosystems in this work reads

$$F(L) = F_0 + \tau A_{\text{asp}}(L) + \mu L , \quad (3.15)$$

where $F(L)$ is the load-dependent friction force. F_0 is the load-independent Derjaguin-offset ascribed to the presence of the lubricant (discussed later in this section), τ is the system's effective shear strength, $A_{\text{asp}}(L)$ is the time-averaged asperity contact area calculated using SPM as discussed in section 3.1.3, μ is the nanoscopic coefficient of friction, and L is the applied load. The Bowden-Tabor term $\tau A_{\text{asp}}(L)$ in Eq. (3.15) describes the

adhesion-controlled friction, whereas the Amontons-Coulomb term μL describes the load-controlled friction regime for nano-systems [105, 106]. This general form of the friction law will hold at any considered load and reproduces the observed load-vs.-friction behavior in all nanotribological systems in this work. It is valid independently of the particular form of the asperities or whether solid-solid contact occurs or not, i.e., for all values of the asperity contact area $A_{\text{asp}}(L) \geq 0$.

In contrast to the friction law given in [107], namely Eq. (3.15) written without F_0 , for this work it was absolutely necessary to consider a Derjaguin-offset $F_0 \neq 0$, because in all mixed lubrication cases investigated here, the friction force $F(L)$ does not vanish, even if both the load L and the asperity contact area $A_{\text{asp}}(L)$ do—as can be observed by inspecting the load-vs.-friction graphs in chapter 4. Of course there are nanotribological systems where such an offset of friction force either does not occur at $L = 0$ or is negligible [108], a selection of which will be discussed in section 4.3.

Note that the above three-term friction law obtained for boundary lubrication in nanotribological systems formally comprises other long-standing friction laws well known in literature. The Derjaguin-Amontons-Coulomb friction law, also referred to as modified Amonton’s law [109],

$$F(L) = F_0 + \mu L , \quad (3.16)$$

directly results from Eq. (3.15) by assuming $A_{\text{asp}}(L) = 0$. The offset F_0 was first identified and introduced to tribology by Derjaguin in 1934 based on purely theoretical considerations [30]. He argued that the presence of $F_0 \neq 0$ in the friction law is a direct consequence of the cohesion forces between molecules within the lubricant, see also Ref. [110]. $F_0 / \mu = L_0 \neq 0$ can be seen as an internal load L_0 caused by adhesion occurring in the presence of lubricant at load $L = 0$, and accordingly this term can be combined with the third one of Eq. (3.15) leading to $F_0 + \mu L = \mu(L_0 + L)$ as in Ref. [105].

The Bowden-Tabor friction law [37, 108], $F(L) = \tau' A_{\text{asp}}(L) = \tau A_{\text{asp}}(L) + \mu L$, on the other hand, immediately follows from Eq. (3.15) when $F_0 = 0$, and by introducing $\tau' = \tau + \mu L / A_{\text{asp}}(L)$ [111]. From the latter particular form of Eq. (3.15), a generalized Amontons-Coulomb friction law $F(L) = \mu' L$ may be written by introducing $\mu' = \mu + \tau A_{\text{asp}}(L) / L$ [112]. Both μ' and τ' would be system parameters if $A_{\text{asp}}(L) \sim L$, which may hold for macroscopic systems, but is definitely not the case in nanoscopic ones, see Fig. 3.6. It is also possible to ‘derive’ the last term of Eq. (3.15) starting from the second one by assuming that the shear strength τ obeys a linear pressure dependence and can therefore be written as $\tau + \mu p$, if $A_{\text{asp}}(L) \neq 0$ for all L considered, with $p = L / A_{\text{asp}}(L)$ [113, 114].

3.4.2 Least squares fitting procedure

Let us assume that the friction force $F(L)$ as a function of the load L is known from MD simulations, i.e., consider a finite set of values $F_i = F(L_i)$ ($i = 1, 2, \dots, n$) together with their corresponding errors σ_i made while calculating the friction forces as discussed

in section 3.3. Because these errors σ_i are normally distributed, the chi-square merit function [115],

$$\chi^2(F_0, \tau, \mu) = \sum_{i=1}^n \left[\frac{F_i - F_0 - \tau A_{\text{asp}}(L_i) - \mu L_i}{\sigma_i} \right]^2 \quad (3.17)$$

achieves its minimum with respect to the parameters F_0 (offset of the friction force), τ (effective shear strength) and μ (coefficient of friction), and for the given nanotribological system the three-term friction law in Eq. (3.15) holds. This means that the partial derivatives of $\chi^2(F_0, \tau, \mu)$ with respect to F_0 , τ and μ following from Eq. (3.17) all vanish, and in order to determine these parameters one has to solve the system of linear equations

$$\begin{pmatrix} S_{11} & S_{12} & S_{13} \\ S_{12} & S_{22} & S_{23} \\ S_{13} & S_{23} & S_{33} \end{pmatrix} \begin{pmatrix} F_0 \\ \tau \\ \mu \end{pmatrix} = \begin{pmatrix} S_1 \\ S_2 \\ S_3 \end{pmatrix}, \quad (3.18)$$

for example by using Cramer's rule, where

$$\left\{ \begin{array}{l} S_{11} = \sum_{i=1}^n \frac{1}{\sigma_i^2}, \quad S_{12} = \sum_{i=1}^n \frac{A_{\text{asp}}(L_i)}{\sigma_i^2}, \quad S_1 = \sum_{i=1}^n \frac{F_i}{\sigma_i^2} \\ S_{22} = \sum_{i=1}^n \frac{A_{\text{asp}}^2(L_i)}{\sigma_i^2}, \quad S_{13} = \sum_{i=1}^n \frac{L_i}{\sigma_i^2}, \quad S_2 = \sum_{i=1}^n \frac{F_i A_{\text{asp}}(L_i)}{\sigma_i^2} \\ S_{33} = \sum_{i=1}^n \frac{L_i^2}{\sigma_i^2}, \quad S_{23} = \sum_{i=1}^n \frac{L_i A_{\text{asp}}(L_i)}{\sigma_i^2}, \quad S_3 = \sum_{i=1}^n \frac{F_i L_i}{\sigma_i^2} \end{array} \right. . \quad (3.19)$$

In addition, the error (variance) made by estimating F_0 , τ and μ based on Eq. (3.17) can be evaluated using Eq. (3.19) and

$$\left\{ \begin{array}{l} \sigma_{F_0}^2 = \sum_{i=1}^n \sigma_i^2 \left(\frac{\partial F_0}{\partial F_i} \right)^2 = \frac{1}{\Delta} (S_{22} S_{33} - S_{23}^2) \\ \sigma_{\tau}^2 = \sum_{i=1}^n \sigma_i^2 \left(\frac{\partial \tau}{\partial F_i} \right)^2 = \frac{1}{\Delta} (S_{11} S_{33} - S_{13}^2) \\ \sigma_{\mu}^2 = \sum_{i=1}^n \sigma_i^2 \left(\frac{\partial \mu}{\partial F_i} \right)^2 = \frac{1}{\Delta} (S_{11} S_{22} - S_{12}^2) \end{array} \right., \quad (3.20)$$

where $\Delta = S_{11}S_{22}S_{33} + 2S_{12}S_{13}S_{23} - S_{11}S_{23}^2 - S_{13}^2S_{22} - S_{12}^2S_{33}$ is the determinant of the system of linear equations in Eq. (3.18). Apart from Eq. (3.20), the goodness of fit can be expressed in terms of the upper incomplete gamma function

$$Q\left(\frac{\chi^2}{2}, \frac{n_{\text{dof}}}{2}\right) = 1 - \frac{1}{\Gamma\left(\frac{n_{\text{dof}}}{2}\right)} \int_0^{\frac{\chi^2}{2}} e^{-t} t^{\frac{n_{\text{dof}}}{2}-1} dt, \quad (3.21)$$

where χ^2 is the chi-square merit function from Eq. (3.17) and n_{dof} is the number of degrees of freedom, i.e., the number of data points (loads) minus the number of fit parameters, and Γ is the gamma function. Values of Q close to 1 denote high fit quality.

Note, however, that this least squares fitting of F_0 , τ and μ properly works only as long as at least one load L_i exists such that $A_{\text{asp}}(L_i) \neq 0$. When $A_{\text{asp}}(L_i) = 0$ for all loads L_i considered, Derjaguin's friction law Eq. (3.16) holds and Eq. (3.18) is replaced by

$$\begin{pmatrix} S_{11} & S_{13} \\ S_{13} & S_{33} \end{pmatrix} \begin{pmatrix} F_0 \\ \mu \end{pmatrix} = \begin{pmatrix} S_1 \\ S_3 \end{pmatrix}, \quad (3.22)$$

which, once solved, provides F_0 and μ with an error (variance) of

$$\begin{cases} \sigma_{F_0}^2 = \sum_{i=1}^n \sigma_i^2 \left(\frac{\partial F_0}{\partial F_i}\right)^2 = \frac{S_{33}}{S_{11}S_{33} - S_{13}^2} \\ \sigma_{\mu}^2 = \sum_{i=1}^n \sigma_i^2 \left(\frac{\partial \mu}{\partial F_i}\right)^2 = \frac{S_{11}}{S_{11}S_{33} - S_{13}^2} \end{cases}, \quad (3.23)$$

but the shear strength τ remains undefined. In this special case, one can also use the corresponding chi-square merit function,

$$\chi^2(F_0, \mu) = \sum_{i=1}^n \left(\frac{F_i - F_0 - \mu L_i}{\sigma_i}\right)^2 \quad (3.24)$$

as an approach for measuring the goodness of fit when no solid-solid contact occurs during sliding.

3.4.3 Convergence of constitutive system parameters

In order to get a feeling for the convergence of the system parameters, it was studied how many data points n_p (i.e. loads) it takes for F_0 , μ , and τ to stabilize. For this, at first $n_p = 3$ points were chosen at random out of the $n_{p,\text{max}} = 62$ available for each asperity type, with the constraint that the first and the last data points are always the ones at the lowest and highest load, respectively. The chi-square fitting procedure was then carried out $n_r = 10^4$ times for every random data configuration, after which the mean value

and the standard deviation for each system parameter was recorded. This procedure was repeated with $3 < n_p \leq 62$ in order to see general trends for the convergence of the system parameters.

The detailed results of the convergence study is shown for the spherical asperity shape in Figs. 3.12 (a), (c), and (e). The round yellow markers at $n_p = 16$ represent the fitting results for 16 equally spaced data points. Looking at F_0 , the mean value drops steeply for small n_p , has a pronounced minimum at $n_p = 6$ and then rises monotonically, seemingly reaching saturation at $n_p = n_{p,max}$. The variance remains almost constant for $10 < n_p < 50$, then drops and reaches zero by default for $n_p = n_{p,max} = 62$. The upper limit of the error bars reach the final value of F_0 at $n_p \approx 30$, from which point on the obtained system parameter is statistically indistinguishable from the converged value. Note, however, that the average value of F_0 lies only 16% below the converged F_0 even at $n_p = 6$, where convergence is poorest.

By contrast, the mean value of μ rises steeply for small n_p and has a flat maximum at $n_p = 14$ which lies within 3% of the final value. The variance decreases monotonically. The convergence of τ , although with a different sign, is marked by similar behavior: its mean value drops steeply at first but reaches a value within 2% of its final value by $n_p = 15$, and the variance decreases monotonically as well.

Figs. 3.12 (b), (d), and (f) compare the convergence progress of the three system parameters with respect to the values at $n_p = n_{p,max} = 62$ for all considered asperity types. Note the different scaling of the vertical axes. One immediately sees that F_0 , μ , and τ are affected by errors due to incomplete convergence which are of the orders 15%, 3%, and 5%, respectively. It can therefore be concluded that μ is a very stable parameter which may be estimated with good accuracy using only few load points. The system parameter τ also converges quickly but generally its quality depends on the occurrence of solid-solid contact, cf. the green curve in Fig. 3.12 (f), where a single load point with no asperity contact slows convergence. Finally, F_0 converges somewhat more slowly, and its variance does not decrease monotonically. Its quality is strongly dependent on solid-solid contact, or rather its absence in some points, especially at low loads, cf. the green curve in Fig. 3.12 (b). Based on $n_p = 16$ load points, one can expect to obtain values within a 5% range around the converged value for μ (and τ , as long as sufficient solid-solid contact occurs). As can be seen in Fig. 3.12 (a), the value for F_0 may lie closer to the converged value than the general trend indicates as long as the evaluated load points are evenly distributed, but it may also be off by $\pm 12\%$ in the worst case.

3.5 Lubricant Analysis

Order in the lubricant film seems to play a considerable role in the occurrence of the load-independent force offset F_0 featured in all of the friction laws discussed in this work. To investigate this, the correlations between the individual atoms of the carbon backbones of the lubricant molecules were visualized using dynamic cross-correlation maps (DCCMs).

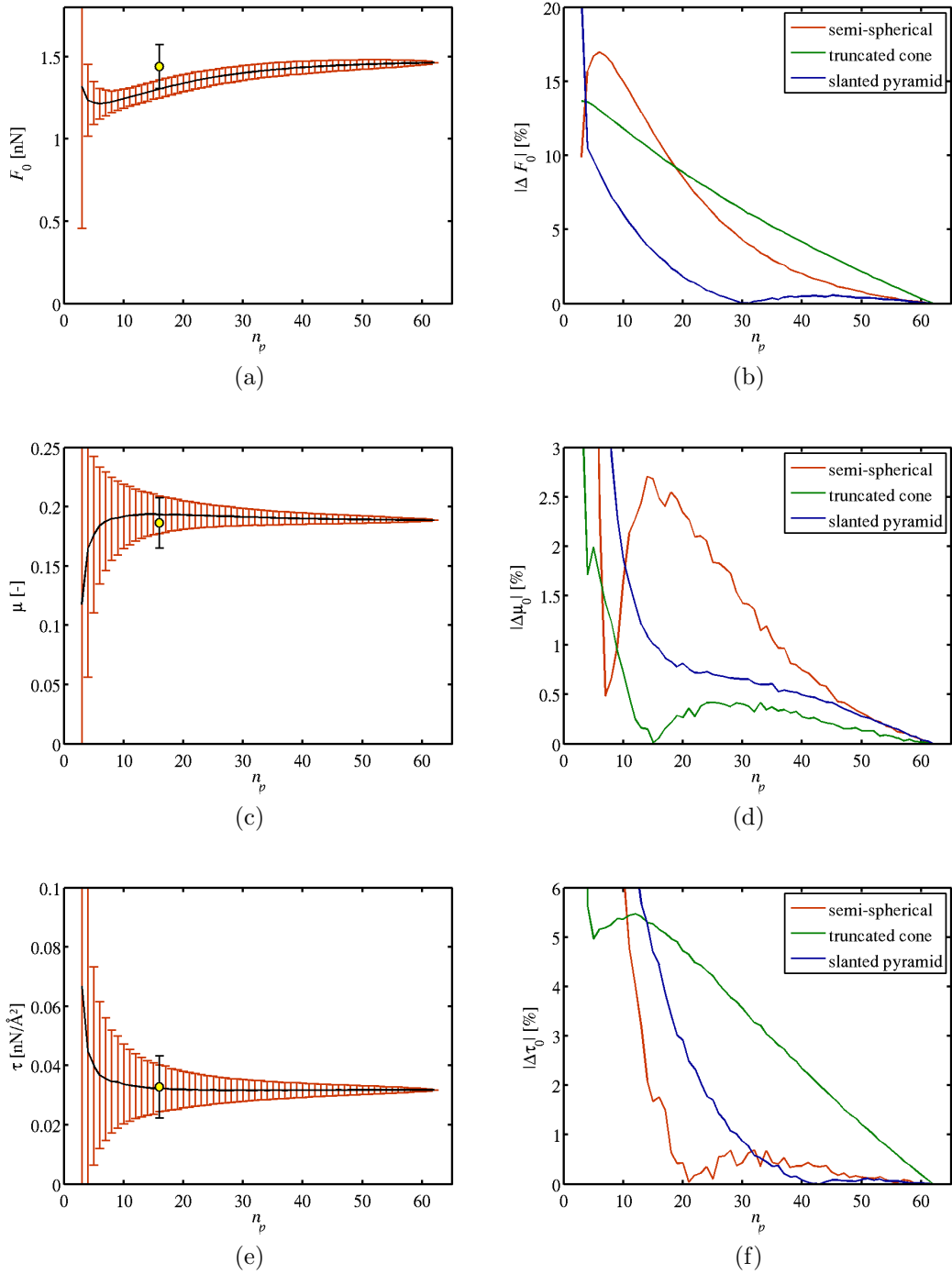


Figure 3.12: Convergence of the chi-square fitting procedure with increasing number of data (i.e. load) points n_p for the system parameters F_0 (a), μ (c) and τ (e). The left column shows data from the system with the semi-spherical asperity. The right column compares the progress of convergence of the system parameters for all three asperity types in percent of the values at $n_p = 62$.

The matrices which these represent have the additional advantage of directly serving as a basis for calculating various forms of configurational entropy, which may be interpreted as a single scalar quantification of certain aspects of lubricant order.

3.5.1 Dynamic cross-correlation maps (DCCM)

In terms of the position vectors $\vec{r}_i(t)$ and $\vec{r}_j(t)$ at the moment t of two “particles” (e.g. atoms, groups of atoms, residues, atomic clusters, etc.), the corresponding element c_{ij} of the covariance matrix is defined as [116]

$$c_{ij} = \langle \Delta \vec{r}_i \cdot \Delta \vec{r}_j \rangle = \langle (\vec{r}_i - \langle \vec{r}_i \rangle) \cdot (\vec{r}_j - \langle \vec{r}_j \rangle) \rangle = \langle \vec{r}_i \cdot \vec{r}_j \rangle - \langle \vec{r}_i \rangle \cdot \langle \vec{r}_j \rangle , \quad (3.25)$$

where \cdot denotes the scalar product of two vectors and angle brackets indicate time averages taken over the last period $T - t_0$ of the simulations (T is the final, t_0 the initial moment) [117], for example,

$$\left\{ \begin{array}{l} \langle \vec{r}_i \cdot \vec{r}_j \rangle = \frac{1}{N_t} \sum_{n=1}^{N_t} \vec{r}_i(t_0 + n\Delta t) \cdot \vec{r}_j(t_0 + n\Delta t) \\ \langle \vec{r}_k \rangle = \frac{1}{N_t} \sum_{n=1}^{N_t} \vec{r}_k(t_0 + n\Delta t) , \end{array} \right. , \quad (k = i, j) \quad (3.26)$$

with

$$N_t = \left\lceil \frac{T - t_0}{\Delta t} \right\rceil \in \mathbb{N} ,$$

and Δt being the time between two consecutive time frames or alternatively the period used for partial averaging. Thus the diagonal elements of this covariance matrix,

$$c_{kk} = \langle \Delta \vec{r}_k^2 \rangle = \langle |\Delta \vec{r}_k|^2 \rangle = \langle \vec{r}_k^2 \rangle - \langle \vec{r}_k \rangle^2 = \langle |\vec{r}_k|^2 \rangle - |\langle \vec{r}_k \rangle|^2 , \quad (3.27)$$

give the mean-square fluctuations of the k th particle. The normalized covariance matrix, called the dynamic cross-correlation matrix C , is formed by the cross-correlation coefficients [116, 117],

$$C_{ij} = \frac{\langle \Delta \vec{r}_i \cdot \Delta \vec{r}_j \rangle}{\sqrt{\langle \Delta \vec{r}_i^2 \rangle \langle \Delta \vec{r}_j^2 \rangle}} = \frac{c_{ij}}{\sqrt{c_{ii} c_{jj}}} \in [-1, +1] , \quad (3.28)$$

such that positive values of C_{ij} quantify the correlated motion between particles i and j , whereas negative valued cross-correlation coefficients indicate the degree of anticorrelation in the motion of two particles and C_{ij} s for extrema ∓ 1 mark perfectly (anti)correlated particle pairs. Furthermore, the so introduced cross-correlation coefficient C_{ij} —also known as Pearson correlation coefficient r [$\Delta \vec{r}_i, \Delta \vec{r}_j$]—is a suitable measure for time-correlated motions along a straight line by means of the relative displacements (i.e. , it properly detects

linear correlations), but fails to provide any information about the magnitude of fluctuations, which can range from small local oscillations to large-scale collective motions [118]. Moreover, correlations occurring due to parallel oscillations of the same period shifted in phase by 90° , or perpendicular oscillations in phase of identical period, which yields a vanishing C_{ij} , are not distinguished either [119]. For these reasons, complementary to C_{ij} [118], it is also useful to separately investigate the average maximum magnitude

$$r_{\text{abs}} [\Delta\vec{r}_i, \Delta\vec{r}_j] = \frac{\langle |\Delta\vec{r}_i| |\Delta\vec{r}_j| \rangle}{\sqrt{\langle \Delta\vec{r}_i^2 \rangle \langle \Delta\vec{r}_j^2 \rangle}} \quad (3.29)$$

and the average colinearity

$$r_{\text{dir}} [\Delta\vec{r}_i, \Delta\vec{r}_j] = \left\langle \left| \frac{\Delta\vec{r}_i}{|\Delta\vec{r}_i|} \cdot \frac{\Delta\vec{r}_j}{|\Delta\vec{r}_j|} \right| \right\rangle . \quad (3.30)$$

In accordance with common practice in the known literature, $\vec{r}_i(t)$ indicates the instantaneous position of the backbone carbon atoms in the lubricant molecules [116, 117, 118, 119].

Per definition, the dynamic cross-correlation matrix C introduced in Eq. (3.28) is a symmetric one. Therefore, when these matrices are shown graphically as so-called dynamic cross-correlation maps (DCCM), for sake of clarity and redundancy-free representation, commonly in the upper triangle only the negative correlation values are displayed, whereas in the lower triangle the positive correlation values only [119]. Beyond the time interval considered for averaging in Eq. (3.26), the current magnitude and structure of the correlation values in DCCM strongly depends on the global and unique reference frame used as well. For example, translating this initial frame by \vec{R} , the element c'_{ij} of the covariance matrix with respect to the new reference frame,

$$\begin{aligned} c'_{ij} &= c_{ij} + \langle \vec{R} \cdot \vec{R} \rangle - \langle \vec{R} \rangle \cdot \langle \vec{R} \rangle \\ &\quad - \langle \vec{r}_i \cdot \vec{R} \rangle + \langle \vec{r}_i \rangle \cdot \langle \vec{R} \rangle - \langle \vec{r}_j \cdot \vec{R} \rangle + \langle \vec{r}_j \rangle \cdot \langle \vec{R} \rangle , \end{aligned} \quad (3.31)$$

differs from that in Eq. (3.25) whenever \vec{R} is time-dependent, e.g. , identical with the center of mass of the entire system,

$$\vec{R}_{\text{CM}}(t) = \frac{1}{m} \sum_i m_i \vec{r}_i(t) , \quad \text{where } m = \sum_i m_i , \quad (3.32)$$

see Ref. [120].

3.5.2 Configurational entropy

The configurational entropy S_{config} contributes to the total entropy S_{tot} of a given system along with S_{tr} and S_{rot} , which arise from the translational and rotational motions of the

entire system. As it is related to the position of the constituent particles only, S_{config} can be seen as a measure of the structural order within the system and is decomposed into a conformational S_{conf} and vibrational S_{vib} part. Independently of which contribution S to S_{tot} is to be determined for a given positional configuration $\boldsymbol{\xi}$ of particles, it can be (at least in principle) directly obtained from the Shannon entropy of the joint probability density function (PDF) $\rho_{\boldsymbol{\xi}}(\boldsymbol{\xi})$ assigned to $\boldsymbol{\xi}$ [121],

$$S = -k_{\text{B}} \int d\boldsymbol{\xi} \rho_{\boldsymbol{\xi}}(\boldsymbol{\xi}) \ln \rho_{\boldsymbol{\xi}}(\boldsymbol{\xi}) , \quad (3.33)$$

where k_{B} is the Boltzmann constant. Note that for the sake of simplicity, in this expression of S the temperature-dependent constant occurring due to the integration of the PDF in the momentum space was omitted. Unfortunately, except for some model systems, $\rho_{\boldsymbol{\xi}}(\boldsymbol{\xi})$ cannot be computed with sufficient accuracy using MD simulations [122], and hence the expression on the right hand side of Eq. (3.33) has to be approximated.

The most commonly used approach for the PDF in literature is the quasi-harmonic (Gaussian) one where the canonical PDF $\rho_{\boldsymbol{\xi}}(\boldsymbol{\xi})$ of particle motion is assumed in the form of a multivariate Gaussian probability density [123],

$$\rho_{\boldsymbol{\xi}}(\boldsymbol{\xi}) = \frac{1}{(2\pi)^{3N/2} \det \mathbf{C}} \exp \left(-\frac{1}{2} \Delta \boldsymbol{\xi}^{\text{T}} \mathbf{C}^{-1} \Delta \boldsymbol{\xi} \right) . \quad (3.34)$$

Here the $3N \times 3N$ covariance (super)matrix \mathbf{C} is given by

$$\mathbf{C} = \langle \Delta \boldsymbol{\xi} \Delta \boldsymbol{\xi}^{\text{T}} \rangle , \quad \text{with} \quad \Delta \boldsymbol{\xi} \Delta \boldsymbol{\xi}^{\text{T}} = \begin{pmatrix} \mathbf{C}_{11} & \mathbf{C}_{12} & \dots & \mathbf{C}_{1j} & \dots & \mathbf{C}_{1N} \\ \mathbf{C}_{21} & \mathbf{C}_{22} & \dots & \mathbf{C}_{2j} & \dots & \mathbf{C}_{2N} \\ \vdots & \vdots & \ddots & \vdots & & \vdots \\ \mathbf{C}_{i1} & \mathbf{C}_{i2} & \dots & \mathbf{C}_{ij} & \dots & \mathbf{C}_{iN} \\ \vdots & \vdots & & \vdots & \ddots & \vdots \\ \mathbf{C}_{N1} & \mathbf{C}_{N2} & & \mathbf{C}_{Nj} & & \mathbf{C}_{NN} \end{pmatrix} \quad (3.35)$$

and N the total number of particles in the investigated system. The two-particle covariance matrix \mathbf{C}_{ij} , on the other hand, is written as

$$\mathbf{C}_{ij} = \Delta \boldsymbol{\xi}_i \Delta \boldsymbol{\xi}_j^{\text{T}} = \begin{pmatrix} \Delta x_i \Delta x_j & \Delta x_i \Delta y_j & \Delta x_i \Delta z_j \\ \Delta y_i \Delta x_j & \Delta y_i \Delta y_j & \Delta y_i \Delta z_j \\ \Delta z_i \Delta x_j & \Delta z_i \Delta y_j & \Delta z_i \Delta z_j \end{pmatrix} , \quad (i, j = 1, \dots, N) \quad (3.36)$$

by compacting the Cartesian components of the positional deviations into a single column matrix,

$$\Delta \boldsymbol{\xi} = \boldsymbol{\xi} - \langle \boldsymbol{\xi} \rangle = \begin{pmatrix} \Delta \boldsymbol{\xi}_1 \\ \vdots \\ \Delta \boldsymbol{\xi}_i \\ \vdots \\ \Delta \boldsymbol{\xi}_N \end{pmatrix} , \quad \text{where} \quad \Delta \boldsymbol{\xi}_i = \begin{pmatrix} \Delta \xi_i^{(1)} \\ \Delta \xi_i^{(2)} \\ \Delta \xi_i^{(3)} \end{pmatrix} \equiv \begin{pmatrix} \Delta x_i \\ \Delta y_i \\ \Delta z_i \end{pmatrix} . \quad (3.37)$$

Thus any element of the covariance (super)matrix \mathbf{C} reads

$$\langle \Delta \xi_i^{(k)} \Delta \xi_j^{(l)} \rangle = \langle \xi_i^{(k)} \xi_j^{(l)} \rangle - \langle \xi_i^{(k)} \rangle \langle \xi_j^{(l)} \rangle, \quad \text{with } k, l = 1(x), 2(y), 3(z) \quad (3.38)$$

and the angle brackets denote time averages taken over the data acquisition period of the simulation.

Particularizing Eq. (3.34) for the center of mass of the entire system consisting of N particles of different masses m_i , recall Eq. (3.32), Eq. (3.33) immediately yields for the translational contribution to the total molar entropy [124],

$$S_{\text{tr}} = R \ln \left[\prod_{k=1}^3 \left(\frac{e^2 m k_B T}{\hbar^2} \right)^{1/2} \sigma_{\xi^{(k)}} \right], \quad (3.39)$$

where $\hbar = h/(2\pi)$ stands for the reduced Planck constant, e denotes the Euler number, R is the universal (molar) gas constant, T the constant temperature, and σ_x , σ_y and σ_z are the principal root-mean-square (RMS) fluctuations of the center of mass. Similarly, the rotational contribution to the molar entropy S_{rot} is obtained as [120]

$$S_{\text{rot}} = R \ln \left[8\pi^2 \left(\frac{e k_B T}{2\pi \hbar^2} \right)^{3/2} (I_x I_y I_z)^{1/2} \right] \quad (3.40)$$

by assuming a symmetry number of unit magnitude and inserting the principal moments I_x , I_y and I_z as eigenvalues of the inertia tensor \mathbf{I} built up with the elements [125]

$$I_{kl} = \sum_{i=1}^N m_i \left(\langle \xi_i' \rangle^2 \delta_{kl} - \langle \xi_i'^{(k)} \rangle \langle \xi_i'^{(l)} \rangle \right), \quad \text{where } k, l = 1(x), 2(y), 3(z), \quad (3.41)$$

determined using the atomic positions ξ_i' with respect to the center of mass of the investigated system.

The common idea behind various estimations for S_{vib} known in literature is the mapping of each vibrational eigenmode of the analyzed system onto a well-defined frequency of a simple one-dimensional quantum harmonic oscillator [126]. In order to proceed in this manner, one has to first diagonalize the symmetric covariance (super)matrix \mathbf{C} from Eq. (3.35) using an orthogonal coordinate transformation, i.e.,

$$\mathbf{T}^T \mathbf{C} \mathbf{T} = \mathbf{\Lambda} = \text{diag}(\lambda_1, \lambda_2, \dots, \lambda_{3N}). \quad (3.42)$$

Here the diagonal matrix $\mathbf{\Lambda}$ consists of $3N$ eigenvalues $\lambda_J \equiv \lambda_j^{(l)}$ labelled with a composite index $J = 3(j-1) + l$, for example, such that the J th column of the $3N \times 3N$ orthogonal matrix \mathbf{T} is the eigenvector corresponding to λ_J , called principal mode, and \mathbf{T}^T is the transpose of \mathbf{T} . Usually, the eigenvectors are also normalized, or alternatively one applies an orthonormal transformation in Eq. (3.42) from the beginning to diagonalize \mathbf{C} [127]. At

the end of the diagonalization, each eigenvector describes a single correlated displacement of particles relative to $\langle \boldsymbol{\xi} \rangle$ in a multidimensional space, and the eigenvalue associated with this eigenvector gives the amplitude of the collective motion, i.e. , the mean-square fluctuation in the direction of that principal mode [117]. Commonly, eigenvalues are arranged in decreasing order $\lambda_1 \geq \lambda_2 \geq \dots \geq \lambda_{3N} \geq 0$ and the corresponding normalized eigenvectors \mathbf{V}_J ($J = 1, \dots, 3N$) as columns form the orthonormal matrix \mathbf{V} , which is equal to \mathbf{T} only if the transformation in Eq. (3.42) is an orthonormal one. Note that by diagonalizing \mathbf{C} as defined in Eq. (3.35), three eigenvalues will correspond to the collective translational motion, three more to the rotation, and only the remaining $3N - 6$ modes are purely vibrational.

Once the $3N - 6$ vibrational eigenmodes are identified, the frequencies ω_J of the associated one-dimensional quantum harmonic oscillators are calculated relating these to the classical variance $\langle \Delta \boldsymbol{\xi}_J^2 \rangle = \lambda_J$ of the uncorrelated particle coordinates using the equipartition theorem,

$$m_J \omega_J^2 \lambda_J = k_B T, \quad (J = 1, 2, \dots, 3N - 6), \quad (3.43)$$

which reasonably well holds as long as $\hbar \omega_J \ll k_B T$. Summing up the analytically known vibrational entropies $S_{\text{vib}}^{(J)}$ directly obtained from Eq. (3.33) for all associated quantum harmonic oscillators $J = 1, 2, \dots, 3N - 6$, immediately results in the vibrational contribution to the total molar entropy within the quasi-harmonic approach as [128]

$$S_{\text{vib}} = R \sum_{J=1}^{3N-6} \frac{\beta \hbar \omega_J}{\exp(\beta \hbar \omega_J) - 1} - R \sum_{J=1}^{3N-6} \ln [1 - \exp(-\beta \hbar \omega_J)], \quad (3.44)$$

where $\beta = (k_B T)^{-1}$. Schlitter in his *ad hoc* quantum mechanical approximation [129] provided an upper bound to S_{vib} and hence to the configurational entropy in most systems with

$$\begin{aligned} S_{\text{Schl}} &= \frac{1}{2} R \sum_{J=1}^{3N-6} \ln \left[1 + \frac{e^2}{(\beta \hbar \omega_J)^2} \right] = \frac{1}{2} R \ln \left[\prod_{J=1}^{3N-6} \left(1 + \frac{k_B T e^2}{\hbar^2} m_I \lambda_I \right) \right] \\ &\simeq \frac{1}{2} R \ln \det \left(\mathbf{1} + \frac{k_B T e^2}{\hbar^2} \mathbf{M} \boldsymbol{\Lambda} \right) = \frac{1}{2} R \ln \det \left(\mathbf{1} + \frac{k_B T e^2}{\hbar^2} \mathbf{M} \mathbf{C} \right) > S_{\text{vib}}, \end{aligned} \quad (3.45)$$

which correctly reproduces both the quantum and the classical mechanical limits of the entropy ($S_{\text{Schl}} = 0$ if $T \rightarrow 0$, and $S_{\text{Schl}} \propto \ln T$ if $T \rightarrow \infty$) and is not singular even if the $3N \times 3N$ covariance (super)matrix \mathbf{C} is [130]. In Eq. (3.45) $\mathbf{1}$ represents the $3N \times 3N$ unit matrix and \mathbf{M} represents the mass (super)matrix introduced as formed with $\mathbf{M}_{ij} = m_i \delta_{ij} \mathbf{1}_{3 \times 3}$, δ_{ij} is the Kronecker symbol and $\mathbf{1}_{3 \times 3}$ the 3×3 unit matrix. Note also that $\mathbf{M} \mathbf{C} = \mathbf{M}^{1/2} \mathbf{C} \mathbf{M}^{1/2}$ is the mass-weighted covariance (super)matrix built up with the Cartesian components of the mass-weighted positional deviations, namely $\mathbf{M}_{ii}^{1/2} \mathbf{C}_{ij} \mathbf{M}_{jj}^{1/2} = (\sqrt{m_i} \Delta \boldsymbol{\xi}_i) (\sqrt{m_j} \Delta \boldsymbol{\xi}_j)^T$ [127], which, once diagonalized, leads to mass-weighted mean-square fluctuations along the eigenvectors [131]. By removing the translational and rotational motions of the center of mass of the system by a least squares fit,

for example, S_{Schl} will differ from that of the unfitted system, but its value may still be used for relative comparisons with S_{vib} [132].

Chapter 4

Results and Discussion

This chapter presents three studies in which the analysis methods outlined in chapter 3 are applied to the data obtained from nano shear simulations. Sections 4.1 and 4.2 both deal with mixed lubrication in the nanoscopic regime, where boundary lubricants fail, direct asperity contact occurs, and the three-term kinetic friction law applies in its entirety. Finally, section 4.3 is a large-scale case study of the friction performance of different boundary lubricants under various conditions and with varied substrate roughness. Nine of these systems are then analysed further in an attempt to correlate a particular system parameter of the three-term kinetic friction law, the Derjaguin offset F_0 , to the configurational entropy of the boundary lubricant.

4.1 SPM Analysis of Boundary Lubricant Failure

In this section I will exemplify how the SPM post-processing method discussed in section 3.1 may be used for a detailed analysis of the non-linear load-vs.-friction behavior in mixed-lubrication shear simulations of rough nano-systems [38, 39]. The focus in this study lies on forcing boundary lubricant failure at high loads, which leads to direct asperity-asperity contact, while avoiding it at low loads, thus retaining boundary lubrication as in Refs. [32, 33, 34]. These conditions are ideal for testing the stability and accuracy of SPM for calculating contact areas, as well as for ensuring the applicability of the three-term kinetic friction law at high load-resolution.

4.1.1 Specific system setup

The three nanotribological systems featured in this section are prepared following the general guidelines for large substrates in chapter 2 and can be viewed in Fig. 4.1. The thickness of the amorphous Fe substrates is 0.82 nm, which is equivalent to 1352 atoms or ~ 4 monolayers of bcc Fe(100). This substrate thickness may lie slightly below the recommended minimum as discussed in section 3.2, but since the main interest here lies

with the asperity tip deformation and comparative studies on systems with thicker substrates have given similar results, it can be considered sufficient. Only stearic acid is used as boundary lubricant. The procedure for generating pre-worn boundary lubricant films described in section 2.2.2 is applied to the three simulated asperity types (semi-spherical, truncated cone, and slanted pyramid) in order to achieve load-dependent occurrence of asperity contact. This leads to lubricant coverages of 66, 84, and 74 molecules per slider, respectively, explaining the noticeable difference in lubrication gap thickness between the three systems. For comparison, an atomically flat surface of the same lateral dimensions will typically hold around 130 molecules of stearic acid [23] which form a dense and almost defect-free film at that coverage. The applied loads range from 1.38 to 44 nN, corresponding to nominal pressures between 50 MPa and 1.6 GPa, which are not evenly distributed over the load spectrum. The highest density of load points can be found near the most pronounced discontinuities in the load-vs.-friction relations.

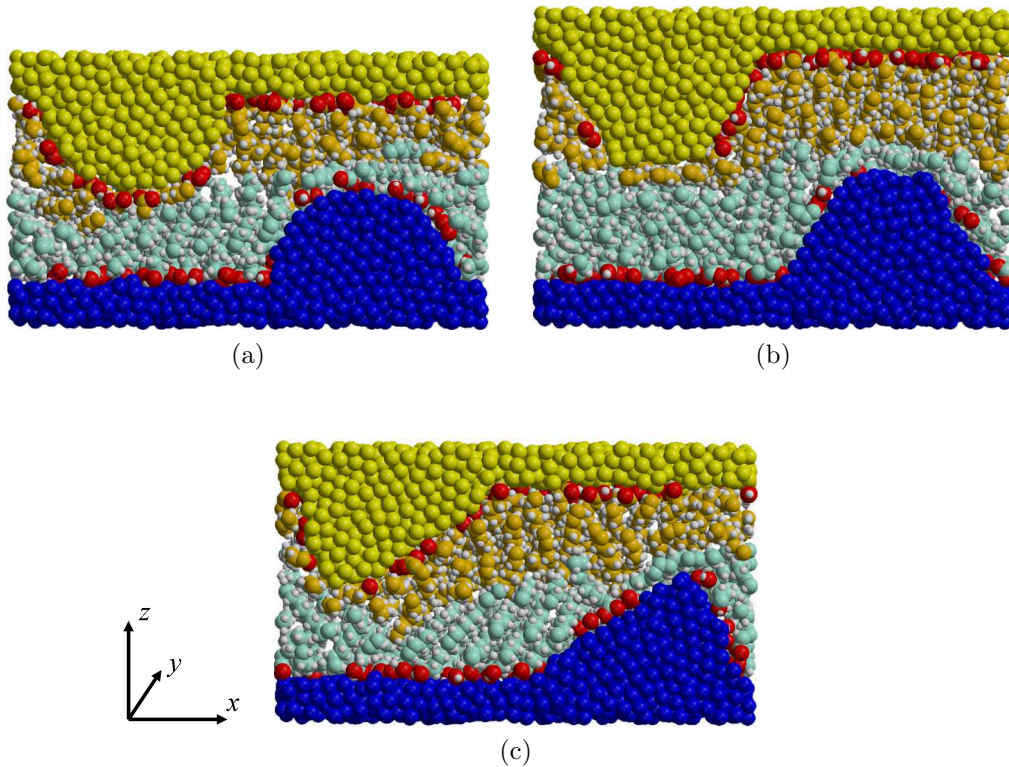


Figure 4.1: Snapshots of the three MD-nanosystems analyzed in this section. (a) semi-spherical asperity, $\eta = 66$ molecules/slider. (b) truncated cone asperity, $\eta = 84$ molecules/slider. (c) slanted pyramid asperity, $\eta = 74$ molecules/slider. The color code is the same as in Fig. 2.11.

4.1.2 Time-dependence of friction force

The friction force $F(L)$ as a function of time for the MD-nanosystem with the semi-spherical asperity shown in Fig. 4.1 (a) at five different loads can be seen in Fig. 4.2. Note how $F(L)$ remains low and relatively constant at $L = 2.76$ nN (blue). At $L = 11.02$ nN (cyan), a bulge between $t \simeq 1.0$ and 1.7 ns due to asperity contact becomes apparent. Although asperity contact increases further with growing load, the associated bulge becomes buried in the larger load-dependent contribution to the friction force at $L = 22.04$, 33.06 , and 44.08 nN (green, yellow, and red, respectively).

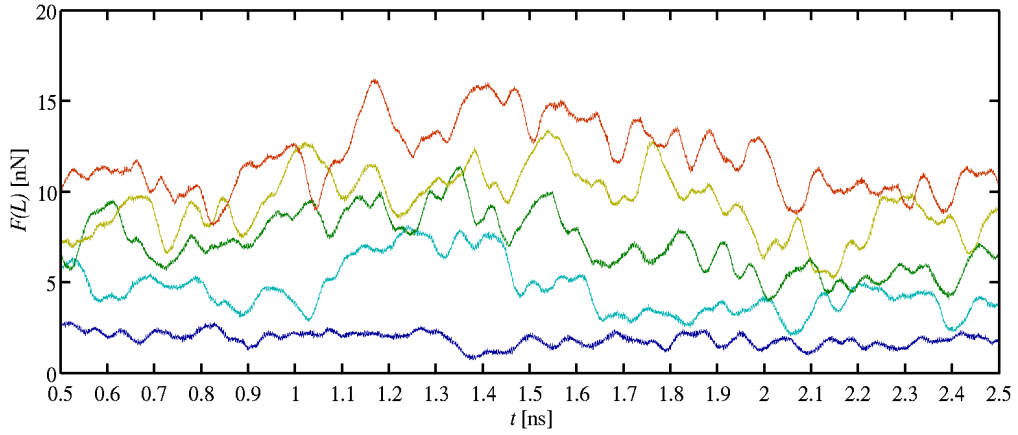


Figure 4.2: Friction force as a function of time for the system with the semi-spherical asperity at loads of 2.76, 11.02, 22.04, 33.06, and 44.08 nN. All curves are running averages with a time window of $\Delta t = 30$ ps and are colored rainbow-style with blue denoting low and red denoting high load.

4.1.3 Asperity contact area

Load-dependence As can be seen in the smooth particle method (SPM) visualization in Fig. 4.3, the larger cavities at the smallest shown load of 4.8 nN are already greatly reduced in size after 1.0 ns, but they remain present throughout the entire simulation. This small load is one of the few examples where cavities and asperity contact occur simultaneously. Necking of the solid bridge between the asperities is evident at 1.5 ns, and one can observe some plastic deformation of the asperities at 2.0 ns after contact has ended. At an intermediate load of 23.4 nN, all cavities have already vanished during the dynamic equilibration period. A larger contact area than for 4.8 nN is apparent at 1.0 and 1.5 ns. The gaps in the green bead chains representing the perimeter of the contact zone in Fig. 4.3 (e.g. at 1.0 ns), occur due to the discrete mesh and the contact zone geometry at that time, but this does not influence the accuracy of the calculated asperity contact area $A_{\text{asp}}(L)$ for any of the considered loads L . The contact duration is also longer

than for the low load, since contact has not yet ended at 2.0 ns, when a pronounced neck has formed which is about to break. At the highest shown load of 42.6 nN in Fig. 4.3, no cavities are present throughout the shear simulation, and it can be seen that some plastic deformation of the asperities has already taken place through the lubricant during the dynamic equilibration period and is evident in the image shown at 0.5 ns. One effect of the higher degree of plastic deformation at this high load is that the contact zone is less regularly shaped, especially during necking (at 1.5 and 2.0 ns). This leads to the border of the asperity contact area becoming more jagged than at lower loads, which is a consequence of how its position is calculated, see section 3.1.3. However, the error thus introduced to $A_{\text{asp}}(L)$ is negligible.

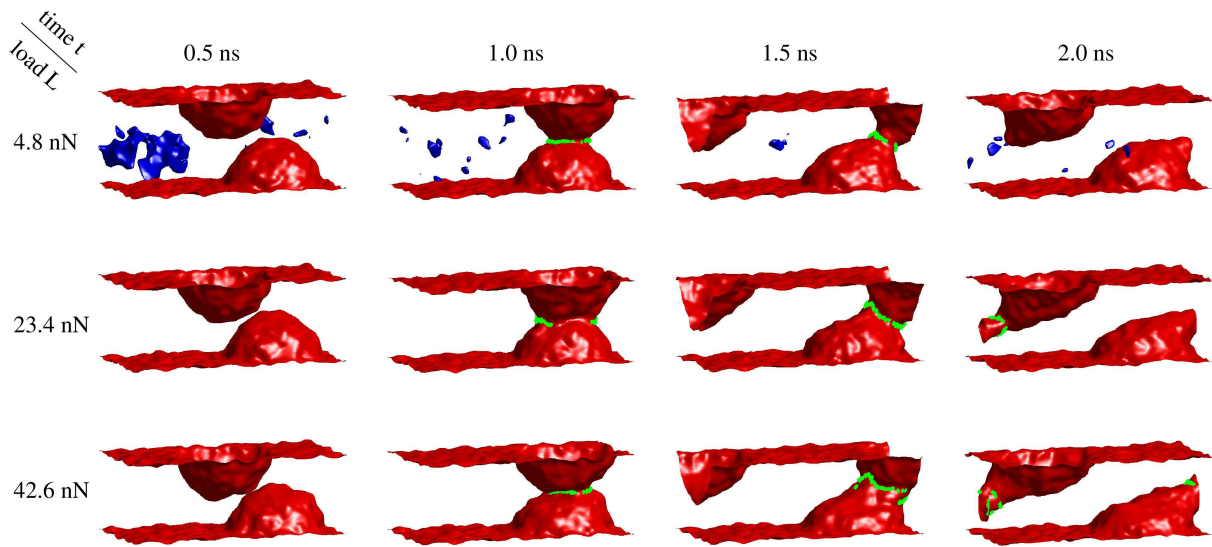


Figure 4.3: SPM representations of the nanotribological system with semi-spherical asperities at three different loads and at four different times. The lubricant is not shown for clarity. Red iso-surfaces represent the Fe-surfaces while blue iso-surfaces show the cavities within the lubricant. The green bead chains mark the points which encompass the minimum cross-section in the contact zone and thus uniquely contour the asperity contact area.

Asperity shape dependence Similar time-development is also observed for the other considered asperity geometries. To illustrate the occurring differences, however, a comparison of the different asperity shapes at the same intermediate load of 23.4 nN is made in Fig. 4.4. At 0.5 ns, the initial difference in asperity geometry is apparent. By 1.0 ns, the systems with the semi-spherical and the truncated cone asperities have already engaged in asperity contact, while the two slanted pyramid asperities have not come close enough for touching due to their shapes. However, comparing this asperity geometry at 0.5 and 1.0 ns, one can see that some deformation (blunting) of the asperity has already taken

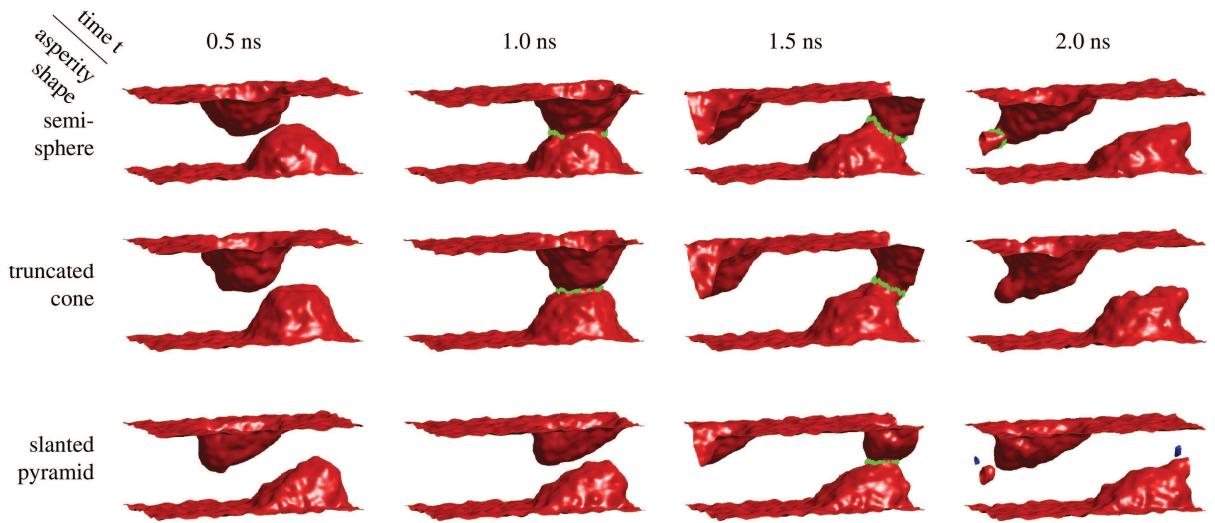


Figure 4.4: SPM representations of three nanotribological systems with semi-spherical, truncated cone and slanted pyramid asperities, respectively, at a load of 23.4 nN and at four different times. The lubricant is not shown for clarity. Red iso-surfaces represent the Fe-surfaces while blue iso-surfaces show the cavities within the lubricant. The green bead chains mark the points which encompass the minimum cross-section in the contact zone and thus uniquely contour the asperity contact area.

place before contact. At 1.5 ns, all three systems are in contact, with the semi-spherical asperity having the largest contact area and the other two being comparable in size (cf. Fig. 4.5). At 2.0 ns, contact has just ended for the truncated cone and the slanted pyramid systems, with a high degree of plastic deformation and asperity corrugation visible in the truncated cone system, while the slanted pyramid system still looks similar to the way it did before asperity contact (especially the upper asperity). This may be attributed to the short contact duration, the low number of contact atoms, as well as the original shape of the asperity which is similar to the semi-spherical one after deformation. Also note the formation of a small cavity at 2.0 ns for this asperity type.

Contact area Looking at the time-development of the asperity contact area calculated with SPM in Fig. 4.5 for $L = 23.4$ nN, all curves exhibit the same general shape. The differences are mainly in magnitude, as well as a time-offset in the beginning of contact for different asperity geometries due to their shapes. One feature common to all asperity shapes is a slightly steeper slope of the curve up to the peak, with a more moderate decline after the maximum. This can be attributed to plastic deformation and necking of the solid bridge before contact ends (cf. Fig. 4.3 at 2.0 ns; 23.4 and 42.6 nN).

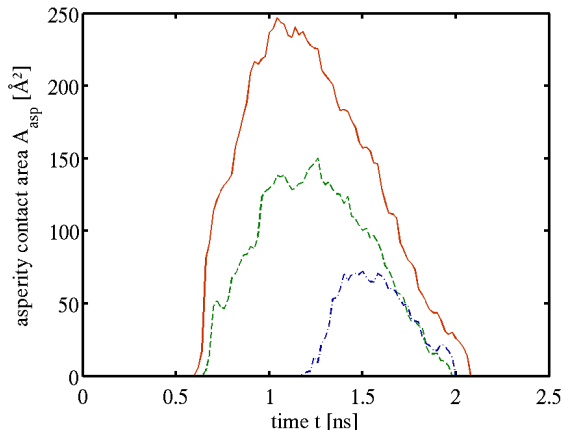


Figure 4.5: Calculated asperity contact area as a function of time at a load of 23.4 nN, corresponding with the nano-systems shown in Fig. 4.4. The solid red line stands for the system with semi-spherical asperity, while the green dashed and blue dash-dotted lines stand for the truncated cone and the slanted pyramid asperity systems, respectively.

4.1.4 Cavities

One aspect briefly mentioned in section 3.1.1, which is important for the correct estimation of $A_{\text{asp}}(L)$ is the consideration of cavities within the simulation domain, i.e., regions where the total material density drops below the threshold density ρ_0 . Gao, Luedtke and Landman noticed the emergence of a large void after near-contact of two barrier-type asperities due to turbulent flow within the lubricant of *n*-hexadecane [31], but the planned further investigation in that direction was never carried out.

Should cavities for some reason exist within the asperity contact zone, this would constitute a source of considerable error in the contact area estimation. This aspect was therefore investigated separately, and the results of the analysis can be seen in Fig. 4.6, where the total cavity volume calculated via SPM is depicted as a function of load and time in a surface plot colored according to the number of contact atoms calculated via CCP, discussed in section 3.1.4. What can be seen clearly is that in regions with high cavity volumes, asperity contact plays little or no role, and vice versa. This may be explained with the fact that as the two Fe surfaces jump to direct asperity contact, the lubrication gap thickness is suddenly reduced, effectively removing all remaining cavities. It may therefore be assumed that in our systems, cavities do not interfere with the contact area calculation.

The system with the semi-spherical asperity (Fig. 4.6a) exhibits the most well-defined behavior. Cavities exist for low loads up to approximately 10-15 nN and decrease in volume to below 0.5% of the total box volume by 2 ns if no asperity contact occurs, or almost vanish as soon as asperity contact starts. Up to loads of 10 nN, small volumes of cavities and asperity contact may co-exist. At lower loads up to 4 nN, the total cavity

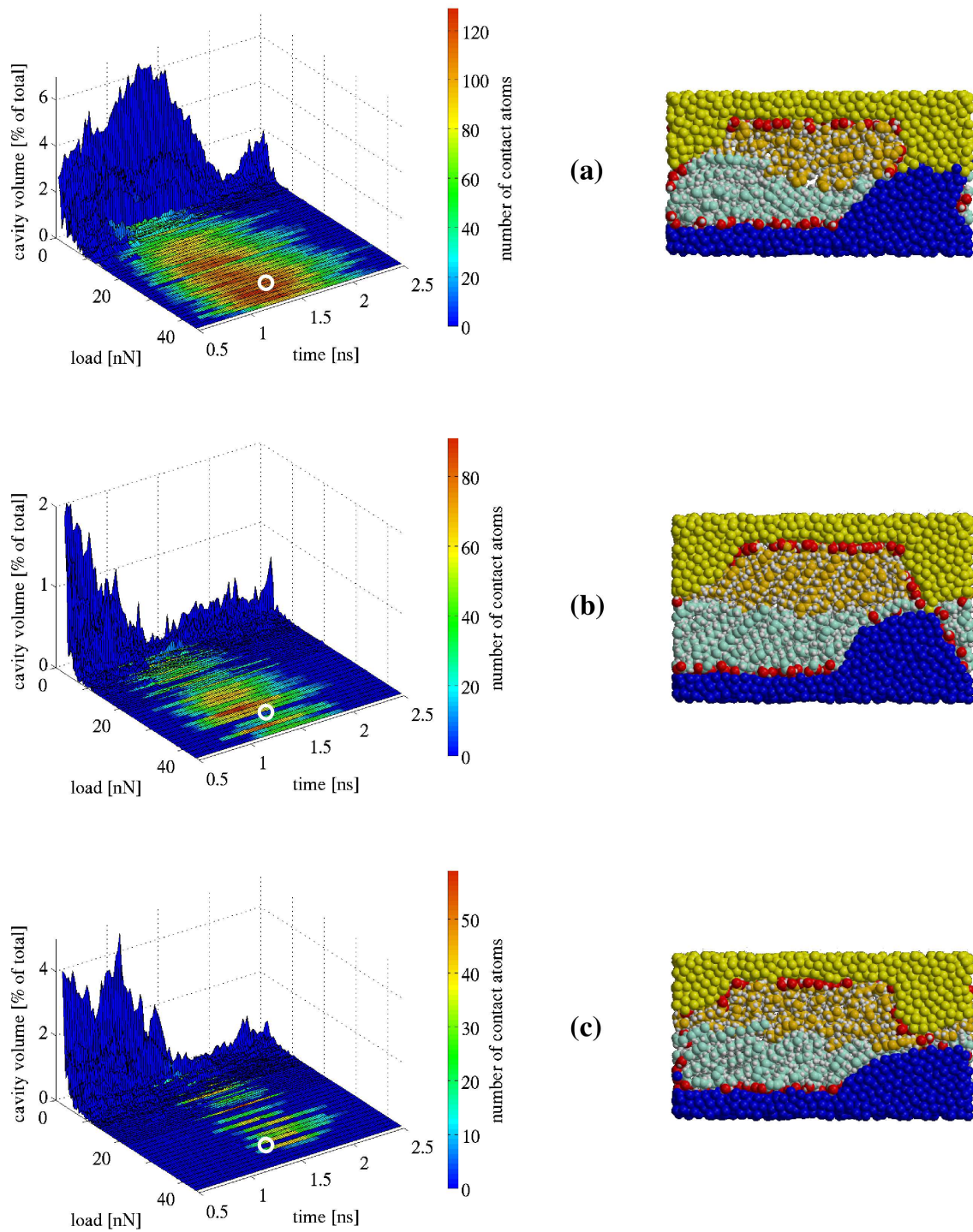


Figure 4.6: Total cavity volume of the three nanotribological systems with semi-spherical (a), truncated cone (b), and slanted pyramid (c) asperities, respectively, colored according to the number of contact atoms as a function of load and time (left column). The right column shows snapshots of an xz -section through the center of the three systems at a load of 35.7 nN and at 1.4 ns (marked with white circles in the left column). Color code as in Fig. 2.11.

volume increases again after the asperities have passed by each other without contact. Loads beyond 4 nN always exhibit asperity contact. For the other two asperity types (Figs. 4.6b and 4.6c), the picture is not as clear. Although cavities are non-significant for loads beyond about 10 nN, the contact situation is less predictable here. For the truncated cone, some medium to high loads (notably 16.5 and 35.7 nN in Fig. 4.6b) exhibit little or no asperity contact. The situation is even more chaotic for the slanted pyramid system. Here, only about half the loads higher than 20 nN exhibit asperity contact.

The points marked by white circles in the left column of Fig. 4.6 are shown as snapshots of the respective systems in the atomistic representation. They were chosen to visualize three distinct contact situations. Although these situations are exemplarily shown here for a particular asperity shape, load and time only, they can occur for several other constellations of these parameters. The snapshot in Fig. 4.6 (a) shows a full asperity contact situation where the lubricant has failed and high plastic deformation and material transfer occur. This is typical of the system with the semi-spherical asperity for loads greater than around 4 nN, where maximum contact areas range from 1.2 – 2.5 nm². Fig. 4.6 (b) shows a snapshot of a transition contact situation which is most common at low to intermediate loads for all systems, but can occur at high loads for the truncated cone and the slanted pyramid asperities. Typical contact areas for this contact situation range from 0.1 – 0.5 nm². Finally, the snapshot in Fig. 4.6 (c) represents the no-contact situation. This can be a result of low load (valid for all systems) or, as in this example, due to plastic deformation of the asperities during their approach.

4.1.5 Three-term kinetic friction law

The left column in Fig. 4.7 shows the load-vs.-friction behavior of the three simulated systems, for which L and F were obtained by time-averaging their values over 2.0 ns after the dynamic equilibration period. For an example of the time development of the friction force recall Fig. 4.2. Between 53 and 63 data points were obtained in this way for each system, yielding a highly resolved load dependence curve for each case, which clearly reveals non-linearities and discontinuities. The parameters F_0 , τ and μ entering the three-term kinetic friction law $F(L) = F_0 + \tau A_{\text{asp}}(L) + \mu L$, obtained by minimising χ^2 , as well as their estimated errors are summarized in Table 4.1, where Q denotes the goodness of fit from Eq. (3.21). The standard deviations of the calculated friction force values, which are necessary to fit the parameters and are shown as error bars in Fig. 4.7, correspond to $\sigma_{\text{si},x}$ and are calculated according to Eq. (3.14) based on the statistical inefficiency. They include the factor 2 discussed in section 3.3.2 and amount to errors of 5–10%.

It is worth pointing out again that the values for $A_{\text{asp}}(L)$ are obtained from geometrical considerations only and are calculated completely independently of the friction force data. With that in mind, the high degree of agreement between the original data and the points fitted to the proposed friction law, which can be seen in the right column of Fig. 4.7, is impressive. The accuracy of the proposed smooth particle approach also con-

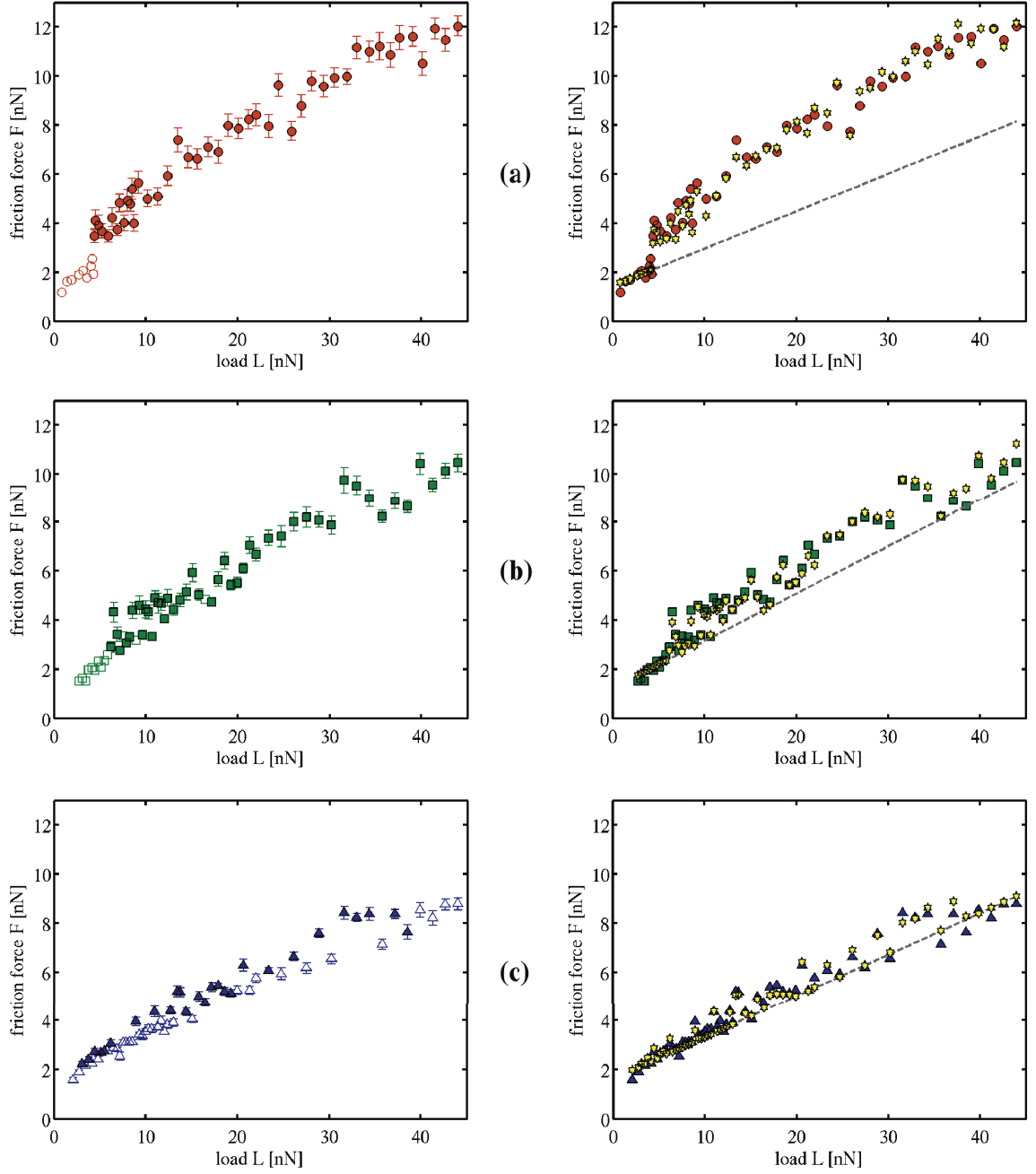


Figure 4.7: Load-vs.-friction behavior of the three nanotribological systems with semi-spherical (a), truncated cone (b), and slanted pyramid (c) asperities, respectively. The error bars in the left column are based on the statistical inefficiency of the MD force values. Empty symbols represent simulations in which no asperity contact occurred, while filled symbols denote simulation runs with asperity contact. In the right column, the original data is superimposed with yellow stars showing the values obtained from the three-term friction law in Eq. (3.15) using the χ^2 -fitted parameters from Table 4.1, while the dashed lines represent the Derjaguin-form, i.e., $F(L) = F_0 + \mu L$.

asperity geometry	F_0 [nN]	ΔF_0 [nN]	μ	$\Delta\mu$	τ [nN/Å ²]	$\Delta\tau$ [nN/Å ²]	Q
semi-sphere	1.437	0.072	0.153	0.017	0.034	0.004	0.992
truncated cone	1.222	0.057	0.193	0.007	0.030	0.004	0.932
slanted pyramid	1.611	0.053	0.170	0.004	0.042	0.005	0.997

Table 4.1: Best-fit parameters and their respective estimated errors obtained from the χ^2 -fitting procedure applied to Eq. (3.15). Q is the goodness-of-fit parameter from Eq. (3.21).

firmly its possible applicability at nanoscale to estimate typical quantities from continuum mechanics, when a simple downscaling fails as it has been already shown in Ref. [133] for the asperity contact area.

The dashed lines in Fig. 4.7 represent the contributions to the friction force which do not depend on asperity contact. The best way to discuss this is using the examples of the semi-spherical asperity, which exhibits a high degree of asperity interaction, and the slanted pyramid asperity, which is mainly load-controlled. In the first case, the dashed line passes right through the data points as long as there is no asperity contact, while the contributions of the load-controlled and the adhesion-controlled term are of similar magnitude for higher loads where asperity contact occurs. In the case of the slanted pyramid asperity, the left panel in Fig. 4.7 (c) shows that asperity contact occurs in only about 50% of the simulations, even for high loads. This is reflected in the right panel, as the dashed line remains close to the original data throughout the entire load range, which means that except for some deviations between 20 and 35 nN, there is almost no contribution from the adhesion-controlled term.

The predominantly load-controlled behavior of the slanted pyramid system may also affect the quality of the fitted value of τ , which at ~ 4 GPa is noticeably higher than for the other systems, leading to a spread of 17.3% for the values of τ between asperities. It is worth pointing out that τ represents the effective shear strength of the entire nanotribological system and should therefore not be confused with the shear strength of bulk Fe. The corresponding mean variation of μ is 11.7% and therefore lies within experimental tolerances. The values for F_0 in table 4.1 vary by 13.7% from one asperity to the next, which may be a result of the slightly different lubricant coverages for different asperity shapes and/or slightly different nominal asperity overlaps. F_0 may be seen as the extrapolation of the data to zero load, which is reasonable because $A_{\text{asp}}(L)$ can be considered zero at small loads. The actual simulation of loads below the ones considered in this work is very demanding since on one hand the large cavities in the initial configurations have to be dealt with properly, and on the other hand the combination of large asperities and

a relatively high shear velocity leads to uncontrolled separation of the two sliders at very low loads.

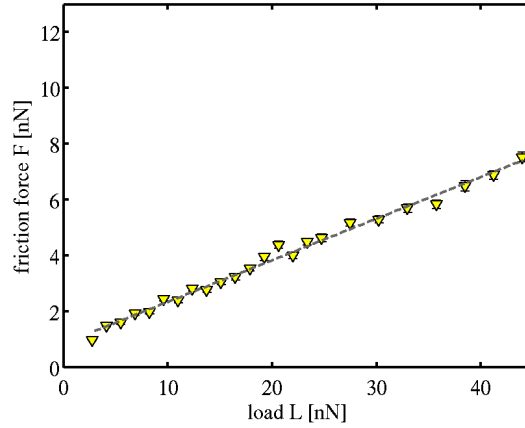


Figure 4.8: Load-vs.-friction behavior of the nanotribological systems without any asperities, the lubricant coverage nominally corresponding to the one with semi-spherical asperities. The dashed line is a linear fit to the data.

To compare the obtained results with a system that does not have any asperities, 24 load points were calculated for such a system with $\eta = 96$ molecules per surface. The higher lubricant coverage compared to the other systems serves to fill the void left by the removed asperities. Fig. 4.8 shows its load-vs.-friction behavior, which is very linear, since with $A_{\text{asp}}(L) = 0$ there is no contribution from the adhesion-controlled term. The linear regression yields $\mu = 0.15$, $F_0 = 0.84$ and a correlation coefficient of 0.996, which compares well with the other values obtained for the nanoscopic coefficient of friction, μ (cf. Table 4.1). The difference in F_0 of a factor of about 2 is believed to originate on one hand from the higher degree of order in the monolayers of the lubricant molecules, which are undisturbed by asperities in this system, and on the other hand by the greater effective distance between the solid surfaces.

We can conclude that the SPM approach for mapping MD data to continuum proposed in section 3.1 has been successfully applied to visualize the Fe surface geometry of the simulated nanosystems with load-dependent occurrence of asperity-asperity contact. Furthermore, the method allows the straightforward calculation of the contact area, which enters the three-term friction law introduced in section 3.4.1 and can be used to explain the non-linearities in the load-vs.-friction behavior of the systems. Finally, Ref. [134] can be seen as an experimental proof that a formally equivalent friction law also holds true for fluid-fluid interfaces.

4.2 Simulation of Nanoscopic Run-in

While the simulations in section 4.1 focus on many short runs to achieve high load resolution, here some of this resolution was sacrificed to the possibility of simulating much longer time periods [40]. This allows the repeated occurrence of asperity-asperity contact which may be interpreted as the simulation of a nanoscopic run-in procedure. In this section I will compare two asperity types, one semi-sphere and one slanted pyramid, at 16 equally spaced loads with 10 repeated sliding passes (chances for asperity-asperity contact) each.

4.2.1 Specific system setup

The two nanotribological systems featured in this section are prepared following the general guidelines for large substrates in chapter 2. The thickness of the amorphous Fe substrates is 1.96 nm, which is equivalent to 4050 atoms or ~ 12 monolayers of bcc Fe(100). Both simulated asperity types (semi-spherical and slanted pyramid) have a uniform lubricant coverage of $\eta = 66$ stearic acid molecules per slider. Snapshots of the systems can be seen in Fig. 4.9. The 16 applied loads L range from 2.75 to 44 nN in steps of 2.75 nN, corresponding to nominal pressures between 100 MPa and 1.6 GPa in steps of 100 MPa.

4.2.2 Asperity contact area

At the beginning of the simulation, the lubricant molecules are uniformly distributed over the entire substrate surface. As the two asperities approach each other during shear, the lubricant undergoes some initial restructuring, and if the local forces in the lubrication gap (which depend on load, shear velocity, asperity geometry, etc.) become sufficiently high, lubricant molecules situated on the asperities may be squeezed out and solid-solid contact occurs. Figs. 4.10 and 4.11 show overviews of the time development of the slider surface geometries for both asperity types at a load of 24.8 nN in SPM-representation, as discussed in section 3.1.

The momentary asperity contact area $A_{\text{asp}}(L, t)$ is calculated using the SPM post-processing scheme described in section 3.1.3. When superimposing these data for all calculated passes p , it is evident that the time of the onset of contact $t_{\text{cont}}^{(p)}$ increases appreciably after the first pass, see Fig. 4.12. At loads where asperity contact occurs in almost every pass, $t_{\text{cont}}^{(p>1)}$ fluctuates about a mean value greater than $t_{\text{cont}}^{(1)}$, whereas for loads where $A_{\text{asp}}(L, t)$ vanishes after several passes, $t_{\text{cont}}^{(p)} < t_{\text{cont}}^{(p+1)}$ usually holds true.

As a general trend, it can be seen that the time-averaged contact area for a single pass

$$A_{\text{asp}}(L) = \langle A_{\text{asp}}(L, t) \rangle, \quad \forall t \in [t_0^{(p)}, t_0^{(p)} + T], \quad (4.1)$$

where $t_0^{(p)}$ is the starting moment of p th pass of period T ($p = 1, 2, \dots, 10$), decreases with every pass irrespective of load, see Fig. 4.13 (a). The types of asperity contact

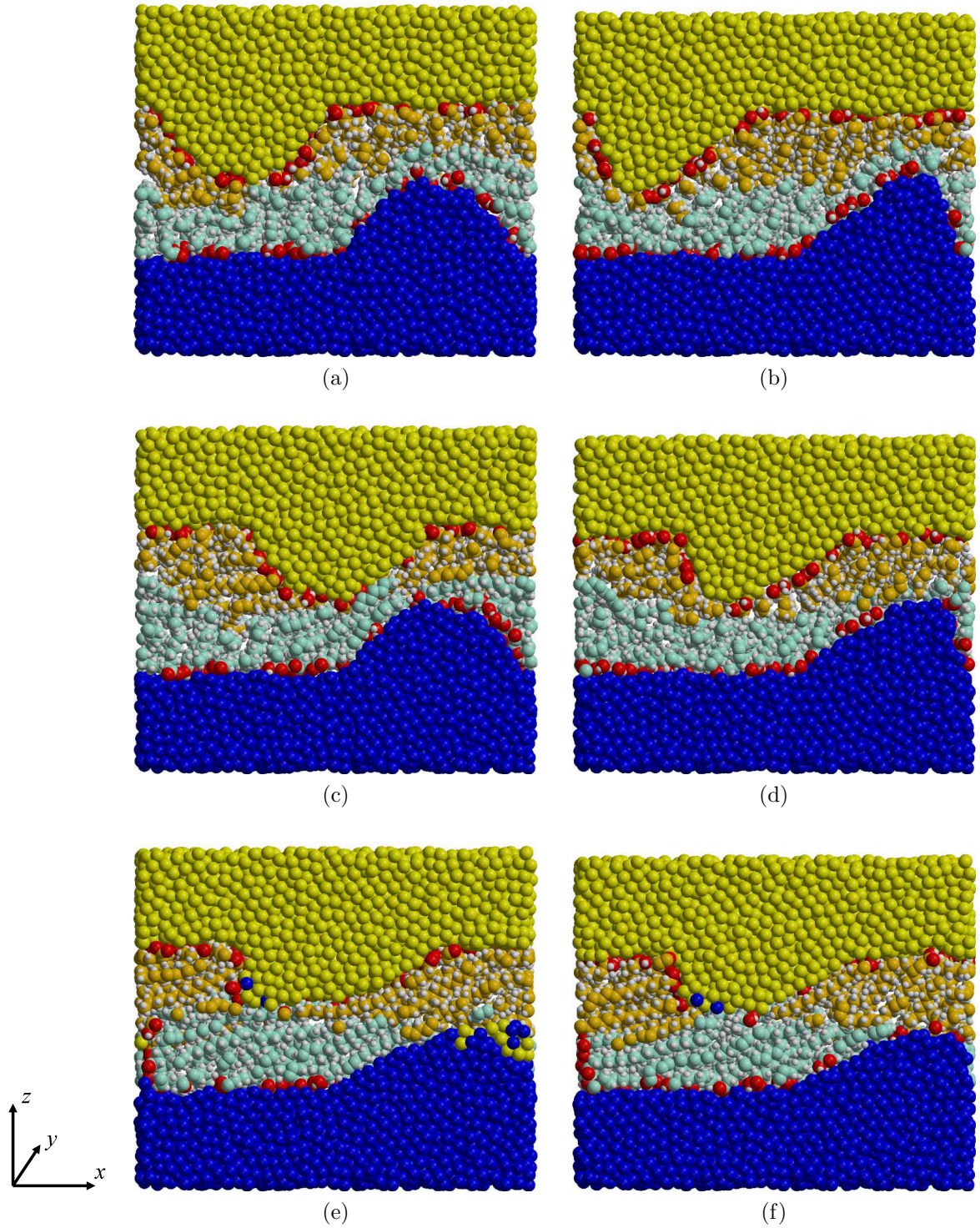


Figure 4.9: Side views of the semi-spherical (left) and the slanted pyramid (right) systems at at a load of $L = 24.8$ nN . (a, b) Initial configurations at $t = 0$ ns. (c, d) Beginning of first pass at $t = 0.5$ ns. (e, f) End of 10th pass at $t = 19.1$ ns. The color code is the same as in Fig. 2.11.

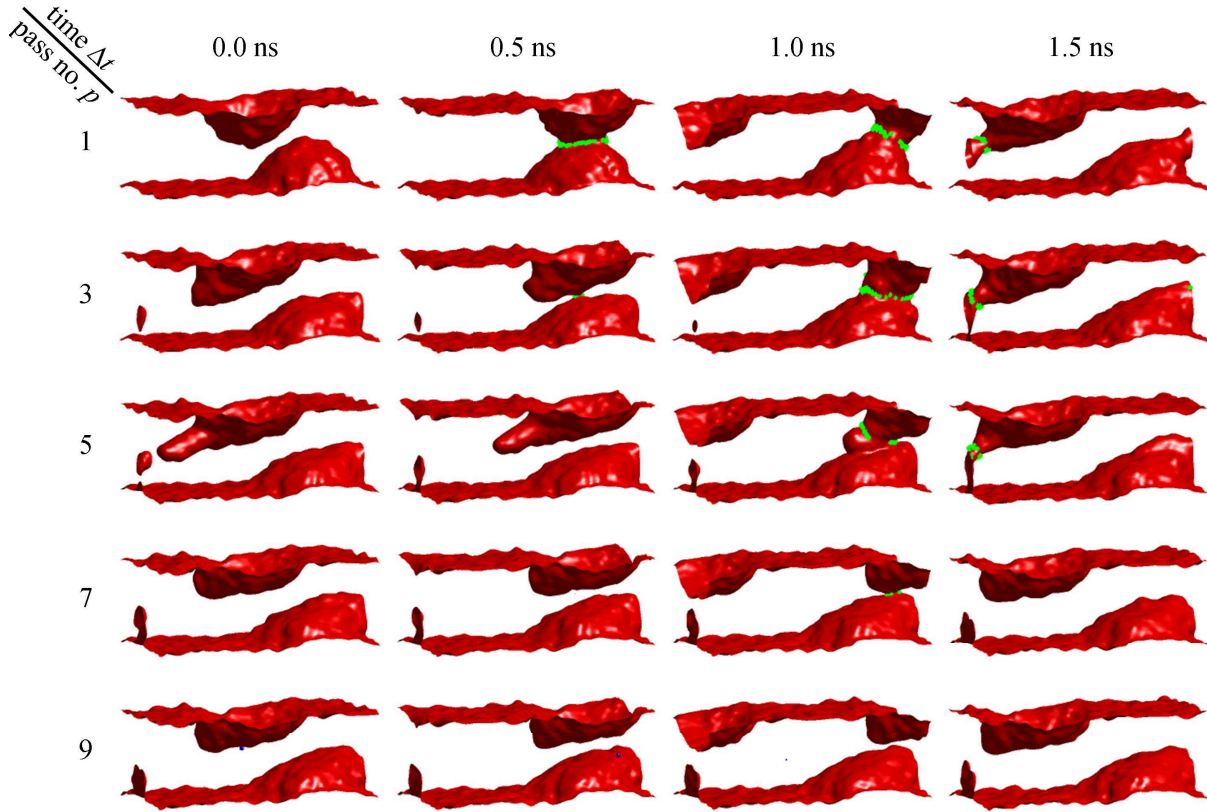


Figure 4.10: Snapshots of an SPM-representation of the semi-spherical asperity system at $L = 24.8$ nN for sliding passes 1, 3, 5, 7, and 9, and at four equally spaced times during each pass. The lubricant molecules are not shown for clarity. The green bead chains mark the boundary of the contact zone calculated with SPM. The top left image shows the initial configuration after the equilibration period, and the bottom right one shows a configuration near the end of the simulation.

development can be classified as follows: (1) $A_{\text{asp}}(L) \approx 0$ for all L , (2) $A_{\text{asp}}(L)$ decreases monotonously with p , (3) $A_{\text{asp}}(L)$ decreases with p , but has a plateau for several passes, and (4) $A_{\text{asp}}(L)$ has a local maximum at $p > 1$. With the exception of the sporadic cases of the 3rd and the 4th type, asperity contact has virtually vanished after 5-6 passes.

This quite clear-cut behavior of $A_{\text{asp}}(L)$ does not apply to the contact duration Δt_{cont} , see Fig. 4.13 (b). Δt_{cont} and $A_{\text{asp}}(L)$ have an approximately parabolic relationship, recall Fig. 3.7 (a), meaning that even very small asperity surface areas can be in contact for considerable periods. Therefore, even after 7 passes, one may encounter values for Δt_{cont} which have only decreased to 30% of their initial or maximum values.

The top panels of Figs. 4.14 and 4.15 shows complete maps of the asperity contact area $A_{\text{asp}}(L)$ as a function of time and load for the semi-spherical and the truncated cone asperity, respectively. The former illustrates how even at medium to high loads, asperity contact may subside after the first pass (e.g. 27.6 and 35.8 nN), whereas even for low

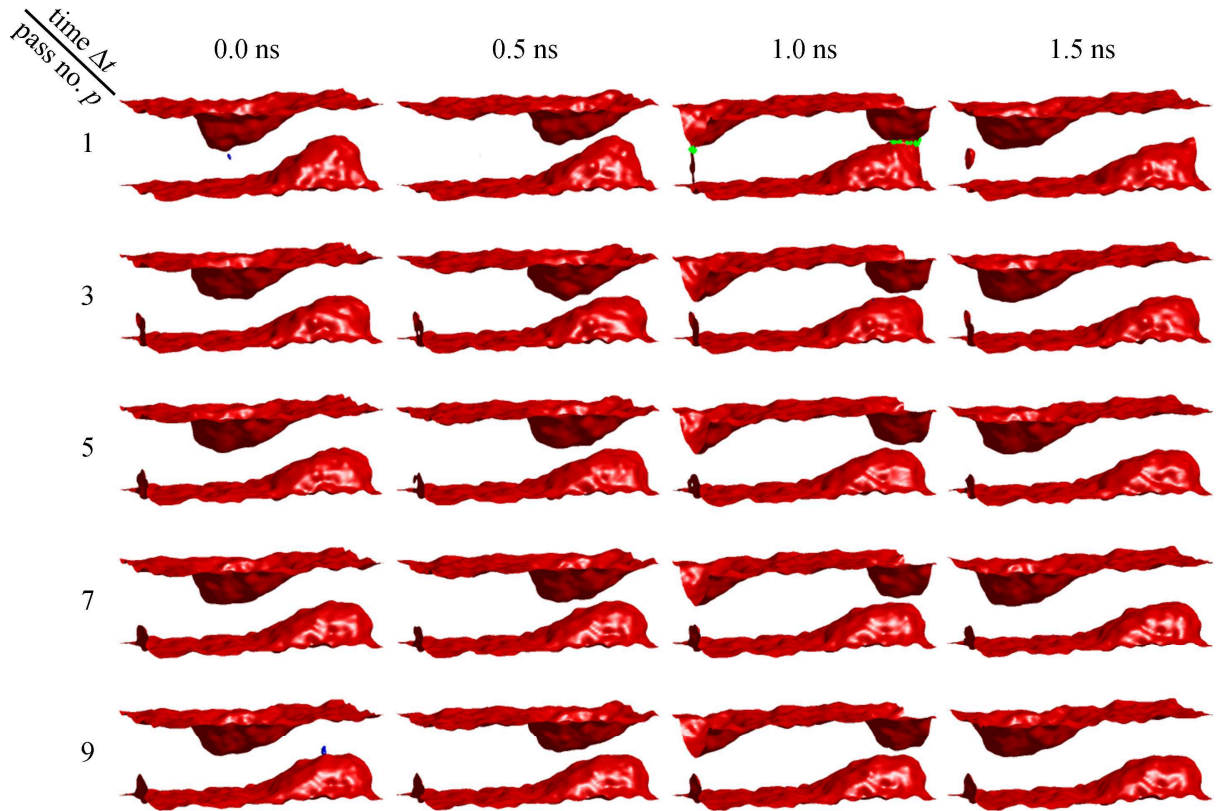


Figure 4.11: Snapshots of an SPM-representation of the slanted pyramid asperity system at $L = 24.8$ nN for sliding passes 1, 3, 5, 7, and 9, and at four equally spaced times during each pass. The lubricant molecules are not shown for clarity. The green bead chains mark the boundary of the contact zone calculated with SPM. The top left image shows the initial configuration after the equilibration period, and the bottom right one shows a configuration near the end of the simulation.

loads, recurring asperity contact is possible (e.g. 13.8 nN). In the second map it can be seen that for the slanted pyramid asperity there exist high loads (> 38 nN) where, due to prior asperity deformation, no (or only negligible) asperity contact occurs, see section 4.2.3. Note that at the lowest load of 2.76 nN, asperity contact occurs only during the passes 4, 5, and 6, which is a rare example of asperity contact development of type 4 in the classification above.

4.2.3 Asperity deformation

One quantity which may be readily calculated using smooth particle post-processing, namely by integrating over the areas of the triangles which constitute the iso-surfaces shown in Figs. 4.10 and 4.11, is the total Fe surface area $A_{\text{Fe}}(L, t)$. Maps of the time and load dependence of $A_{\text{Fe}}(L, t)$ for both asperity types can be found in Figs. 4.14 and 4.15.

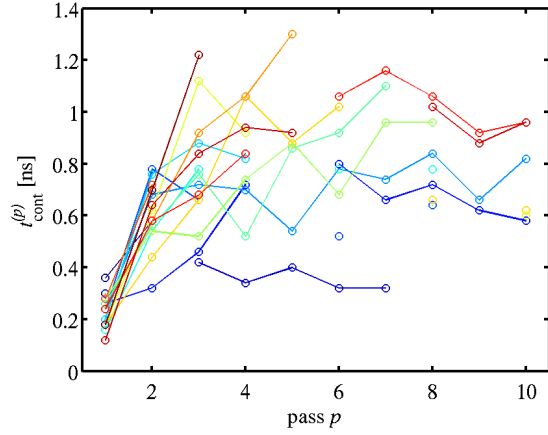


Figure 4.12: The moment of asperity contact onset $t_{\text{cont}}^{(p)}$ as a function of the pass number p for the semi-spherical asperity. Time is counted starting after the dynamic equilibration period of 0.5 ns and restarts with every pass. Colors are rainbow-style with blue denoting low and red denoting high loads.

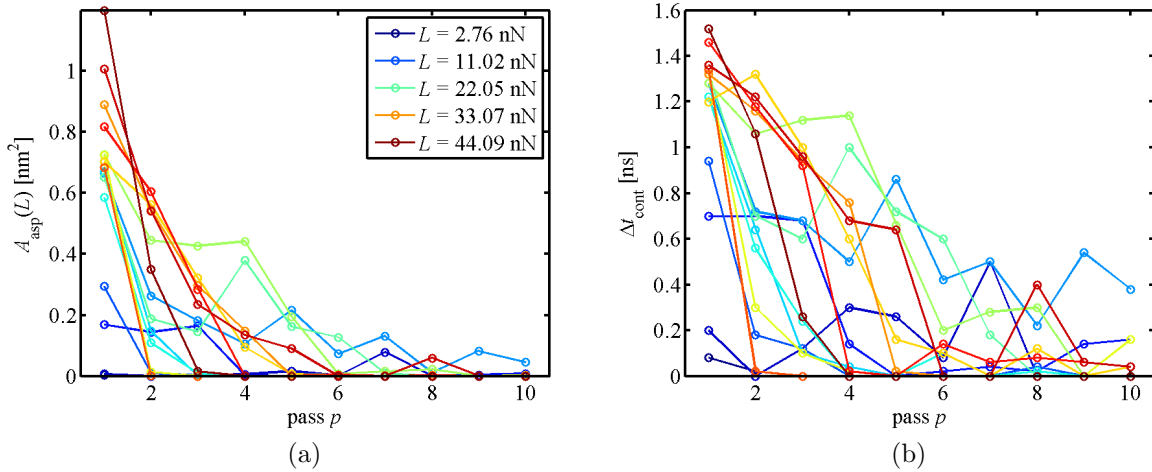


Figure 4.13: Average asperity contact area (a) and contact duration (b) as a function of the pass number p and the load for the semi-spherical asperity system. Colors are rainbow-style with blue denoting low and red denoting high loads.

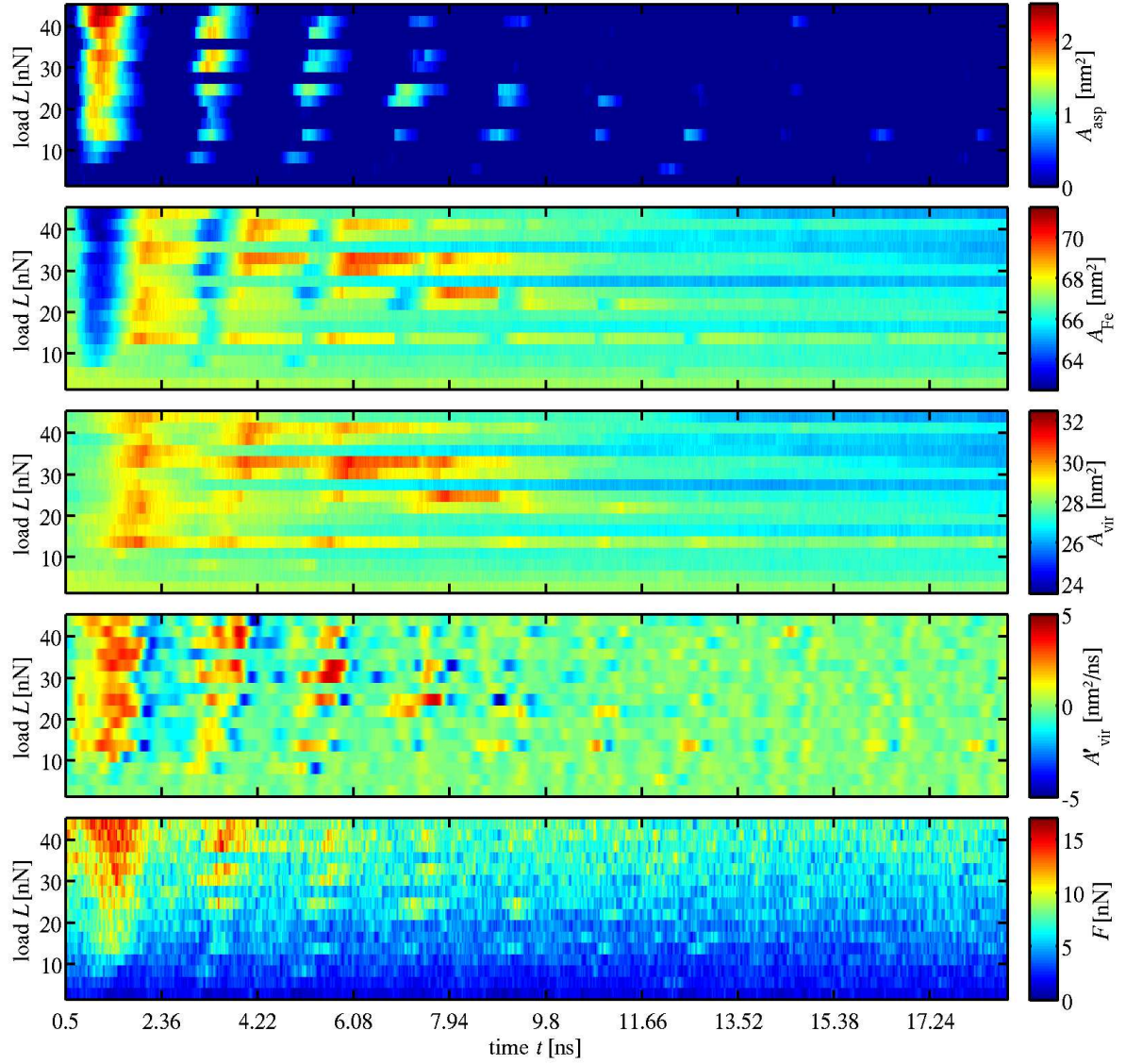


Figure 4.14: Maps of the asperity contact area $A_{\text{asp}}(L, t)$, the total Fe surface area $A_{\text{Fe}}(L, t)$, the “virtual asperity surface area” $A_{\text{vir}}(L, t)$, its time-derivative $A'_{\text{vir}}(L, t)$, and the friction force $F(L, t)$ as a function of time and load for the semi-spherical asperity. The tick marks along the time axis denote the beginning of a new pass. The dynamic equilibration period of 0.5 ns is not shown.

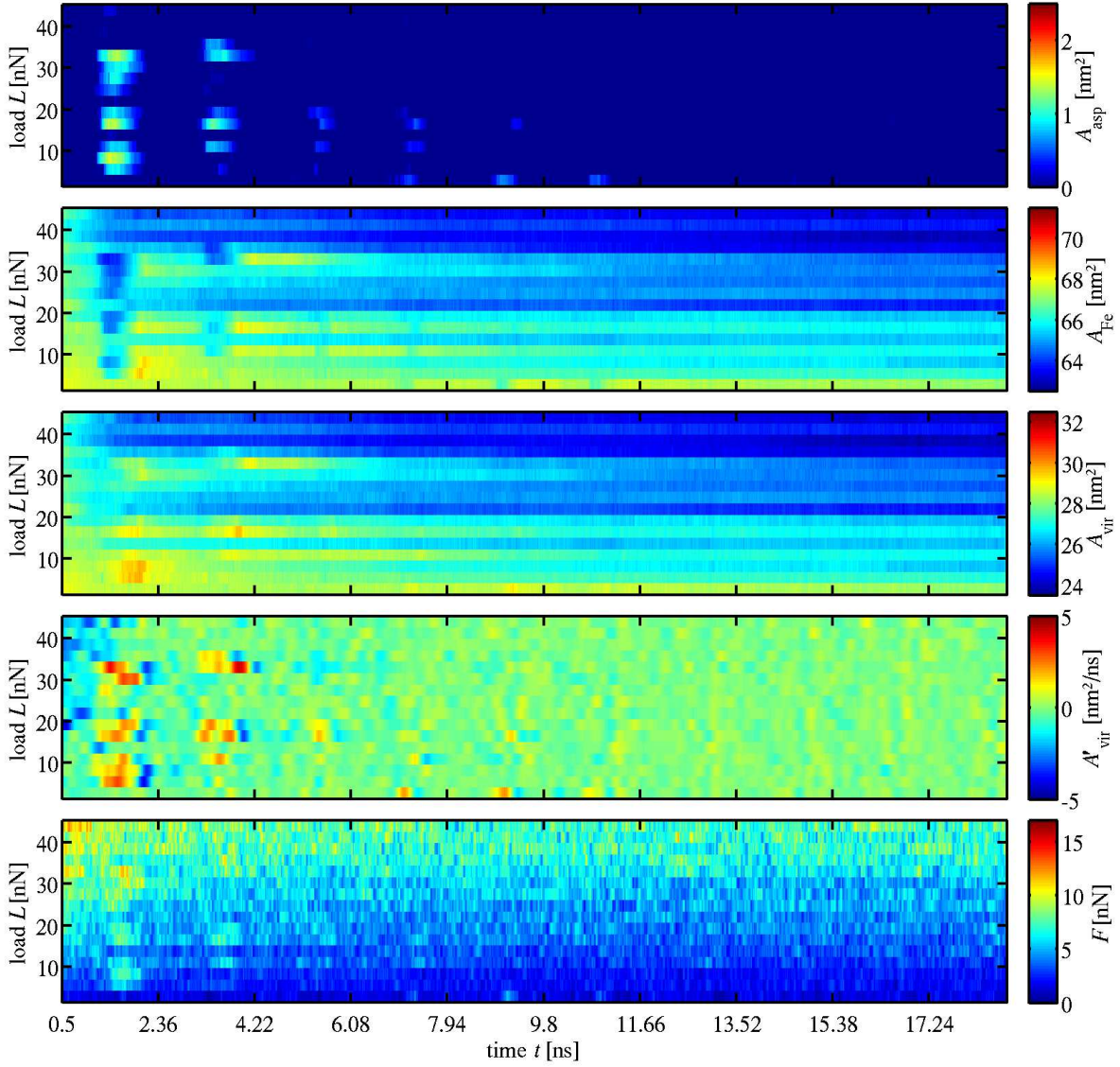


Figure 4.15: Maps of the asperity contact area $A_{\text{asp}}(L, t)$, the total Fe surface area $A_{\text{Fe}}(L, t)$, the “virtual asperity surface area” $A_{\text{vir}}(L, t)$, its time-derivative $A'_{\text{vir}}(L, t)$, and the friction force $F(L, t)$ as a function of time and load for the slanted pyramid asperity. The tick marks along the time axis denote the beginning of a new pass. The dynamic equilibration period of 0.5 ns is not shown.

During asperity contact, one can see the sudden decrease of $A_{\text{Fe}}(L, t)$ due to the loss of $2A_{\text{asp}}(L, t)$, cf. also Fig. 4.16 (a) and (b). This is due to the fact that free surface is lost at the expense of contact area. One may therefore be tempted to calculate $A_{\text{asp}}(L, t)$ from $A_{\text{Fe}}(L, t)$ directly, saving considerable computational effort, but this would only be possible with low accuracy as long as $A_{\text{Fe}}(L, t)$ remains otherwise constant for the entire duration of contact, which is not the case if plastic deformation occurs.

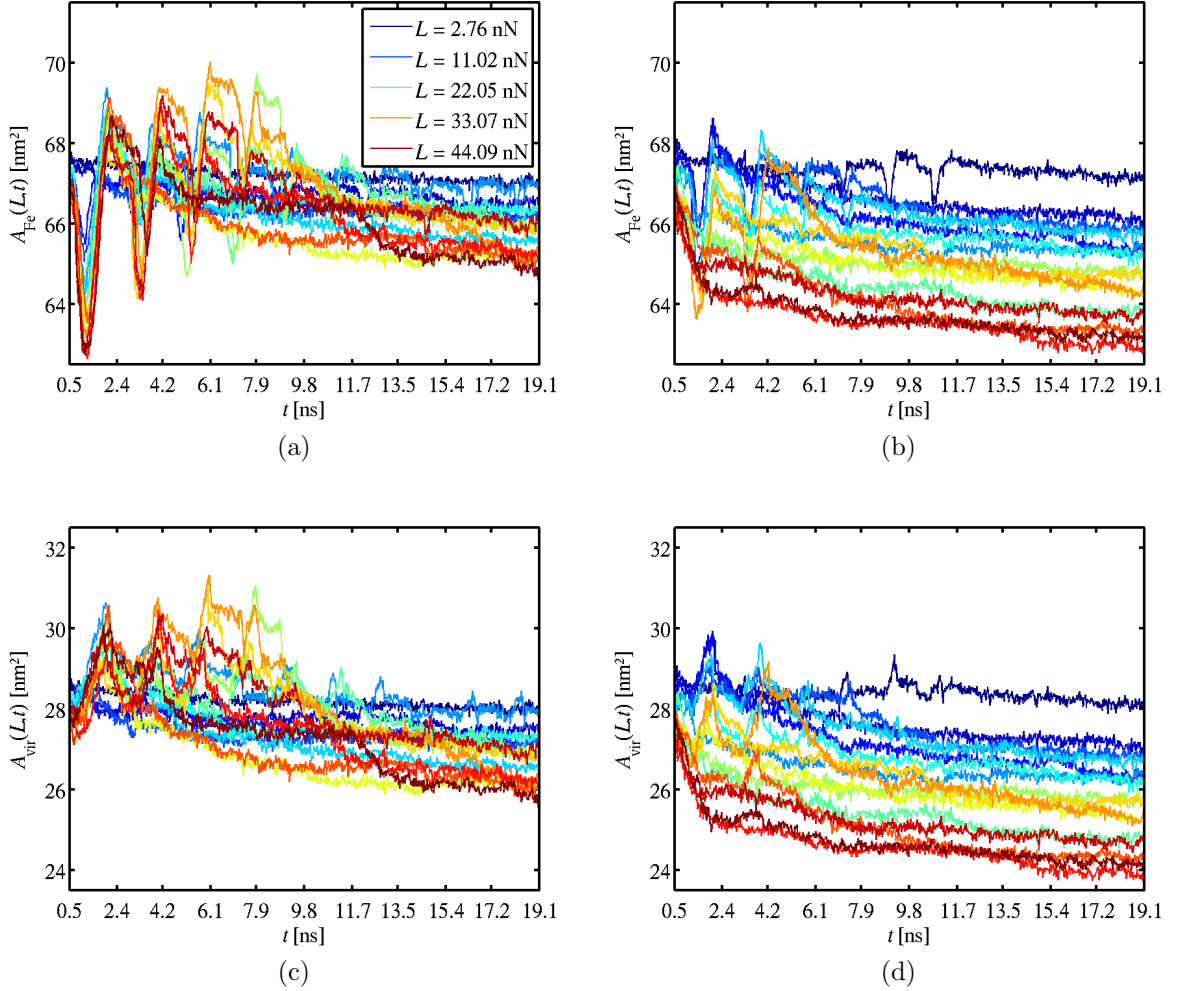


Figure 4.16: The total Fe surface area $A_{\text{Fe}}(L, t)$ of the system with the semi-spherical (a) and the slanted pyramid (b) asperity at all considered loads, compared to the “virtual asperity surface area” $A_{\text{vir}}(L, t)$ for the same systems shown in (c) and (d). The color mapping is in rainbow style, with low loads represented in blue and high loads in red. Tick marks along the t -axis denote the beginning of a new pass.

However, this also means that by using a reverse approach, through the knowledge of $A_{\text{Fe}}(L, t)$ and $A_{\text{asp}}(L, t)$, one may estimate the amount and rate of plastic deformation of

the asperities. So by adding $2A_{\text{asp}}(L, t)$ to $A_{\text{Fe}}(L, t)$ and subtracting an estimate for the (approximately constant) non-asperity Fe surface area ($2 \times xy$ -cross-section - $2 \times$ asperity base), one obtains the “virtual asperity surface area” $A_{\text{vir}}(L, t)$, cf. the maps in Figs. 4.14 and 4.15 as well as Fig. 4.16 (c) and (d). Assuming only very little compressibility of the iron and therefore nearly constant iron volume, $A_{\text{vir}}(L, t)$ is a reasonable measure for the surface-to-volume ratio and hence the shape of the asperities. This holds true if the non-asperity Fe surface of the system does not appreciably change its shape throughout the simulation. Note that the initial value of $A_{\text{vir}}(L, t = 0) \approx 28 \text{ nm}^2$ corresponds to the surface of two semi-spheres of radius 1.5 nm.

By numerically calculating the time-derivative of $A_{\text{vir}}(L, t)$,

$$A'_{\text{vir}}(L, t) = \frac{\partial A_{\text{vir}}(L, t)}{\partial t}, \quad (4.2)$$

one can now identify the times when the shape of the asperities changes the most, which may be interpreted as a geometrical indicator for asperity deformation.

Fig. 4.17 shows a side-by-side comparison of the time development of $A_{\text{asp}}(L, t)$, $A_{\text{vir}}(L, t)$, $A'_{\text{vir}}(L, t)$ and $F(L, t)$ for both systems with different asperity geometries at $L = 24.8 \text{ nN}$. For clarity, $A'_{\text{vir}}(L, t)$ was filtered using a cubic B-spline kernel 600 ps wide, and $F(L, t)$ was block-averaged with a block size of 20 ps. In general, $A_{\text{vir}}(L, t)$ tends to decrease over time, which reflects the relaxation of the surface in order to minimize the surface-to-volume ratio. The decrease of $A_{\text{vir}}(L, t)$ is in the range of 0–7% and is greatest if there is little or no asperity contact. At high loads, deformation of both asperities may take place before contact would have occurred for the first time, sometimes preventing contact altogether. This can be seen clearly in the behavior of $A_{\text{asp}}(L, t)$ and $A'_{\text{vir}}(L, t)$ for the slanted pyramid asperity at several loads greater than 12 nN. For example, looking at the top-left corner of the map of $A'_{\text{vir}}(L, t)$ in Fig. 4.15, blue regions indicate a considerable initial decrease of the slanted pyramid asperity surface, while a comparison with the respective part in the map of $A_{\text{asp}}(L, t)$ shows that little to no asperity contact occurs during the first pass.

This surface relaxation is interrupted by local increases and sharp decreases of $A_{\text{vir}}(L, t)$ due to asperity contact. As can be expected, the local, usually linear increases coincide with the times of asperity contact, where the solid bridge is drawn out into a “wire”, thus increasing the surface area. As soon as contact ends and the wire breaks, $A_{\text{vir}}(L, t)$ decreases, usually sharply at first as the two loose ends of the broken wire quickly retract, then more moderately as the shapes of the asperities relax.

In rare cases it can occur that $A_{\text{vir}}(L, t)$ decreases sharply not at the end but at the onset of asperity contact (e.g. semi-spherical, $L = 24.8 \text{ nN}$, $p = 5$, cf. Fig. 4.10, center, and Fig. 4.17). Here, an unrelaxed dangling wire end snaps onto the opposing asperity, thus reducing the surface area very quickly.

Asperity contacts with maximum areas greater than 0.5 nm^2 are usually reflected as increases in the friction force $F(L, t)$, see the bottom maps in Figs. 4.14 and 4.15 for an overview and Fig. 4.17 for a particular example at $L = 24.8 \text{ nN}$. This applies to low and

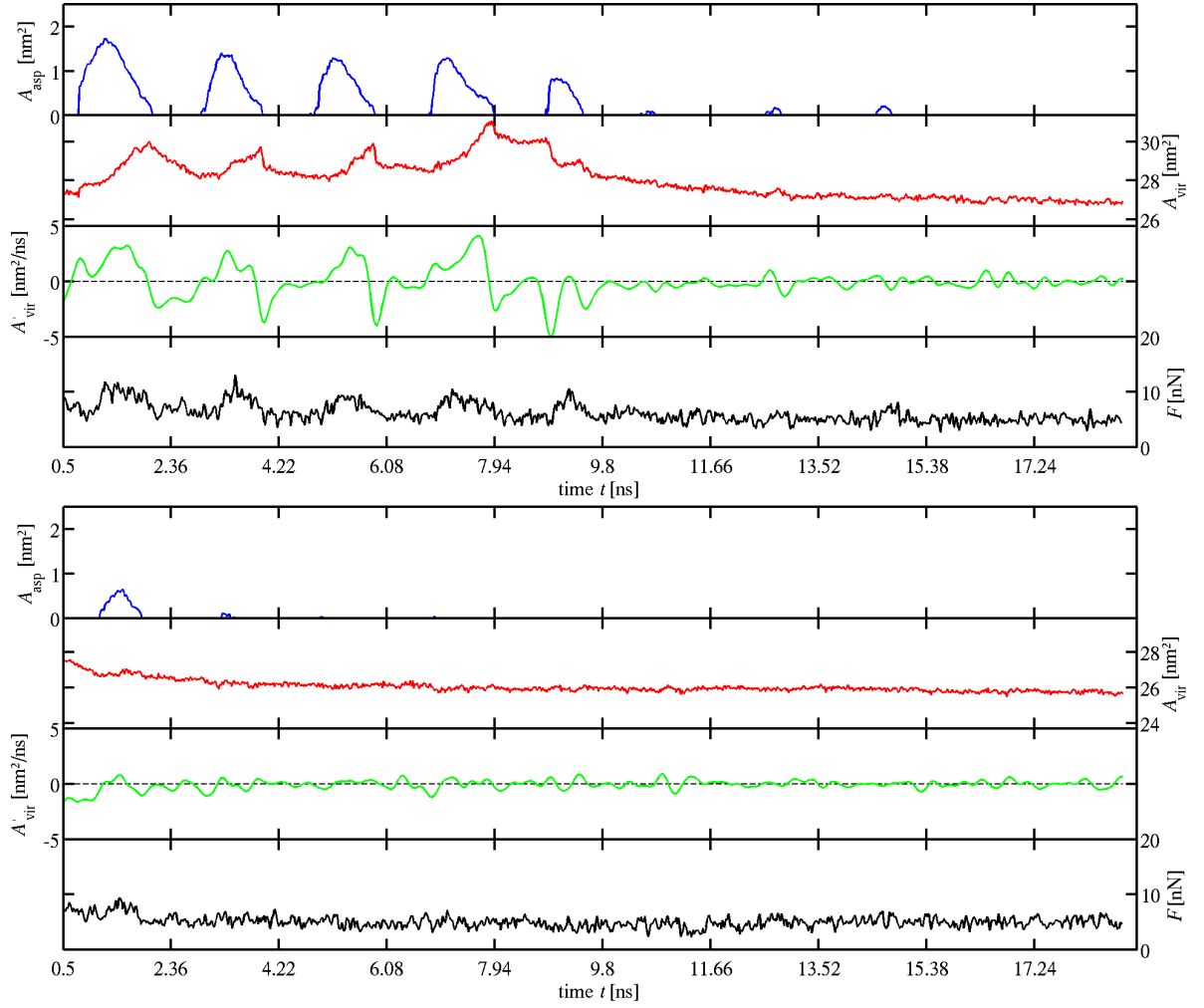


Figure 4.17: Time development of the asperity contact area $A_{\text{asp}}(L, t)$, the “virtual asperity surface area” $A_{\text{vir}}(L, t)$, its filtered time-derivative $A'_{\text{vir}}(L, t)$, and the block-averaged friction force $F(L, t)$ for the semi-spherical (top) and the slanted pyramid asperity (bottom) at $L = 24.8$ nN. Tick marks along the t -axis denote the beginning of a new pass. The dynamic equilibration period of 0.5 ns is not shown.

medium loads (up to 30 nN) in particular. At high loads, smaller increases are usually buried in the noisy $F(L, t)$ -signal.

Figs. 4.14 and 4.15 show complete maps of the asperity deformation rate $A'_{\text{vir}}(L, t)$ as a function of time and load for both asperity types. Yellow, orange and red areas denote loads and times where the surface-to-volume ratio of the asperities increases, as is typically the case when the two asperities are in contact, whereas light- and dark blue areas are dominated by relaxation of asperities, which occurs either after contact (when the drawn-out dangling ends of the broken solid bridge retract) or at the very beginning of a high-load simulation (cf. Fig. 4.15), where high pressure and shear lead to asperity deformation without solid-solid contact. In the green parts of the maps, the virtual asperity surface area does not change. Note that the “creeping relaxation” of asperities (as can be seen for $t > 9.8$ ns in the top of Fig. 4.17) cannot be visualized well in these maps due to the small gradients involved.

Looking at the SPM-representations of the surface geometry development in Figs. 4.10 and 4.11, the first five passes of the semi-spherical asperity system are dominated by intense asperity contact, as can also be seen in the top panel of Fig. 4.17. The changes in the shape of the asperities over time are evident. Note the image of pass 5 at 1.0 ns, which shows the system shortly after the unrelaxed protrusion of the top asperity has snapped onto the lower one, instantly reducing $A_{\text{vir}}(L, t)$ for $L = 24.8$ nN by more than 1 nm^2 . The final shape of the asperities is already visible after pass number 5, when asperity contact and plastic deformation have become negligible. It now looks very similar to the slanted-pyramid asperity in Fig. 4.11, where the two asperities engage in moderate contact only during the first pass, which blunts the tips sufficiently to prevent further contact. Therefore, the final configuration can already be seen during pass number 3. Note that the first 0.5 ns visible in the lower panel of Fig. 4.17 indicate that deformation of the asperities already takes place before they first touch, which may reduce the overall intensity of asperity contact. The fact that the final shape of this asperity type does not differ very much from its initial one, and that the final geometries of both asperity types (semi-spherical and slanted pyramid) are also very similar, suggests that the (blunted) slanted pyramid is the final asperity geometry in a unidirectional mixed-lubrication sliding simulation/experiment, regardless of the initial configuration.

4.2.4 Constitutive system parameters

The load dependence of the friction force differs considerably between the asperity types for $p = 1$, as can be seen in Fig. 4.18 (a) and (b). However, as p grows and the influence of solid-solid contact declines, the behavior becomes almost identical, with the slope of the essentially linear load dependence for $p = 10$ leading to the same coefficient of friction μ for both systems.

The least squares fitting procedure described in section 3.4.2 yields the system parameters as a function of the pass number p , shown in Fig. 4.18 (c) and (d). As in section 4.1, σ_i is based on the statistical inefficiency and calculated using Eqs. (3.13) and (3.14).

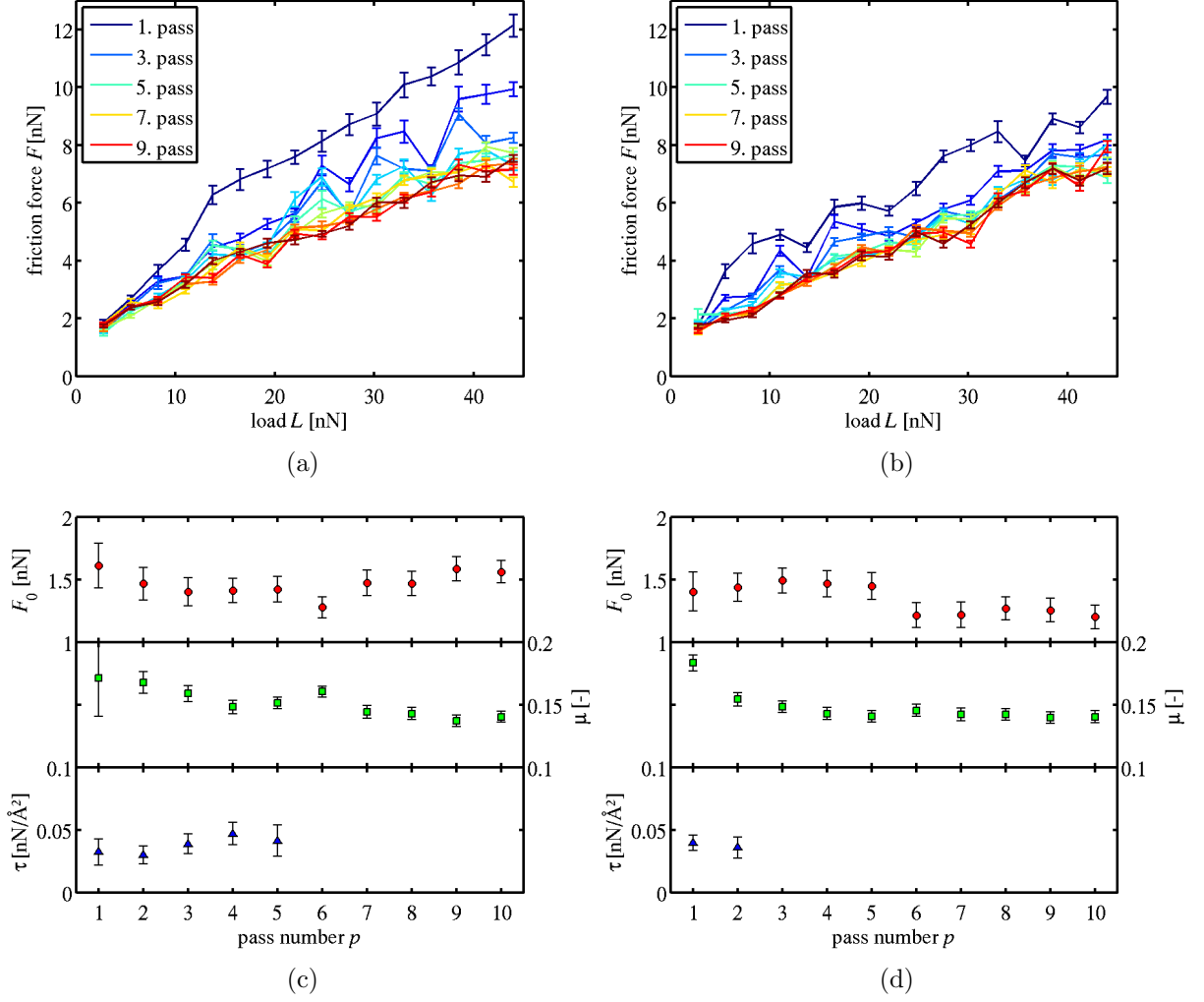


Figure 4.18: Load-vs.-friction behavior of the semi-spherical (a) and the slanted pyramid asperity (b). Results for the individual passes p are shown superimposed. The error bars represent $\sigma_{\text{si},x}$ based on the statistical inefficiencies of the MD friction force values. Bottom row: development of the system parameters $F_0^{(p)}$, $\mu^{(p)}$, and $\tau^{(p)}$ as a function of the pass number p for the semi-spherical (c) and the slanted pyramid asperity (d). The error bars are $\Delta F_0^{(p)}$, $\Delta \mu^{(p)}$, and $\Delta \tau^{(p)}$ from the least squares fitting procedure.

The force offset $F_0^{(p)}$ and the coefficient of friction $\mu^{(p)}$ are well-conditioned and exhibit stable behavior from one pass to the next. The shear strength $\tau^{(p)}$, however, is more problematic since it becomes highly ill-conditioned for passes in which at none of the simulated loads appreciable contact $A_{\text{asp}}(L)$ occurs, as already explained in section 3.4.2. This becomes more and more likely for higher pass numbers, as the system has already run in and asperity tips have blunted, leading to values for $\tau^{(p)}$ either off by two orders of magnitude or even negative, with $\Delta\tau^{(p)}$ becoming very large accordingly.

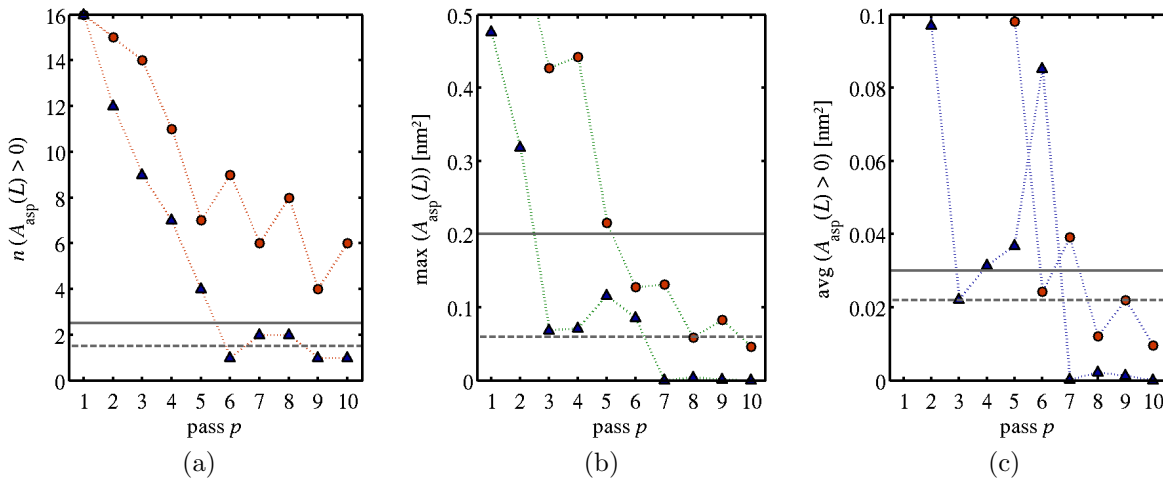


Figure 4.19: Three indicators for formulating practical criteria whether to consider a given value of $A_{\text{asp}}(L)$ in the fitting procedure. Red circles represent the semi-spherical asperity, while blue triangles represent the slanted pyramid asperities. Horizontal lines mark the stricter (solid line) and the less strict (dashed line) minimum value for each indicator.

Therefore in practice, the theoretical criteria introduced in section 3.4.2 which lead to the omission of $\tau^{(p)}$ from the fitting procedure have to be reformulated. Two empirically found sets of criteria may be applied, with the less strict one merely avoiding divergence of $\tau^{(p)}$, while the stricter one also prevents large values of $\Delta\tau^{(p)}$. In the following list, the stricter criterion used in this work is followed by the less strict one in parentheses (see also Fig. 4.19):

- the number of loads for which $A_{\text{asp}}(L) > 0$ must be greater than 2 (1),
- the maximum $A_{\text{asp}}(L)$ for a given pass must be greater than 0.06 nm² (0.2 nm²), and
- the value for $A_{\text{asp}}(L)$ averaged over all loads which have asperity contact must be greater than 0.022 nm² (0.03 nm²).

By comparison, with the potential parameters used, the cross-section of an Fe atom is roughly 0.064 nm^2 . In cases where these criteria are not met, it makes sense to perform the least squares fitting for $F_0^{(p)}$ and $\mu^{(p)}$ only, as described in section 3.4.2, and leave $\tau^{(p)}$ undefined.

The results shown in Fig. 4.18 (c) and (d) strongly suggest that for the run-in system F_0 , τ and μ are indeed constitutive system parameters, namely

$$\begin{cases} F_0^{(p)} \simeq F_0 \\ \tau^{(p)} \simeq \tau \\ \mu^{(p)} \simeq \mu \end{cases}, \quad \forall p > p_{\text{run-in}}. \quad (4.3)$$

Here $p_{\text{run-in}}$ is the number of the pass during which the nanoscopic run-in is completed. We now define the run-in system parameters F_0 , μ , and τ as the averages of the single-pass parameters $F_0^{(p)}$, $\mu^{(p)}$, and $\tau^{(p)}$ for which $p > p_{\text{run-in}}$, and their errors as the associated standard deviations. Fig. 4.20 shows these parameters as a function of $p_{\text{run-in}}$. The

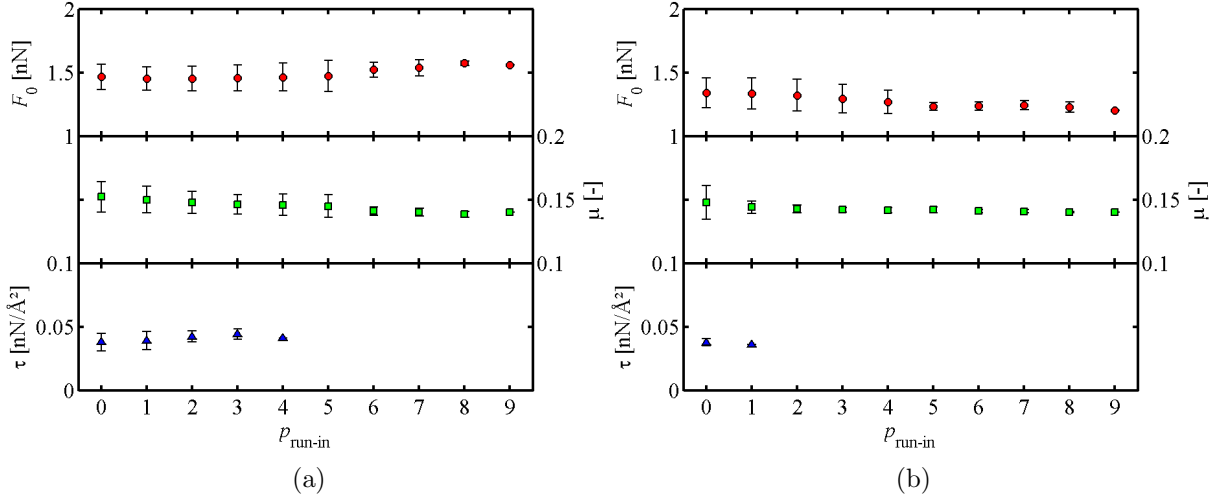


Figure 4.20: The run-in system parameters F_0 , μ , and τ as a function of $p_{\text{run-in}}$ for the semi-spherical (a) and the slanted pyramid asperity (b). The error bars are the standard deviation calculated from all values of $F_0^{(p)}$, $\mu^{(p)}$, and $\tau^{(p)}$ for which $p > p_{\text{run-in}}$.

error bars of F_0 and μ in the system with the semi-spherical asperity, cf. Fig. 4.20 (a), simultaneously decrease quite sharply in size between $p_{\text{run-in}} = 5$ and 6. Moreover, asperity contact has subsided at that stage, so τ is no longer defined. One can therefore conclude that the run-in process has finished after 6 passes in this system. The slanted pyramid asperity system does not exhibit such clear-cut behavior, especially since $F_0^{(p)}$ has an unexpected jump from pass 5 to 6, so the error bars of F_0 remain quite large until $p_{\text{run-in}} =$

5 in Fig. 4.20 (b). The end of run-in can therefore be only approximately set between $p_{\text{run-in}} = 1$ and 5. Note that for both asperity types the effective shear strength τ remains at a constant level and can therefore also be considered a system parameter while it is well defined.

The good coincidence of subsiding asperity contact with the end of the run-in period as determined by the variance of the constitutive system parameters is strong evidence that steady-state sliding of nanosystems in the mixed lubrication regime can be sufficiently well described by the Derjaguin friction law, whereas the run-in period can only be properly characterized with the proposed three-term kinetic friction law.

We can conclude that SPM is a suitable tool for monitoring repeated asperity-asperity contact in MD shear simulations of mixed lubrication. It allows the analysis of the time-development of the involved constitutive system parameters, namely the friction force offset $F_0 > 0$, the effective shear strength τ , and the coefficient of friction μ . If no solid-solid contact occurs for any of the considered loads, i.e., $A_{\text{asp}}(L)$ strictly vanishes and hence the Derjaguin-form of the three-term friction law holds, it was found that the same computational scheme yields only two constitutive system parameters, $F_0 \geq 0$ and μ . While $A_{\text{asp}}(L) \geq 0$ depends on L during the nanoscopic run-in period, it was demonstrated that the constitutive system parameters entering the three-term friction law slightly depend on time, but become time-independent quantities as soon as asperity contact subsides.

4.3 Linking the Derjaguin-offset to Lubricant Disorder

In the last two sections, systems were considered in which direct asperity contact plays a crucial role in their frictional properties. While this is necessary for applying and validating the three-term kinetic friction law, the occurrence of asperity contact makes the interpretation of the Derjaguin-offset F_0 difficult.

In this section I will therefore discuss results of simulations carried out with systems where the roughness is so small that asperities can never touch directly as in Refs. [25, 26, 27, 41]. The system parameter τ is thus not accessible via the fitting procedure, so here the focus lies on the influence of lubricant type, lubricant coverage and nano-roughness of the Fe sliders on the remaining system parameters, the coefficient of friction μ and the Derjaguin-offset F_0 .

Since this study reveals that non-vanishing values for F_0 occur when the lubricant in the nanotribological systems is less ordered, nine systems with high and low values of F_0 are analyzed further. As a first step, the lubricant-lubricant interface as well as the material density distribution are visualized using SPM. Then an attempt is made to relate the friction force offset F_0 to variously estimated entropies of the lubricant, which can be seen as a measure for its structural disorder [40].

4.3.1 Specific system setup

The nanotribological systems featured in this section are prepared following the general guidelines for small substrates in chapter 2. The substrates consist of either 6 monolayers of bcc Fe(100) or an equivalent amount of 1014 atoms of amorphous Fe. The crystalline substrates may feature roughness from 1–4 ML bcc Fe(100) in the form of three Fe islands as described in section 2.1.1. Amorphous substrates have an inherent roughness R_a equivalent to $\simeq 0.5$ ML bcc Fe(100). Each slider is covered with a boundary lubricant layer of either stearic acid (blue), oleic acid (orange) or methyl stearate (green) molecules. The lubricant coverage η is varied from 35 to 63 molecules per slider using initial molecular grids of 5×7 , 6×7 , 6×8 , 7×8 , and 7×9 . In some systems, six monolayers of *n*-hexadecane (red) as a base oil are sandwiched between two boundary layers of stearic acid, forming a binary lubricant. Some examples for various of the described MD-nanosystem setups can be seen in Fig. 4.21. A system with oleic acid was already shown in Fig. 2.14. The applied loads range from 1.38 to 22.04 nN, with at least 3, but usually 5 or 6 different loads per configuration. After a dynamic equilibration period of 0.5 ns, during which the sliding velocity is ramped to and kept at 4 m/s, the contact forces are recorded for 1.5 ns as explained in section 3.3.

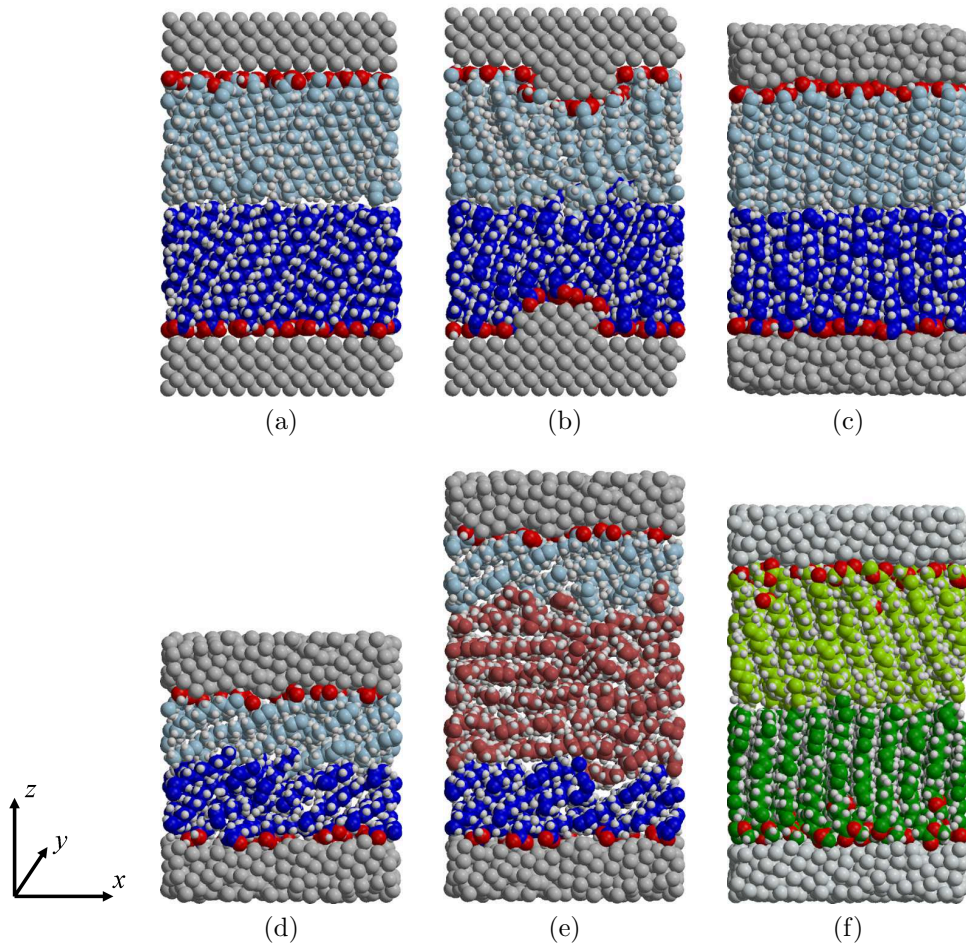


Figure 4.21: Examples for MD-nanosystem setups. The meaning of the abbreviations can be found in table 4.2. (a) SteAc-7 \times 9-0ML, (b) SteAc-7 \times 9-4ML, (c) SteAc-7 \times 9-amo, (d) SteAc-5 \times 7-amo, (e) Hex-5 \times 7-amo, (f) MeSte-7 \times 9-amo.

4.3.2 Time-dependence of friction force

The friction force $F(L)$ as a function of time for two different MD-nanosystems at a constant load $L = 2.76$ nN can be seen in Fig. 4.22. The blue curve denotes the stick-slip type behavior of the highly ordered system from Fig. 4.21 (a), while the red curve shows the time development of the same system with 6 monolayers of *n*-hexadecane sandwiched between the two films of stearic acid, which is much smoother and has an average value which is roughly half of the other system.

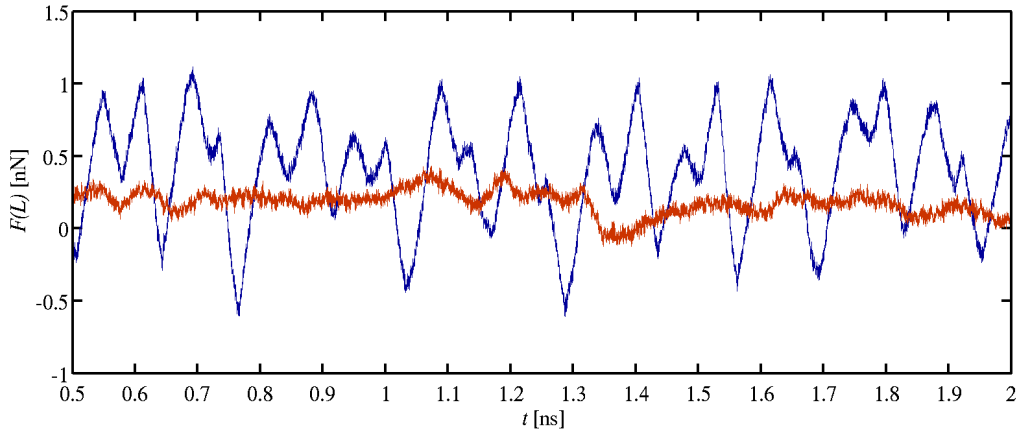


Figure 4.22: Friction force as a function of time. Blue curve: 7×9 stearic acid molecules per flat bcc Fe(100) slider. Red curve: 7×9 stearic acid molecules per flat bcc Fe(100) slider sandwiching 6 ML of *n*-hexadecane. Both curves are running averages with a time window of $\Delta t = 30$ ps.

4.3.3 Load-vs.-friction

The load and the friction force are both time-averaged over the data acquisition period. Since no solid-solid contact occurs, the Derjaguin friction law, Eq. (3.16), holds, so the remaining two system parameters F_0 and μ can be fitted by solving Eq. (3.22) for every system. A complete list of fitted system parameters together with their respective errors calculated according to Eq. (3.23) can be found in appendix C. Fig. 4.23 shows the load-vs.-friction behavior of selected groups of tribosystems, each panel with a different parameter kept constant. The meaning of the abbreviations in the legends can be found in table 4.2. The error bars on the friction forces have been omitted for better readability.

The left column in Fig. 4.23 compares the load-vs.-friction behavior when the nano-roughness of the sliders is increased, while the right column compares different lubricant coverages. Note that the left and the right column have different legends.

Fig. 4.23 (a) compares systems with amorphous sliders featuring very low nano-roughness, where all systems show strong coverage-dependence of the friction forces. Generally, reducing η will make friction forces grow, especially via an increased μ . This picture

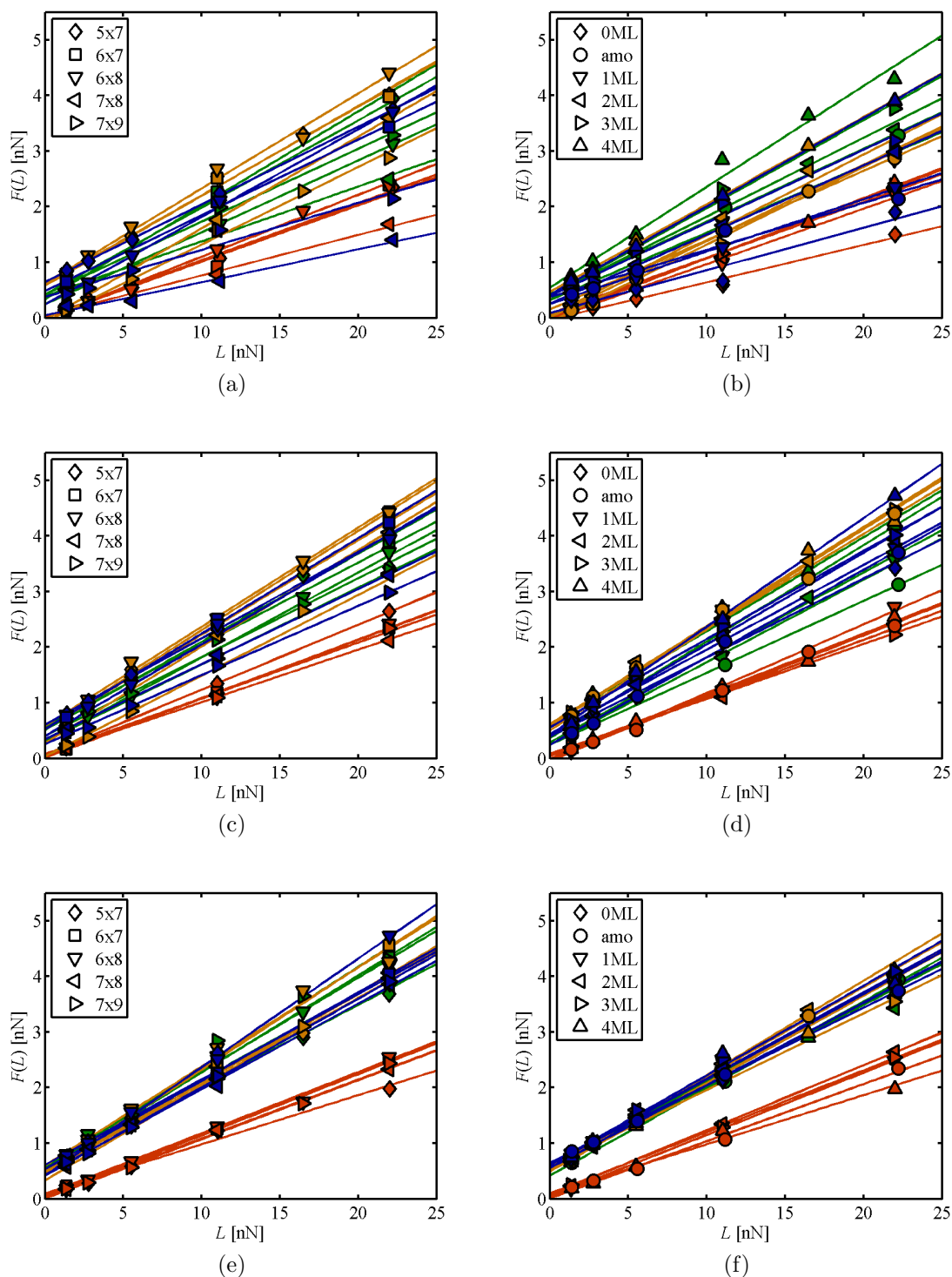


Figure 4.23: Load-vs.-friction curves for various groupings of nano-tribosystems. The meaning of the abbreviations can be found in table 4.2. (a) amo, (c) 2ML, (e) 4ML, (b) 7×9, (d) 6×8, (f) 5×7. Colors: SteAc—blue, OleAc—orange, MeSte—green, Hex—red.

SteAc	stearic acid (boundary lubricant type)
MeSte	methyl stearate (boundary lubricant type)
OleAc	oleic acid (boundary lubricant type)
Hex	SteAc + <i>n</i> -hexadecane (base lubricant)
$k \times l$	molecules per slider (boundary lubricant surface coverage η)
m ML	monolayers of bcc Fe(100) (surface nano-roughness R_a)
amo	amorphous substrate (no explicit roughness, classified as $R_a \simeq 0.5$ ML)

Table 4.2: Key to the used abbreviations.

does not change much with a slight increase in nano-roughness to $R_a = 2\text{ML bcc Fe}(100)$, although friction forces in general go up, see Fig. 4.23 (c). However, when the roughness is set to $4\text{ML bcc Fe}(100)$, cf. Fig. 4.23 (e), the pattern changes. All boundary-lubricated systems now have very comparable load-vs.-friction behavior, irrespective of η . There is a noticeable gap between the fit lines of the boundary-lubricated systems and those of the ones including *n*-hexadecane as a base oil.

Fig. 4.23 (b) shows an overview of the different systems' friction behavior at high boundary lubricant coverage ($\eta = 63$ molecules/slider), where the friction forces exhibit strong roughness dependence, especially those of stearic acid and methyl stearate. As the roughness increases, friction forces go up, and so does the slope of the fits, μ . This behavior is typical of well-ordered and dense surface films, since any roughness feature underneath such a film is almost perfectly reproduced on top of it. It is not surprising that the red curves representing the systems with *n*-hexadecane sandwiched between the films of stearic acid show somewhat less roughness dependence and generally have lower friction forces. This is due to the fact that the *n*-hexadecane molecules are not attached to any surface and can therefore better even out the roughness features at the top of the stearic acid films.

The systems with intermediate boundary lubricant coverage ($\eta = 48$ molecules/slider) in Fig. 4.23 (d) already show less roughness dependence as can be seen by comparing the spread of the fit lines with that of Fig. 4.23 (b). Moreover, a gap seems to emerge between the fit lines of the systems which are only boundary lubricated and those which also have a layer of base oil, with the latter exhibiting lower friction forces. This gap becomes very distinct in Fig. 4.23 (f), where η has been reduced to 35 molecules/slider. Here, most of the boundary-lubricated systems have virtually the same friction forces irrespective of roughness. This could be due to the less-ordered boundary lubricant layers having more freedom to rearrange themselves according to the surface features of the slider, filling the

troughs between asperities and ensuring a more even sliding interface. However, due to the increased possibility of dissipation within the film, friction forces remain high. Adding six monolayers of *n*-hexadecane lowers friction forces considerably, especially via reduction of F_0 . The lower friction forces here are most likely due to the transverse layering of the *n*-hexadecane which causes a more even sliding interface.

4.3.4 Constitutive system parameters

Figs. 4.24 and 4.25 compare the lubricant coverage dependence of F_0 and μ for the 4 main categories of considered lubricants, with the slider nano-roughness as a parameter. Note that in Figs. 4.24–4.27, the symbols have been somewhat spread out laterally so they do not obscure each other. All boundary lubricated systems have in common that F_0 generally decreases with increasing coverage. They share a common maximum value of $F_0 \simeq 0.6$ nN at low coverage, decreasing to values around zero for systems with negligible roughness and 0.5 for rough systems. At high lubricant coverage, there exists a pronounced roughness dependence of F_0 , which is also obvious by comparing with Fig. 4.26. By contrast, the systems which contain 6 ML of *n*-hexadecane as a base lubricant between the two boundary lubricant layers of stearic acid, F_0 fluctuates around zero independently of boundary lubricant coverage, and with a very slight dependence on nano-roughness, see Fig. 4.26 (d).

Comparing the coverage dependence of μ , one notices local maxima for the three boundary-lubricant-only systems at coverages between 42 and 56 molecules/slider, depending on the lubricant. Systems with coverages higher or lower than these values exhibit lower coefficients of friction and therefore better frictional properties at high loads. Values of μ vary between 0.05 and 0.2 for stearic acid, between 0.1 and 0.2 for oleic acid and methyl stearate, while μ remains almost constant at 0.1 for all systems with *n*-hexadecane.

One can observe that higher values for F_0 occur when the lubricant in the nanotribological systems is less ordered. Motivated by this, nine systems out of the system matrix discussed above are selected for further analysis. Three systems each were chosen with the lubricant types stearic acid, oleic acid, and methyl stearate, such that one of them exhibits $F_0 \simeq 0$, and the other two have $F_0 > 0$, once induced by low lubricant coverage η and once due to high surface roughness R_a . These systems, along with their key parameters, are listed in table 4.3, and snapshots of their geometries are shown in the insets of Fig. 4.28.

4.3.5 SPM-visualization of lubricant-lubricant interface

SPM-visualizations of the nine selected systems can be seen in Fig. 4.29. By treating the upper and the lower boundary lubricant layers in the lubrication gap individually, one can visualize the lubricant-lubricant interface which, depending on R_a and η may become noticeably larger than the apparent contact area which is equal to the xy cross-section

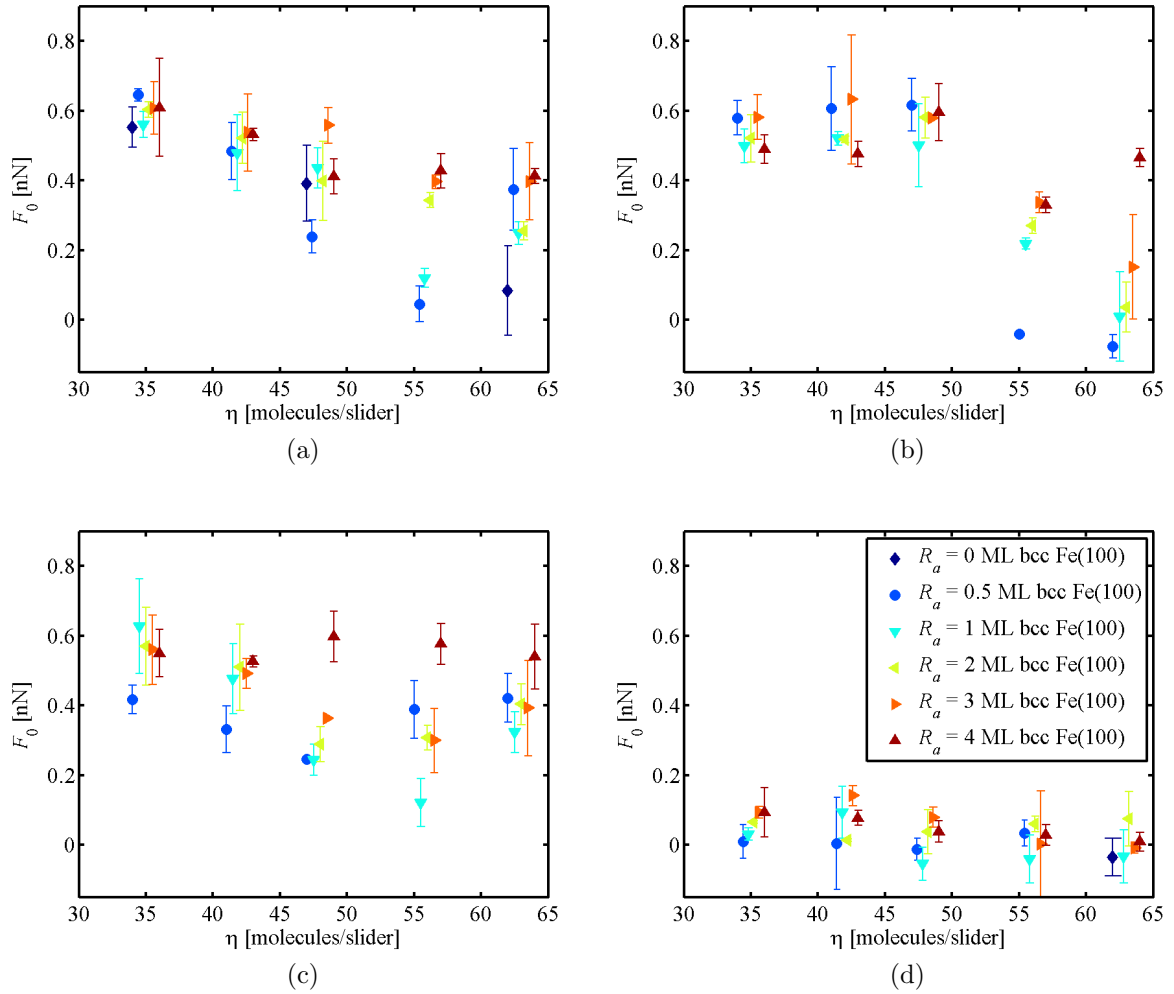


Figure 4.24: Boundary lubricant coverage dependence of the Derjaguin-offset F_0 with the nano-roughness R_a as a parameter for 4 different lubricant types. (a) stearic acid, (b) oleic acid, (c) methyl stearate, (d) stearic acid with n -hexadecane.

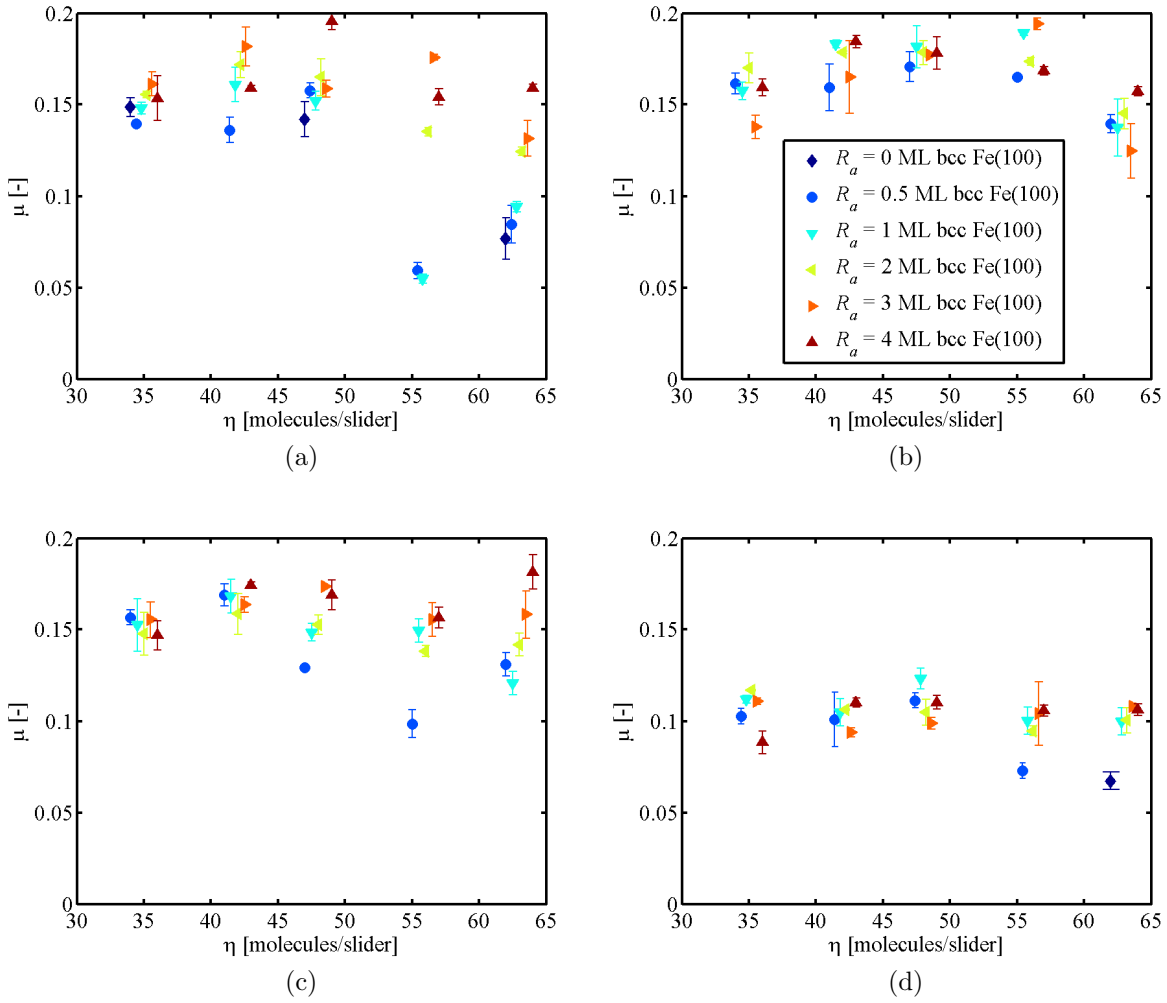


Figure 4.25: Boundary lubricant coverage dependence of the nanoscopic coefficient of friction μ with the nano-roughness R_a as a parameter for 4 different lubricant types. (a) stearic acid, (b) oleic acid, (c) methyl stearate, (d) stearic acid with *n*-hexadecane.

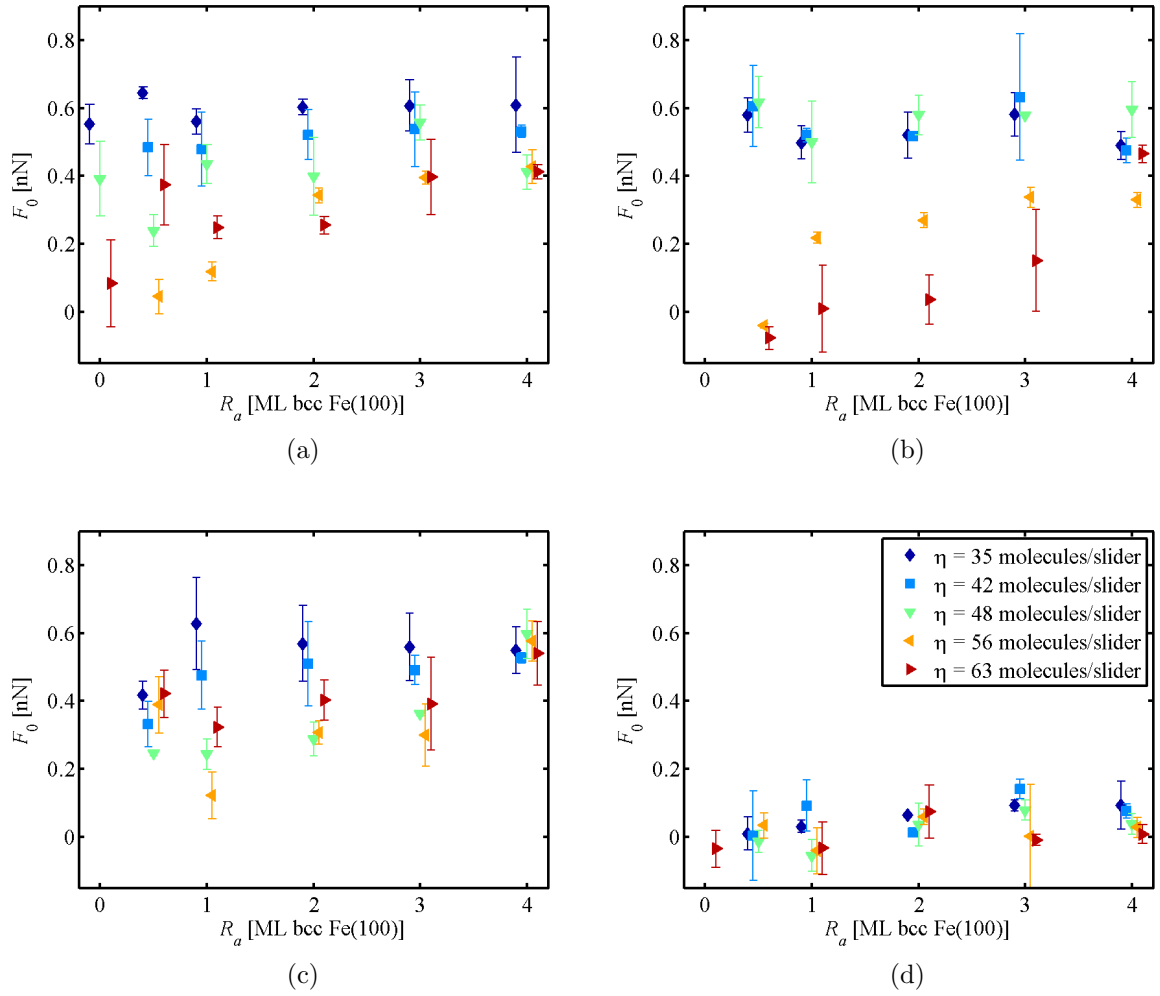


Figure 4.26: Nano-roughness dependence of the Derjaguin-offset F_0 with the boundary lubricant coverage η as a parameter for 4 different lubricant types. (a) stearic acid, (b) oleic acid, (c) methyl stearate, (d) stearic acid with *n*-hexadecane.

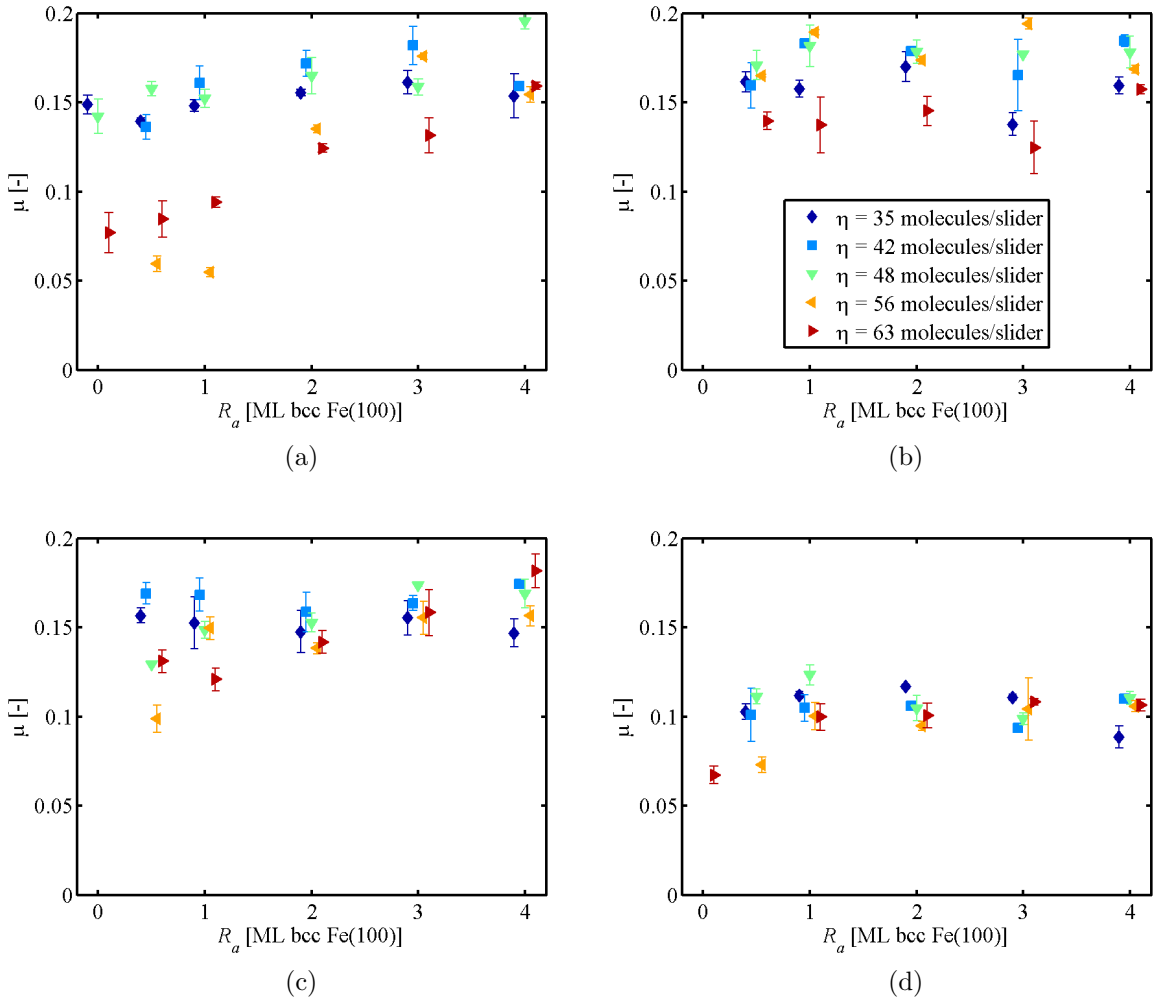


Figure 4.27: Nano-roughness dependence of the nanoscopic coefficient of friction μ with the boundary lubricant coverage η as a parameter for 4 different lubricant types. (a) stearic acid, (b) oleic acid, (c) methyl stearate, (d) stearic acid with *n*-hexadecane.

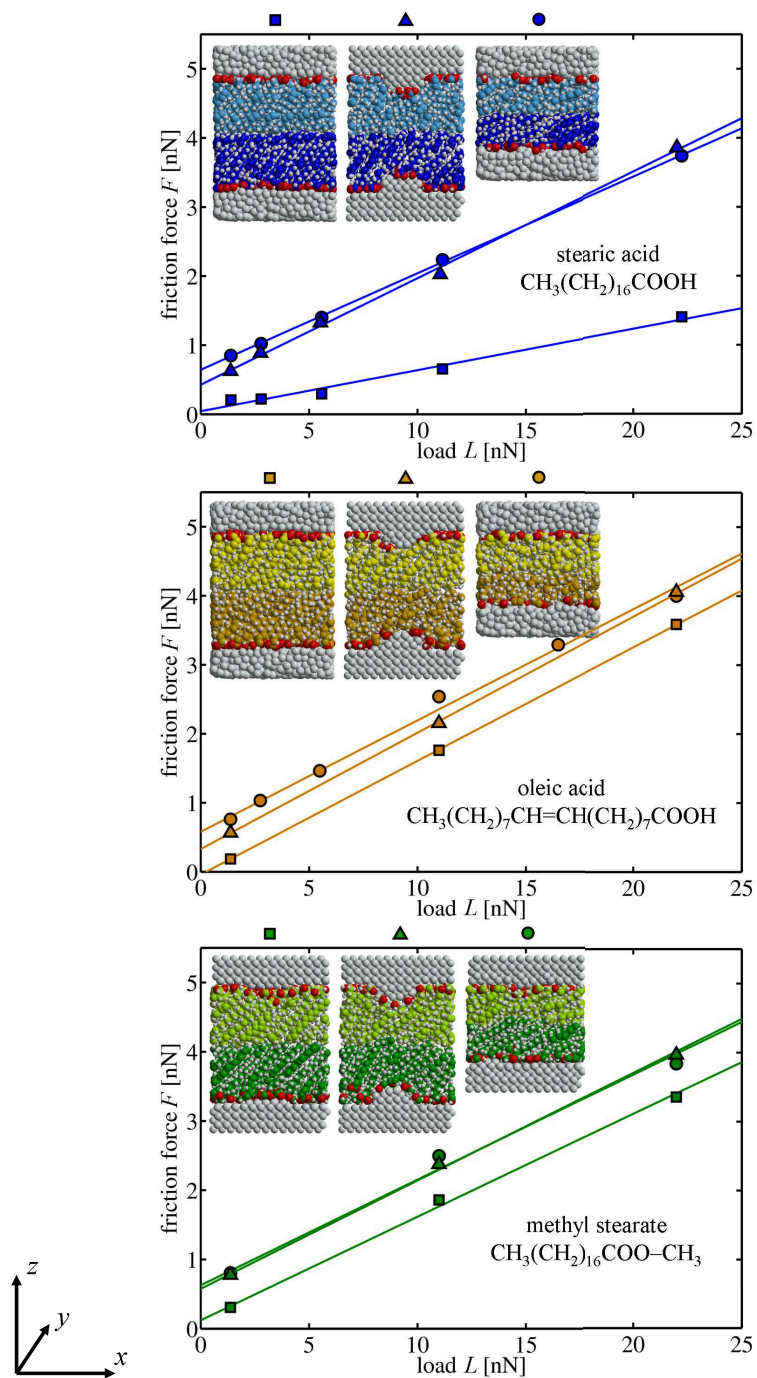


Figure 4.28: Load-vs.-friction behavior of the nine selected nanotribological systems with geometry snapshots shown in the insets. Values for boundary lubricant coverage and nano-roughness as well as a key for the used symbols are listed in table 4.3.

lubricant type	R_a [ML bcc Fe(100)]	η [molecules/slider]	symbol
stearic acid	0.5	56	blue square
stearic acid	4	56	blue triangle
stearic acid	0.5	35	blue circle
oleic acid	0.5	56	orange square
oleic acid	4	56	orange triangle
oleic acid	0.5	35	orange circle
methyl stearate	1	56	green square
methyl stearate	4	56	green triangle
methyl stearate	1	35	green circle

Table 4.3: The nine systems selected for further analysis.

of the simulation box. The systems in Fig. 4.29 are ordered by growing F_0 from left to right, and when comparing the green lubricant-lubricant interfaces, one can see a slight increase in the interfacial roughness between the systems in the left column (with low R_a and high η) and those in the center column (with high R_a and high η). However, the systems in the right column (with low R_a and low η) all exhibit a substantially rougher lubricant-lubricant interface than the high- η systems. It therefore seems that this interfacial roughness alone cannot explain the large differences in F_0 between the systems in the left column, where $F_0 \simeq 0$, and the ones in the other two columns, where $F_0 \simeq 0.6$. To understand the somewhat surprisingly low interfacial roughness introduced by the asperities, it must be taken into account that the high lubricant density does not allow the molecules adsorbed to the asperity tips to laterally avoid the molecules of the opposing lubricant layer. These molecules must therefore reduce their length by twisting into shorter conformations, which requires a certain energy that might have an influence on F_0 .

The rear faces of the SPM-representations in Fig. 4.29 are colored according to the material density ρ as introduced in Eq. (3.2). When visually comparing the density patterns, it becomes apparent that the lubricant order is reduced from left to right, where the three asperities on the slider surface in the center column introduce a slight degree of disorder, and the decreased boundary lubricant coverage in the right column yields a quite chaotic lubricant density pattern. However, to make any proper comparative statements, the degree of disorder has to be quantified, which will be done in the next section.

4.3.6 Derjaguin-offset versus lubricant order

The load-vs.-friction data of the nine selected tribosystems in Fig. 4.28 are used to fit the constitutive system parameters F_0 and μ , shown in Fig. 4.30. The error bars are ΔF_0 and $\Delta \mu$ from the least squares fitting procedure. Notably, the highly ordered system with 56 molecules of stearic acid covering an amorphous Fe surface with low roughness

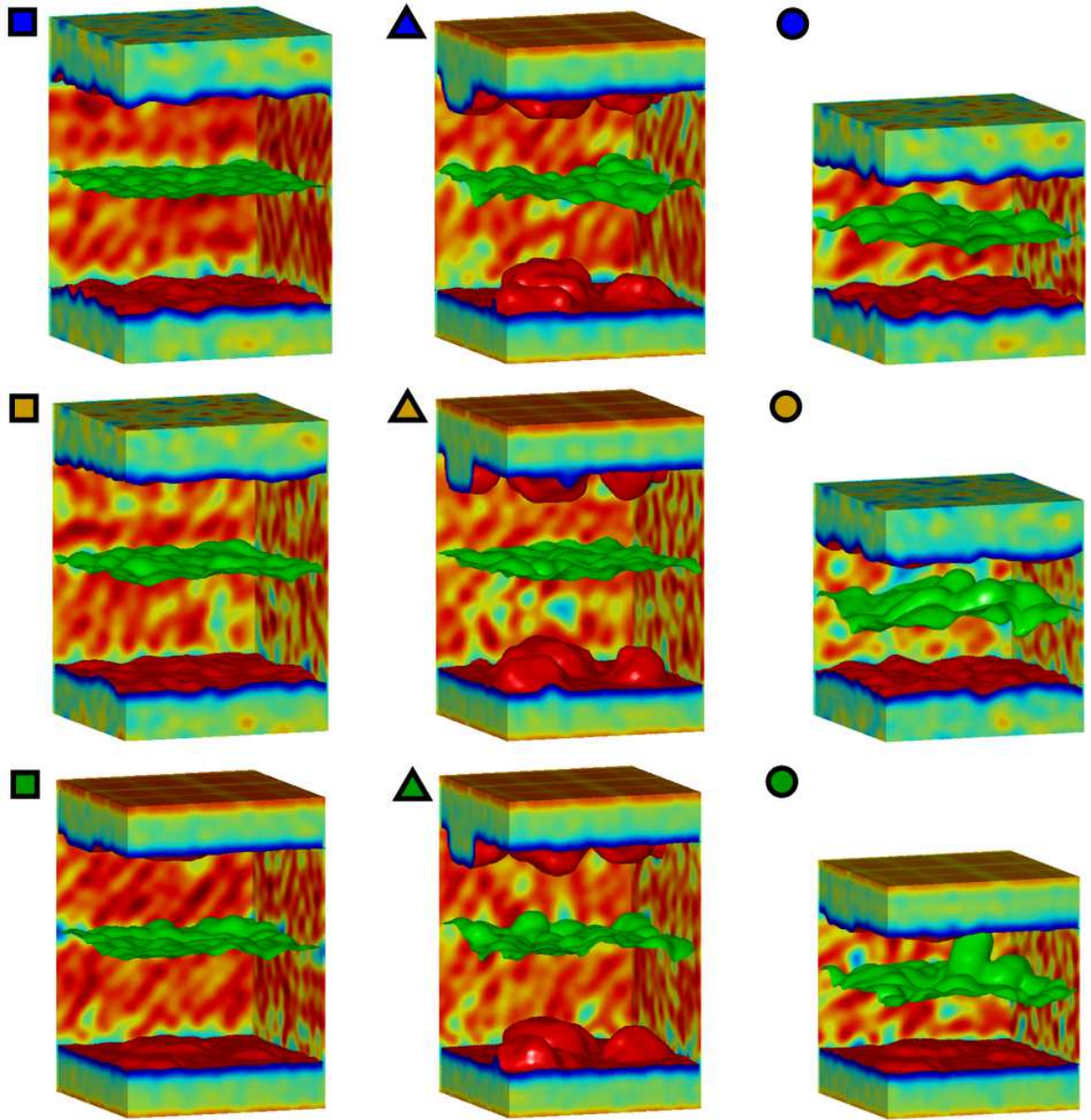


Figure 4.29: SPM-visualizations of the nine systems shown in Fig 4.28. Top row—SteAc, center row—OleAc, bottom row—MeSte. The lubricant-lubricant interfaces are shown as solid-green surfaces, while the Fe surfaces are solid-red. The rainbow-style coloring of the rear faces of the simulation boxes symbolizes the material density ρ as introduced in Eq. (3.2), where dark red areas denote high and blue ones denote low density.

has a coefficient of friction μ much lower than all other systems. In the following, an attempt will be made to link the behavior of F_0 to the lubricant order, which is quantified by various estimates for contributions to its entropy based on the $3N \times 3N$ covariance (super)matrix \mathbf{C} introduced in Eq. (3.35). These were obtained by time-averaging over a data acquisition period of 1.5 ns, based on the lubricant molecules' carbon backbone positions in the center-of-mass system.

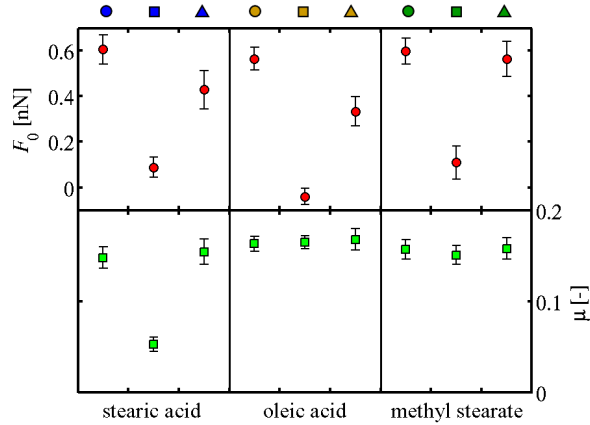


Figure 4.30: The constitutive system parameters F_0 and μ in accordance with the linear load-vs.-friction behavior from Fig. 4.28.

The maps shown in Fig. 4.31 are representations of these covariance (super)matrices, which have been rearranged in a block-wise fashion so that the nine sub-matrices constitute the Cartesian component-wise covariance matrices. All sub-matrices featuring the x -component show clear evidence of the dominant translation in x -direction. The remaining four sub-matrices reveal patterns according to the vibrational modes of the molecules, as will be shown below.

In order to estimate the contributions to the total entropy based on Eqs. (3.39), (3.40) and (3.44), the covariance (super)matrix \mathbf{C} must be diagonalized, for example by using an orthonormal coordinate transformation, which yields eigenvalues λ_J ($J = 1, \dots, 3N$) in decreasing order. Following this, the translational, rotational and vibrational eigenmodes can be identified among the normalized eigenvectors \mathbf{V}_J ($J = 1, \dots, 3N$) which form the columns of the transformation matrix \mathbf{V} in Eq. (3.42). Although it is expected that the eigenvector corresponding to the largest eigenvalue λ_1 describes the collective sliding motion along the x -axis in all of the nanotribological systems investigated here, a symmetry study of the other eigenvectors \mathbf{V}_J ($\forall J \geq 2$) should be carried out because one has to distinguish between the other collective modes as well. Therefore one attempts to identify eigenvectors \mathbf{V}_J stored in the transformation matrix \mathbf{V} with a structure of, e.g., $(1 \ 0 \ 0 \ 1 \ 0 \ 0 \ \dots \ -1 \ 0 \ 0 \ -1 \ 0 \ 0)^T$. This structure has three possible permutations with respect to the Cartesian components, each of which characterizes a purely collective translational motion along the axis for which the corresponding Cartesian

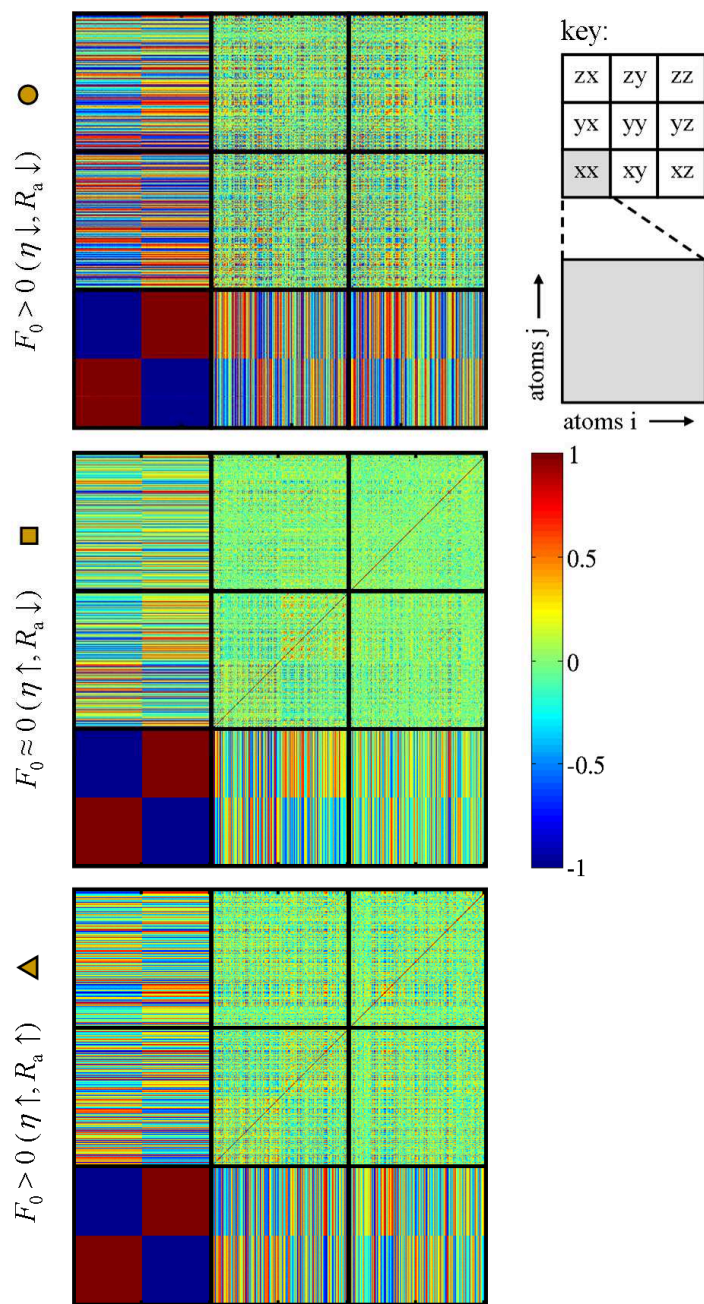


Figure 4.31: Maps of the covariance (super)matrices of the three nanotribological systems from Fig. 4.28 with oleic acid as a lubricant at a load of $L = 11.02$ nN. The elements are calculated averaging over the entire data acquisition period of 1.5 ns and taking the Cartesian components of the atomic positions with respect to the momentary center of mass, see also key.

component does not vanish. Three differently structured typical eigenvectors can stand for collective rotational motions in a given Cartesian coordinate plane about the center of mass. One of the easiest ways to identify these six eigenvectors is to represent in a histogram the number of occurrences within the transformation matrix \mathbf{V} of a given element, because for a purely collective translational motion, ± 1 would be present in the histogram $N/2$ times and so on. Such a histogram formed with the elements of \mathbf{V} and common to all the nanotribological systems considered in Fig. 4.28 is shown in Fig. 4.32 (top). In this figure, two tiny outlier peaks are present which were found to correspond to \mathbf{V}_1 . By drawing the Cartesian component-resolved histogram of \mathbf{V}_1 in Fig. 4.32 (bottom), it becomes evident that \mathbf{V}_1 describes the collective motion due to the sliding along the x -direction. Inspecting the values of the components, apart from the symmetry of \mathbf{V}_1 , it is evident that this collective motion also comprises random fluctuations along the other two axes. Therefore and due to normalization of the eigenvector, the repeated x -component value differs from unity. Furthermore, as can be seen in Fig. 4.32, there is no evidence of any other translational or rotational collective modes, which means that all the remaining ones are vibrational.

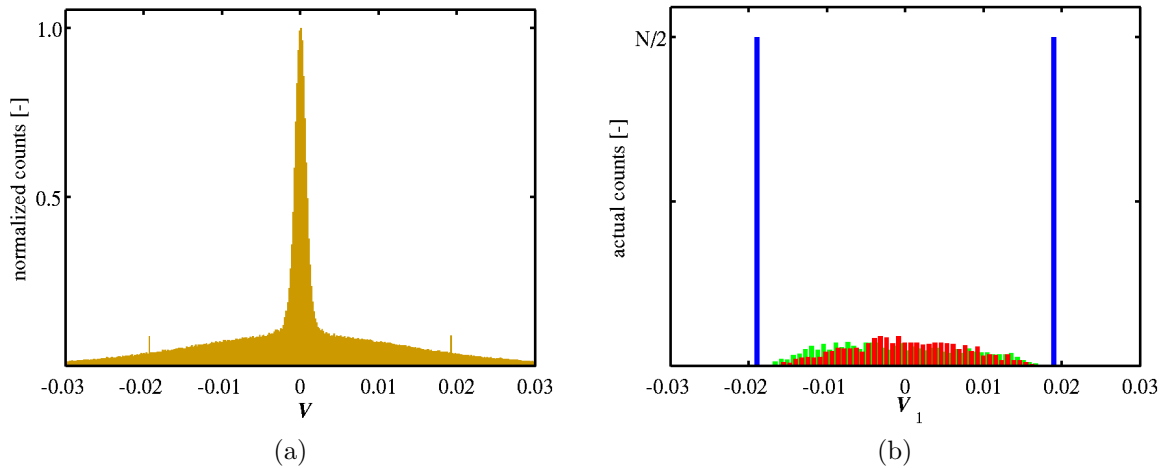


Figure 4.32: Histogram of all components of all normalized eigenvectors corresponding to eigenvalues greater than 10^{-5}Å^2 (a) and of the dominant one \mathbf{V}_1 (b; blue— x , green— y , red— z) obtained by diagonalizing the covariance (super)matrix shown in Fig. 4.31 (middle). $N = 2016$ is the number of C -atoms in the system. The two peaks at $\sim \pm 0.02$ hint at pure translation without rotation.

In view of these findings, it is now clear that for estimating the translational contribution S_{tr} to the entropy, Eq. (3.39) is not directly applicable, but instead its 1D counterpart,

$$S_{\text{tr}} = R \ln \left[\left(\frac{e^2 m k_B T}{\hbar^2} \right)^{1/2} \sigma_x \right], \quad (4.4)$$

for which σ_x can be well approximated by the square root of the first eigenvalue λ_1 , namely

$$\sigma_x = \sqrt{\lambda_1} . \quad (4.5)$$

Indeed, comparing this 1D-estimate for S_{tr} with the one obtained for σ_x , the square root of the corresponding eigenvalue determined on the basis of the 3×3 covariance matrix constructed for the center of mass of the system, it turns out that the former approach yields only slightly larger values than the latter. This difference is due to the small random y and z components in \mathbf{V}_1 , recall Fig. 4.32. Accordingly, in the case of the vibrational contribution S_{vib} to the entropy, strictly speaking one has to deal with $3N - 1$ modes in Eqs. (3.44) and (3.45). In practice, however, it turns out that both S_{vib} and S_{Schl} converge slowly for small vibrational eigenvalues λ_J , i.e., when the frequency ω_J of the associated one-dimensional quantum harmonic oscillator tends to be extremely large, see Eq. (3.43). Fortunately, when $\lambda_J \rightarrow 0$, its contribution to the vibrational entropy S_{vib} vanishes, because

$$\lim_{\omega_J \rightarrow \infty} S_{\text{vib}}^{(J)} = R \lim_{\omega_J \rightarrow \infty} \frac{\beta \hbar}{\beta \hbar \exp(\beta \hbar \omega_J)} - R \ln 1 = R \lim_{\omega_J \rightarrow \infty} \frac{1}{\exp(\beta \hbar \omega_J)} = 0 , \quad (4.6)$$

and hence one can introduce a cut-off $\lambda_{\text{cut}} \geq 0$ below which all the positive vibrational eigenvalues λ_J can be set to zero and not counted for S_{vib} and S_{Schl} without significantly altering their values. The value for λ_{cut} was set to 10^{-5} , resulting in about 100 contributing eigenvalues per system. With that knowledge, large amounts of calculation time can be saved by not having to invert the entire matrix, but simply by approximating the $\simeq 300$ largest eigenvalues.

The results for the entropy contributions estimated in this manner are given as per-atom values in Fig. 4.33, where it can be seen that, to some extent, S_{tr} (right triangles, left axis) better follows the trend of F_0 in Fig. 4.30 than S_{vib} (diamonds, right axis). Both S_{tr} and S_{vib} correlate well with F_0 regarding changes in the lubricant surface coverage η , but do not reflect changes in F_0 due to an increase of surface roughness R_a . This could have two main reasons. On one hand, the individuality of the constitutive molecules is lost in the single macromolecule approach for the entropy, and so it seems to be unable to measure the change in the structural order due to the higher surface roughness. On the other hand, it could also be that, while the expressions for S_{tr} and S_{vib} are derived from the Shannon entropy, the quasi-harmonic (Gaussian) approach to the PDF considered here oversimplifies the interatomic potential by reducing it to an elastic one. The same holds for the Schlitter-entropy, recall Eq. (3.45), which by definition only sets an upper bound for S_{vib} —as confirmed by Fig. 4.33 (b).

In conclusion, it can be stated that if $A_{\text{asp}}(L) \equiv 0$ for all L considered, it was found that the occurrence of the offset F_0 can be partially related to the structural order of the system by estimating the load-dependent entropy with the single macromolecule approach, which is based on covariance (super)matrices of the carbon backbone atoms in the lubricant.

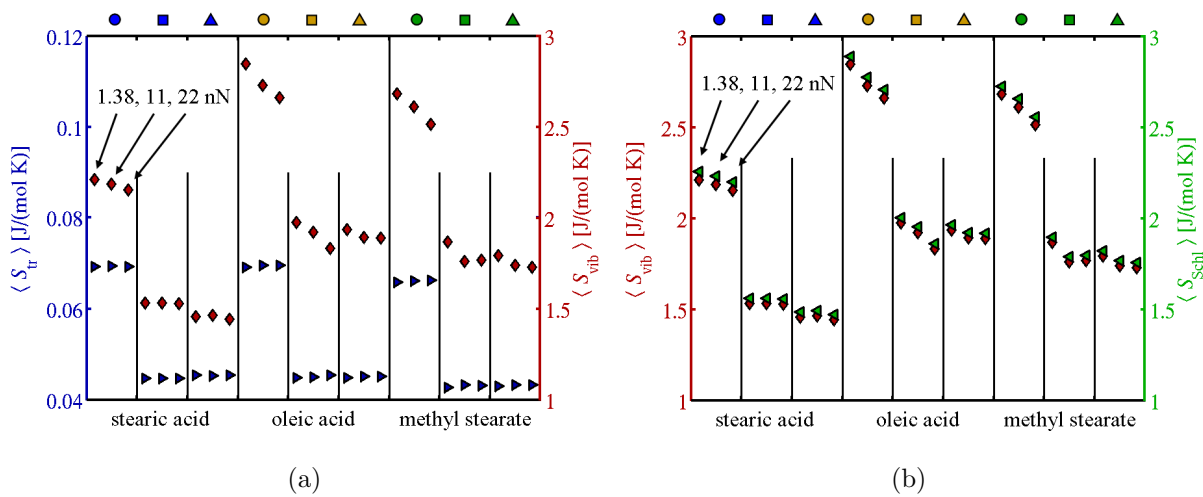


Figure 4.33: Molar per-atom contributions to the entropy within the single macromolecule approach and following Schlitter's *ad hoc* approximation, for all nanotribological systems in Fig. 4.28. The translational entropy values are represented by blue right triangles, the vibrational ones by red diamonds, and green left triangles stand for the configurational entropy according to Schlitter.

Conclusion

In this thesis, I proposed a three-term kinetic friction law at nanoscale to explain the distinct non-linearities and discontinuities in the load-vs.-friction behavior of atomistically simulated tribological systems operating under mixed lubrication conditions. This law consists of the load-dependent Amontons-Coulomb term, the Bowden-Tabor term depending on the contact area between opposing asperities, and a load-independent friction force offset first introduced by Derjaguin. Through the exact knowledge of the mean asperity contact area, the applied load, and the average friction force, I could then fit the three load-independent constitutive system parameters of each system, namely the friction force offset, the effective shear strength, and the nanoscopic coefficient of friction. These three parameters can accurately reproduce the frictional response of a nanoscopic tribosystem based on the load and the asperity contact area.

The main finding of this work is that the Amontons-Coulomb friction law, where the coefficient of friction of a tribological system is defined as the friction force divided by the applied load, may produce good results at the macro and micro scale. However, as soon as one enters the mixed and boundary lubrication regimes, where the lubrication gap thickness may be reduced to a few nanometers, the occurrence of a load-independent friction force offset precludes the calculation of the coefficient of friction via a simple division. Instead, the slope of the linear load-vs.-friction relation must be calculated, which requires the computation or measurement of several friction forces at different loads. Finally, when the lubricant film (partially) breaks down and direct asperity-asperity contact occurs, linearity is lost and a mere derivation of the friction force with respect to the applied load would lead to a coefficient of friction which is load-dependent and hence no longer a system parameter. However, with the knowledge of the asperity contact area and by using a proper fitting procedure for the proposed three-term kinetic friction law, it is now possible to calculate the load-independent coefficient of friction governing the load-controlled contribution to the friction force in nanosystems.

To estimate the asperity contact area, I developed a computational scheme which allows the mapping of the geometrical configurational data obtained from classical molecular dynamics (MD) simulations to continuum via a simple but powerful smooth particle post-processing approach (SPM). With this method, it is possible to visualize surfaces and interfaces in molecular systems as iso-surfaces of a calculated material density. Furthermore, it can deal with quantities resulting from MD simulations which may be awkward or impossible to handle in a discrete atomistic representation, but can be straightforwardly

treated with the methods of continuum mechanics. This bridging of the gap between simulation methods which are usually confined to specific time and space domains is an important step towards multiscale computational tribology.

I then applied this SPM approach to numerous MD simulations of mixed and boundary-lubricated nanoscale systems, using it to calculate the solid-solid contact area which occurs when the lubricant film breaks down and two opposing asperities touch. The resulting values for this asperity contact area were successfully validated with two other approaches, a contact atom counting procedure and a Voronoi tessellation of the contact zone, which are either less reliable or computationally much more expensive than the SPM approach.

As a tribosystem in the mixed-lubrication regime runs in, which I simulated by repeatedly shearing two lubricated asperities against each other, the amount of direct solid-solid interaction decreases over time, finally leading to the disappearance of the contact-area-dependent contribution to the friction force from the proposed friction law. The subsequent linear load-vs.-friction behavior of the run-in system is described by a two-term friction law, a special case of the proposed one for vanishing contact area called the Derjaguin-form, which still retains the load-independent friction force offset.

To analyze the occurrence and the possible origins of this friction force offset, I carried out a large number of shear simulations with boundary-lubricated tribosystems, i.e., systems without asperity contact during sliding. This case study involved the variation of the boundary lubricant type and coverage as well as the roughness of the solid substrates. Moreover, some systems were simulated which included several layers of a base-oil-type lubricant between the two boundary lubricant films. The addition of the base oil resulted in the vanishing of the load-independent friction force offset, finally leading to the purely load-controlled load-vs.-friction behavior described by the well-known and macroscopically used Amontons-Coulomb friction law.

However, there were various tribosystems in the case study which were not additionally lubricated with a base oil but still had a friction force offset close to zero. So to further analyze the origins of its occurrence, I carefully selected several systems exhibiting high and low friction force offsets. To corroborate the observation that the friction force offset was somehow linked to the degree of disorder within the lubricant, I attempted to quantify this disorder by estimating the lubricant's configurational entropy. The single macromolecule approach, based on covariance (super)matrices of the carbon backbone atoms in the lubricant, yielded the result that a higher friction force offset is reflected in the configurational entropy of those systems in which lubricant disorder is caused by low boundary lubricant coverage, but not in those where it is due to substrate roughness.

Appendix A

LAMMPS Script

In this section I will briefly discuss the entire LAMMPS input script template used for most of the large-asperity shear simulations in this work. In the following, text blocks typeset in `monospace` are actual script code. Within the script, the pound character (`#`) denotes a remark line which is ignored by LAMMPS. Script lines that do not start at the far left are continuations of the previous line due to limited page width. I will print a block of script code first and discuss it directly afterwards. For a full documentation of LAMMPS commands, see the LAMMPS online manual [10].

```
# Shear simulation 4m/s for 2.5 ns
# Tribosystem amorphous Fe + semi-spherical asperity --
# Boundary lubricant: stearic acid (66 molecules/slider)
#
# Atomic Types:
# RCH3 Alkane   CT   type 1
# R2CH2 Alkane  CT   type 2
# HR Alkane     HC   type 3
# COOH CarbAc  C    type 4
# OH CarbAc     OH   type 5
# C=O CarbAc    O    type 6
# COOH CarbAc  HO   type 7
# Fe mobile lo  Fe1  type 8
# Fe fixed lo   Fe2  type 9
# Fe asp lo     Fe3  type 10
# Fe mobile hi  Fe4  type 11
# Fe fixed hi   Fe5  type 12
# Fe asp hi     Fe6  type 13
```

It is usually good practice to have a helpful header including information about the type of simulation and a list defining the used atomic types.

```

# Preamble
units          metal
atom_style     full
lattice        bcc 2.855324
boundary       p p s

```

```

# Read Data File
read_data      data.tribo

```

Here the unit system is set to `metal`, meaning that distances are measured in Ångströms, time in picoseconds and energy in electron volts. The atom style `full` requires every atom in the simulation to be assigned a charge and to be treated molecularly. The lattice is set to the bcc Fe lattice with the lattice constant from the used EAM-FS potential. Finally, the boundary conditions are set to periodic in x and y -direction, and “shrink-wrapped” (see section 1.5) in z -direction.

```

# Interaction Potential Styles
pair_style     hybrid eam/fs lj/cut/coul/cut 10.0 18.0
bond_style     harmonic
angle_style    harmonic
dihedral_style opls

```

```

# EAM/FS Parameters
pair_coeff     * * eam/fs Fe_mm.eam.fs NULL NULL NULL
              NULL NULL NULL NULL Fe Fe Fe Fe Fe Fe

```

```

# OPLS-AA Interatomic Potentials
pair_coeff     1 1 lj/cut/coul/cut 0.002862 3.500000
pair_coeff     2 2 lj/cut/coul/cut 0.002862 3.500000
pair_coeff     3 3 lj/cut/coul/cut 0.001301 2.500000
pair_coeff     4 4 lj/cut/coul/cut 0.004553 3.750000
pair_coeff     5 5 lj/cut/coul/cut 0.007372 3.000000
pair_coeff     6 6 lj/cut/coul/cut 0.009106 2.960000
pair_coeff     7 7 lj/cut/coul/cut 0.000000 0.000000

```

```

# Solid-lubricant Interaction Potentials
pair_coeff     1 8* lj/cut/coul/cut 0.01692 3.15832
pair_coeff     2 8* lj/cut/coul/cut 0.01692 3.15832
pair_coeff     3 8* lj/cut/coul/cut 0.01141 2.66927
pair_coeff     4 8* lj/cut/coul/cut 0.02134 3.26917
pair_coeff     5 8* lj/cut/coul/cut 0.10000 2.92404
pair_coeff     6 8* lj/cut/coul/cut 0.10000 2.90448
pair_coeff     7 8* lj/cut/coul/cut 0.00000 0.00000

```

```
# Special OPLS-AA Settings
special_bonds  0.0 0.0 0.5
pair_modify    shift yes mix geometric
```

The pair style hybrid allows the simultaneous use of the EAM-FS potential for the metal sliders together with the Lennard-Jones and Coulomb potential required for the molecules. Then all homogeneous and mixed LJ-parameters are set. Finally, the intermolecular potentials are configured to OPLS-AA standard.

```
# Particle Group Definitions
group lofix type 9
group loslab type 8
group islands type 10 13
group hifix type 12
group hislab type 11
group fixed union lofix hifix
group tstat union loslab hislab islands
group mobile subtract all fixed
group allup subtract all lofix
```

Define various groups of atoms. Some of these will be used to configure external constraints, the thermostat, or simply some output commands.

```
# Thermostatting Computations
compute tstat1d tstat temp/partial 0 1 0
compute mob1d  mobile temp/partial 0 1 0
```

```
# Reaction Force Computation
compute F_r allup group/group lofix
```

The first block configures the thermostat so it only interferes with the *y*-component of the atom velocity. The second block sets the groups of atoms between which the friction force and the load will be computed.

```
# Neighbor List Options
neighbor      2.0 bin
neigh_modify  delay 5 one 4000
```

```
# Time Step and rRESPA-Integrator
timestep      0.002
run_style     respa 3 2 2 bond 1 angle 2 pair 3
```

```

# Thermodynamic Output Style
thermo_style    multi
thermo          50
thermo_modify   temp mobld flush yes

```

The neighbor list must be made slightly bigger to accommodate more atoms for high-load shear simulations. Next, the top-level time step is set, and the rRESPA algorithm is configured to three time step levels, each a factor 2 apart. Finally, thermodynamic output is set to include the partial energies of the internal molecular degrees of freedom, write every 50 time steps, and calculate the temperature from the y -component of the atom velocity only.

```

# Initialization
fix              1 all nve
fix              2 lofix setforce 0.0 0.0 0.0
fix              2b hifix setforce 0.0 0.0 0.0

```

```

# Langevin Thermostatting
fix              3 tstat langevin 300.0 300.0 0.5 699483
fix_modify      3 temp tstatld

```

The integrating scheme and the Langevin thermostat are chosen and configured. In LAMMPS, the Langevin thermostat must be coupled with the NVE ensemble to function correctly. The `setforce` command makes the outermost slider atoms rigid. The number 699483 is the seed for the uniform random number generator.

```

# Time Averages of Reaction Forces
fix      forces      all ave/time 1 50 50 c_F_r[1] c_F_r[2] c_F_r[3]
                                                file avg.forces_all

```

```

# Dumps (Configuration Snapshots)
dump     1  all custom 250 dump.tribo.gz tag mol type q x y z
dump     2  all custom 10000 dump.overview.gz tag mol type q x y z vx vy vz

```

The averaging and output options for the reaction forces are set, and two separate files with system configurations (“snapshots”) are written. One every 0.5 ps for in-depth analysis, and one every 20 ps for quick overviews and visualization.

```

# Constant Slider Separation for 1250 Steps
velocity      hifix set 0.0 0.0 0.0 sum no units box
run 1250

```

```

# Apply Load: 1.6 GPa = 44.08 nN

```

```

velocity      hifix set 0.0 0.0 NULL sum no units box
unfix        2b
fix          2b hifix setforce 0.0 0.0 NULL
fix          4 hifix aveforce NULL NULL -0.04096358209

```

The slider separation is kept constant for 2.5 ps, then the load is applied in $-z$ -direction as a per-atom force in eV/Å.

```

# Ramp Velocity to 4m/s in 9750 Time Steps
velocity hifix set 0.001 0.0 NULL sum no units box
run 250
velocity hifix set 0.002 0.0 NULL sum no units box
run 250
# .
# .
# .
velocity hifix set 0.038 0.0 NULL sum no units box
run 250
velocity hifix set 0.039 0.0 NULL sum no units box
run 250

# Shear at 4m/s
velocity hifix set 0.04 0.0 NULL sum no units box
run 1239000

```

The sliding velocity is ramped to 4 m/s in steps of 0.1 m/s over 20 ps, then it is kept constant for the rest of the total simulation time of 2.5 ns. The vertical ellipsis denotes that several similar blocks of code have been omitted.

Appendix B

Potential Parameters

The following tables list the potential parameters used throughout this work. The values in tables B.1–B.4 are taken from the OPLS-AA force field discussed in section 1.2.3 and gathered via private communication with W. Jorgensen, M. Chandross, C. D. Lorenz, and L.-T. Kong, while the solid-lubricant interaction parameters in table B.5 were obtained using the procedure from section 2.1.2. One- or two-letter abbreviations in parentheses introduced in table B.1 are used throughout tables B.2, B.3, and B.4. Atoms which share the same abbreviation may have different non-bonded parameters but behave identically with respect to all bonded potentials. Further information on the OPLS-AA force field can be found in [135] and the references therein.

In all tables, the first block lists the parameters required for modeling saturated carboxylic acids such as stearic acid. In the second block, additional parameters for also including the double bonds occurring in unsaturated carboxylic acids such as oleic acid can be found. The third block adds parameters needed for modeling the methyl group in methyl esters such as methyl stearate.

atom, group (abbreviation)	q [e^-]	σ [\AA]	ε [eV]	m [a.m.u.]
C, alkane: R-CH ₃ (CT)	-0.18	3.50	0.002862	12.000
C, alkane: R-CH ₂ -R' (CT)	-0.12	3.50	0.002862	12.000
H, alkane (HC)	0.06	2.50	0.001301	1.008
C, carboxyl (C)	0.52	3.75	0.004553	12.000
O(H), carboxyl (OH)	-0.53	3.00	0.007372	15.999
O(C), carboxyl (O)	-0.44	2.96	0.009106	15.999
H(O), carboxyl (HO)	0.45	0.00	0.000000	1.008
C, alkene (CM)	-0.12	3.55	0.003296	12.000
H, alkene (HC)	0.12	2.42	0.001301	1.008
C, carbonyl (C)	0.51	3.75	0.004553	12.000
O(R), ester (OR)	-0.33	3.00	0.007372	15.999
O(C), carbonyl (O)	-0.43	2.96	0.009106	15.999
C, methoxy (CT)	0.16	3.50	0.002862	12.000
H, alkoxy (HC)	0.03	2.42	0.000651	1.008

Table B.1: Non-bonded potential parameters.

bond	K_r [eV]	r_0 [\AA]
CT-CT	11.622	1.529
CT-HC	14.744	1.090
CT-C	13.746	1.522
C=O	24.718	1.229
C-OH	19.514	1.364
OH-HO	23.980	0.945
CM-CM	23.807	1.340
CM-CT	13.746	1.510
CM-HC	14.744	1.080
C-CT	13.746	1.522
CT-OR	13.877	1.410
C-OR	9.280	1.327

Table B.2: Bond stretching parameters.

angle	K_θ [eV]	θ_0 [°]
CT-CT-CT	2.5302	112.7
CT-CT-HC	1.6262	110.7
HC-CT-HC	1.4310	107.8
CT-CT-C	2.7319	111.1
HC-CT-C	1.5177	109.5
CT-C=O	3.4691	120.4
CT-C-OH	3.0355	108.0
O=C-OH	3.4691	121.0
C-OH-HO	1.5177	113.0
CT-CM-HC	1.5177	117.0
CM-CT-CT	2.7319	111.1
CM-CT-HC	1.5177	109.5
CM-CM-CT	3.0355	124.0
CM-CM-HC	1.5177	120.0
CT-OR-C	3.5992	116.9
HC-CT-OR	1.5177	109.5
CT-C-OR	3.5125	111.4
OR-C=O	3.5992	123.4

Table B.3: Angle bending parameters.

dihedral	V_1 [eV]	V_2 [eV]	V_3 [eV]
CT-CT-CT-CT	0.056373	-0.002168	0.008673
HC-CT-CT-CT	0	0	0.013009
HC-CT-CT-HC	0	0	0.013009
CT-CT-CT-C	-0.073589	-0.019774	0.025368
HC-CT-CT-C	0	0	-0.003296
CT-C-OH-HO	0	0.209449	0
O=C-OH-HO	0	0.209449	0
CM-CT-CT-CT	+0.056373	-0.002168	+0.008673
CM-CM-CT-CT	+0.015004	+0.017563	-0.039201
CT-CM-CM-CT	0	+0.607097	0
CT-CM-CM-HC	0	+0.607097	0
HC-CM-CM-HC	0	+0.607097	0
HC-CT-CM-CM	0	0	-0.016131
HC-CM-CT-HC	0	0	+0.013790
HC-CM-CT-CT	0	0	+0.013790
HC-CT-CT-CM	0	0	+0.015871
CT-CT-C-OH	0	0	-0.023980
HC-CT-C-OH	0	0	+0.005724
CT-C-OR-CT	+0.202467	+0.222198	0
O=C-OR-CT	0	+0.222198	0
C-OR-CT-HC	0	0	+0.008586

Table B.4: Dihedral potential coefficients.

lubricant-solid	σ_{ij} [Å]	ε_{ij} [eV]
CT-Fe	3.16	0.01692
HC-Fe	2.67	0.01141
C-Fe	3.27	0.02134
OH-Fe	2.92	0.10000
O-Fe	2.90	0.10000
HO-Fe	0.00	0.00000
CM-Fe	3.18	0.01815
HC _{alkene} -Fe	2.63	0.01141
CT _{methoxy} -Fe	3.16	0.01692
HC _{alkoxy} -Fe	2.63	0.00807

Table B.5: Mixed LJ-parameters for lubricant-solid interactions.

Appendix C

Best-Fit Parameters

The following tables give a complete account of the calculated best-fit parameters and their respective estimated errors for the systems discussed in section 4.3, grouped by lubricant. The parameters were obtained from the χ^2 -fitting procedure applied to Eq. (3.16), and in the tables n_{data} denotes the number of data points entering the fitting procedure. The used system ID abbreviations are explained in table 4.2.

system ID	F_0 [nN]	ΔF_0 [nN]	μ	$\Delta\mu$	n_{data}
SteAc-5x7-0ML	0.553	0.058	0.149	0.005	5
SteAc-5x7-1ML	0.561	0.037	0.148	0.003	5
SteAc-5x7-2ML	0.603	0.022	0.155	0.002	5
SteAc-5x7-3ML	0.608	0.076	0.161	0.007	5
SteAc-5x7-4ML	0.610	0.140	0.154	0.012	5
SteAc-5x7-amo	0.645	0.017	0.140	0.002	5
SteAc-6x7-1ML	0.479	0.109	0.161	0.009	3
SteAc-6x7-2ML	0.522	0.074	0.172	0.007	3
SteAc-6x7-3ML	0.537	0.110	0.182	0.011	3
SteAc-6x7-4ML	0.531	0.017	0.159	0.002	3
SteAc-6x7-amo	0.484	0.082	0.136	0.007	3
SteAc-6x8-0ML	0.392	0.110	0.142	0.010	5
SteAc-6x8-1ML	0.435	0.057	0.152	0.005	5
SteAc-6x8-2ML	0.399	0.114	0.165	0.010	5
SteAc-6x8-3ML	0.557	0.052	0.159	0.005	5
SteAc-6x8-4ML	0.412	0.051	0.195	0.004	5
SteAc-6x8-amo	0.239	0.047	0.158	0.004	5
SteAc-7x8-1ML	0.119	0.027	0.055	0.003	3
SteAc-7x8-2ML	0.343	0.022	0.135	0.002	3
SteAc-7x8-3ML	0.396	0.019	0.176	0.002	3
SteAc-7x8-4ML	0.427	0.050	0.154	0.004	5
SteAc-7x8-amo	0.045	0.051	0.059	0.004	5
SteAc-7x9-0ML	0.084	0.128	0.077	0.011	5
SteAc-7x9-1ML	0.249	0.033	0.094	0.003	5
SteAc-7x9-2ML	0.255	0.026	0.124	0.002	5
SteAc-7x9-3ML	0.397	0.111	0.131	0.010	5
SteAc-7x9-4ML	0.413	0.021	0.159	0.002	5
SteAc-7x9-amo	0.374	0.118	0.085	0.010	5

Table C.1: Constitutive system parameters for stearic acid.

system ID	F_0 [nN]	ΔF_0 [nN]	μ	$\Delta\mu$	n_{data}
OleAc-5x7-1ML	0.498	0.049	0.158	0.005	3
OleAc-5x7-2ML	0.521	0.068	0.170	0.008	6
OleAc-5x7-3ML	0.581	0.064	0.138	0.006	3
OleAc-5x7-4ML	0.490	0.041	0.159	0.005	6
OleAc-5x7-amo	0.579	0.050	0.161	0.006	6
OleAc-6x7-1ML	0.521	0.020	0.183	0.002	3
OleAc-6x7-2ML	0.518	0.009	0.179	0.001	3
OleAc-6x7-3ML	0.632	0.185	0.165	0.020	3
OleAc-6x7-4ML	0.476	0.036	0.184	0.003	3
OleAc-6x7-amo	0.606	0.119	0.160	0.013	3
OleAc-6x8-1ML	0.501	0.120	0.182	0.011	3
OleAc-6x8-2ML	0.580	0.058	0.178	0.007	6
OleAc-6x8-3ML	0.578	0.002	0.177	0.000	3
OleAc-6x8-4ML	0.596	0.082	0.178	0.009	6
OleAc-6x8-amo	0.617	0.075	0.171	0.008	6
OleAc-7x8-1ML	0.218	0.016	0.189	0.002	3
OleAc-7x8-2ML	0.270	0.022	0.174	0.002	3
OleAc-7x8-3ML	0.337	0.029	0.194	0.003	3
OleAc-7x8-4ML	0.329	0.022	0.169	0.002	3
OleAc-7x8-amo	-0.041	0.006	0.165	0.001	3
OleAc-7x9-1ML	0.009	0.128	0.137	0.016	3
OleAc-7x9-2ML	0.036	0.072	0.145	0.008	6
OleAc-7x9-3ML	0.152	0.150	0.125	0.015	3
OleAc-7x9-4ML	0.465	0.026	0.157	0.002	6
OleAc-7x9-amo	-0.077	0.033	0.140	0.005	6

Table C.2: Constitutive system parameters for oleic acid.

system ID	F_0 [nN]	ΔF_0 [nN]	μ	$\Delta\mu$	n_{data}
MeSte-5x7-1ML	0.628	0.136	0.153	0.014	3
MeSte-5x7-2ML	0.569	0.112	0.148	0.012	6
MeSte-5x7-3ML	0.559	0.099	0.155	0.010	3
MeSte-5x7-4ML	0.550	0.069	0.147	0.008	6
MeSte-5x7-amo	0.417	0.041	0.157	0.004	3
MeSte-6x7-1ML	0.476	0.101	0.168	0.009	3
MeSte-6x7-2ML	0.509	0.124	0.159	0.011	3
MeSte-6x7-3ML	0.491	0.043	0.164	0.004	3
MeSte-6x7-4ML	0.526	0.015	0.174	0.002	3
MeSte-6x7-amo	0.331	0.067	0.169	0.006	3
MeSte-6x8-1ML	0.243	0.045	0.148	0.005	3
MeSte-6x8-2ML	0.288	0.050	0.153	0.005	6
MeSte-6x8-3ML	0.362	0.005	0.174	0.001	3
MeSte-6x8-4ML	0.597	0.073	0.169	0.008	6
MeSte-6x8-amo	0.246	0.007	0.129	0.001	3
MeSte-7x8-1ML	0.122	0.069	0.150	0.006	3
MeSte-7x8-2ML	0.307	0.035	0.138	0.003	3
MeSte-7x8-3ML	0.299	0.092	0.155	0.009	3
MeSte-7x8-4ML	0.577	0.059	0.156	0.006	3
MeSte-7x8-amo	0.388	0.082	0.099	0.008	3
MeSte-7x9-1ML	0.323	0.058	0.121	0.006	3
MeSte-7x9-2ML	0.403	0.059	0.142	0.006	6
MeSte-7x9-3ML	0.392	0.137	0.158	0.013	3
MeSte-7x9-4ML	0.540	0.093	0.181	0.009	6
MeSte-7x9-amo	0.421	0.069	0.131	0.006	3

Table C.3: Constitutive system parameters for methyl stearate.

system ID	F_0 [nN]	ΔF_0 [nN]	μ	$\Delta\mu$	n_{data}
Hex-5x7-1ML	0.031	0.018	0.112	0.002	3
Hex-5x7-2ML	0.064	0.004	0.117	0.000	3
Hex-5x7-3ML	0.093	0.016	0.111	0.002	3
Hex-5x7-4ML	0.093	0.071	0.088	0.006	5
Hex-5x7-amo	0.010	0.048	0.103	0.004	5
Hex-6x7-1ML	0.092	0.075	0.105	0.007	3
Hex-6x7-2ML	0.013	0.003	0.106	0.000	3
Hex-6x7-3ML	0.141	0.029	0.094	0.002	3
Hex-6x7-4ML	0.077	0.021	0.110	0.002	3
Hex-6x7-amo	0.003	0.132	0.101	0.015	3
Hex-6x8-1ML	-0.055	0.047	0.123	0.006	3
Hex-6x8-2ML	0.037	0.063	0.105	0.007	3
Hex-6x8-3ML	0.079	0.030	0.099	0.003	3
Hex-6x8-4ML	0.038	0.031	0.110	0.004	6
Hex-6x8-amo	-0.013	0.032	0.111	0.004	6
Hex-7x8-1ML	-0.041	0.069	0.100	0.008	3
Hex-7x8-2ML	0.060	0.023	0.095	0.003	3
Hex-7x8-3ML	0.002	0.152	0.104	0.017	3
Hex-7x8-4ML	0.028	0.029	0.106	0.003	3
Hex-7x8-amo	0.033	0.036	0.073	0.004	3
Hex-7x9-0ML	-0.035	0.054	0.067	0.005	5
Hex-7x9-1ML	-0.034	0.076	0.100	0.008	3
Hex-7x9-2ML	0.074	0.079	0.100	0.007	3
Hex-7x9-3ML	-0.009	0.016	0.108	0.002	3
Hex-7x9-4ML	0.008	0.027	0.106	0.003	5

Table C.4: Constitutive system parameters for stearic acid with n -hexadecane.

List of Figures

1.1	Lennard-Jones potential.	8
1.2	Bond stretching, angle bending, and bond torsion parameters.	9
1.3	Several OPLS-AA torsional potentials.	11
2.1	Amorphization of a bcc Fe crystal.	20
2.2	Three large asperity types.	22
2.3	Small substrates.	22
2.4	<i>n</i> -hexadecane.	23
2.5	Stearic acid.	24
2.6	Oleic acid.	24
2.7	Stearic acid methyl ester (methyl stearate).	25
2.8	Equilibration of a boundary layer (small slider).	26
2.9	Development of the molecular tilt angle.	28
2.10	Equilibration of a boundary layer (large slider).	28
2.11	Desorbed lubricant molecules.	29
2.12	Compression of a semi-spherical asperity system.	30
2.13	Compression curves.	31
2.14	Compression and equilibration of an oleic acid system.	32
3.1	From MD to continuum with SPM.	36
3.2	Effect of smearing.	38
3.3	Calculation of the asperity contact area $A_{\text{asp}}(L)$	40
3.4	Material transfer in the truncated cone asperity system.	42
3.5	Directional material transfer balance.	43
3.6	Number of contact atoms.	44
3.7	Validation of SPM with the contact atom counting procedure.	45
3.8	Validation of SPM with Voronoi tessellation.	48
3.9	Visualization of plastic and elastic deformation.	49
3.10	Standard deviation of the contact force versus smoothing.	52
3.11	Justification for the statistical inefficiency approximation.	53
3.12	Convergence of the chi-square fitting procedure.	59
4.1	Snapshots of three MD-nanosystems.	68
4.2	Friction force as a function of time.	69

4.3	Time evolution of the semi-spherical asperity system at three different loads.	70
4.4	Time evolution of three different asperity systems at a given load.	71
4.5	Asperity contact area as a function of time.	72
4.6	Total cavity volume of three nanotribological systems.	73
4.7	Load-vs.-friction behavior of three nanotribological systems with asperities.	75
4.8	Load-vs.-friction behavior of a nanotribological systems without asperities.	77
4.9	Side views of the semi-spherical and the slanted pyramid systems.	79
4.10	Time evolution of the semi-spherical asperity system at a given load. . . .	80
4.11	Time evolution of the slanted pyramid asperity system at a given load. . .	81
4.12	Moment of asperity contact onset as a function of the pass number.	82
4.13	Average asperity contact area and contact duration per pass.	82
4.14	Maps for the semi-spherical asperity.	83
4.15	Maps for the slanted pyramid asperity.	84
4.16	Total Fe surface area compared to the “virtual asperity surface area”. . . .	85
4.17	Time development of the slanted pyramid asperity.	87
4.18	Load-vs.-friction for the semi-spherical and slanted pyramid asperity systems.	89
4.19	Three practical fitting procedure indicators.	90
4.20	Run-in system parameters.	91
4.21	Six MD-nanosystem setups.	94
4.22	Friction force as a function of time.	95
4.23	Load-vs.-friction curves for various nano-tribosystems.	96
4.24	Boundary lubricant coverage dependence of the Derjaguin-offset.	99
4.25	Boundary lubricant coverage dependence of the coefficient of friction. . . .	100
4.26	Nano-roughness dependence of the Derjaguin-offset.	101
4.27	Nano-roughness dependence of the coefficient of friction.	102
4.28	Load-vs.-friction behavior of nine selected nanotribological systems.	103
4.29	SPM-visualizations of nine selected systems.	105
4.30	Constitutive system parameters for the linear load-vs.-friction behavior. . .	106
4.31	Maps of the covariance (super)matrices of three nanotribological systems. .	107
4.32	Histograms of eigenvector components.	108
4.33	Molar per-atom contributions to the entropy.	110

List of Tables

4.1	Constitutive system parameters depending on asperity geometry.	76
4.2	Key to the used abbreviations.	97
4.3	The nine systems selected for further analysis.	104
B.1	Non-bonded potential parameters.	120
B.2	Bond stretching parameters.	120
B.3	Angle bending parameters.	121
B.4	Dihedral potential coefficients.	122
B.5	Mixed LJ-parameters for lubricant-solid interactions.	122
C.1	Constitutive system parameters for stearic acid.	124
C.2	Constitutive system parameters for oleic acid.	125
C.3	Constitutive system parameters for methyl stearate.	126
C.4	Constitutive system parameters for stearic acid with <i>n</i> -hexadecane.	127

Bibliography

- [1] B. Bhushan, editor. *Nanotribology And Nanomechanics: An Introduction*. Springer, 2005.
- [2] M. Müser. Atomistic simulations of solid friction. In P. Nielaba, M. Mareschal, and G. Ciccotti, editors, *Bridging Time Scales: Molecular Simulations for the Next Decade*, volume 605 of *Lecture Notes in Physics*, pages 289–317. Springer Berlin / Heidelberg, 2002.
- [3] U. Landman. Materials by numbers: computations as tools of discovery. *Proc. Natl. Acad. Sci. U.S.A.*, 102(19):6671–6678, 2005.
- [4] B. Alder and T. Wainwright. Phase transition for a hard sphere system. *J. Chem. Phys.*, 27 (5):1208, 1957.
- [5] U. Landman, W. D. Luedtke, and M. W. Ribarsky. Structural and dynamical consequences of interactions in interfacial systems. *Journal of Vacuum Science & Technology A: Vacuum, Surfaces, and Films*, 7(4):2829–2839, 1989.
- [6] P. A. Thompson and M. O. Robbins. Simulations of contact-line motion: Slip and the dynamic contact angle. *Phys. Rev. Lett.*, 63(7):766–769, Aug 1989.
- [7] M. O. Robbins and M. H. Müser. Computer simulations of friction, lubrication and wear. In B. Bhushan, editor, *Modern Tribology Handbook*, pages 717–765. CRC Press, Boca Raton, 2001.
- [8] S. Heo, S. B. Sinnott, D. W. Brenner, and J. A. Harrison. Computational modeling of nanometer-scale tribology. In B. Bhushan, editor, *Nanotribology and Nanomechanics*, pages 623–691. Springer Berlin Heidelberg, 2005.
- [9] J. D. Schall, P. T. Mikulski, G. M. Chateauneuf, G. Gao, and J. A. Harrison. Molecular dynamics simulations of tribology. In *Superlubricity*, pages 79–102. Elsevier, Amsterdam, 2007.
- [10] LAMMPS. <http://lammps.sandia.gov/>
- [11] GROMACS. <http://www.gromacs.org/>

- [12] Moldy. <http://www.ccp5.ac.uk/moldy/moldy.html>
- [13] NAMD. <http://www.ks.uiuc.edu/research/namd/>
- [14] P. A. Thompson, G. S. Grest, and M. O. Robbins. Phase transitions and universal dynamics in confined films. *Phys. Rev. Lett.*, 68(23):3448–3451, 1992.
- [15] C. Baig, B. J. Edwards, D. J. Keffer, and H. D. Cochran. Rheological and structural studies of liquid decane, hexadecane, and tetracosane under planar elongational flow using nonequilibrium molecular-dynamics simulations. *The Journal of Chemical Physics*, 122(18):184906, 2005.
- [16] A. Jabbarzadeh, P. Harrowell, and R. Tanner. The structural origin of the complex rheology in thin dodecane films: Three routes to low friction. *Tribology International*, 40(10-12):1574–1586, 2007. Tribology at the Interface: Proceedings of the 33rd Leeds-Lyon Symposium on Tribology (Leeds, 2006).
- [17] S. Eder, G. Vorlaufer, S. Ilincic, and G. Betz. Simulation of wear processes using molecular dynamics (MD) simulations. *OeTG Symposium (St. Pölten)*, Conference Proceedings:105–112, 2007.
- [18] K. J. Tupper and D. W. Brenner. Molecular dynamics simulations of friction in self-assembled monolayers. *Thin Solid Films*, 253(1-2):185–189, 1994.
- [19] M. Greenfield and H. Ohtani. Molecular dynamics simulation study of model friction modifier additives confined between two surfaces. *Tribology Letters*, 7(2):137–145, 1999.
- [20] C. D. Lorenz, M. Chandross, G. S. Grest, M. J. Stevens, and E. B. Webb. Tribological properties of alkylsilane self-assembled monolayers. *Langmuir*, 21(25):11744–11748, 2005.
- [21] K. J. Tupper, R. J. Colton, and D. W. Brenner. Simulations of self-assembled monolayers under compression: Effect of surface asperities. *Langmuir*, 10(7):2041–2043, 1994.
- [22] T. Ohzono and M. Fujihira. Molecular dynamics simulations of friction between an ordered organic monolayer and a rigid slider with an atomic-scale protuberance. *Phys. Rev. B*, 62(24):17055–17071, 2000.
- [23] M. A. Moller, D. J. Tildesley, K. S. Kim, and N. Quirke. Molecular dynamics simulation of a Langmuir–Blodgett film. *The Journal of Chemical Physics*, 94(12):8390–8401, 1991.
- [24] P. T. Mikulski and J. A. Harrison. Packing-density effects on the friction of *n*-alkane monolayers. *Journal of the American Chemical Society*, 123(28):6873–6881, 2001.

- [25] S. Eder, G. Vorlaufer, and G. Betz. Computational nanotribology of lubricated model friction contacts. *35th Leeds-Lyon Symposium on Tribology*, Book of Abstracts, XXIV (iii), 2008.
- [26] S. Eder, G. Vorlaufer, F. Franek, and G. Betz. Molecular dynamics simulations of the tribological performance of model lubricant additives. *World Tribology Congress 2009—WTC IV (Kyoto)*, Conference Proceedings, 623, 2009.
- [27] S. Ilincic, S. Eder, G. Vorlaufer, A. Vernes, and N. Tungkunagorn. Modelling load and friction in rough tribocontacts using boundary elements and molecular dynamics. *OeTG Symposium*, 189, 2009.
- [28] G. Amontons. *Mémoires de l'Académie Royale*, page 257, 1699.
- [29] C. A. Coulomb. *Mém. Math. Phys. (Paris)*, page 161, 1785.
- [30] B. Derjaguin. Molekulartheorie der äußeren Reibung. *Zeitschrift für Physik A*, 88:661, 1934.
- [31] J. Gao, W. D. Luedtke, and U. Landman. Nano-elastohydrodynamics: Structure, dynamics, and flow in nonuniform lubricated junctions. *Science*, 270:605–608, 1995.
- [32] S. Eder, G. Vorlaufer, and G. Betz. Molecular dynamics simulations of boundary lubricant failure. *Advances in Boundary Lubrication and Boundary Surface Films*, Book of Abstracts, 41, 2009.
- [33] S. Eder, G. Vorlaufer, A. Pauschitz, and G. Betz. Detailed study of additivated nanotribological contacts using molecular dynamics simulations. *36th Leeds-Lyon Symposium on Tribology*, Book of Abstracts, IV (iii), 2009.
- [34] S. Eder, G. Vorlaufer, A. Vernes, and G. Betz. Identification and analysis of friction regimes due to the failure of thin lubricant films. *Theoretical Modeling and Experimental Simulation in Tribology*, Program Booklet, 57, 2010.
- [35] H. J. C. Berendsen. *Simulating the Physical World*. Cambridge University Press, 2007.
- [36] W. G. Hoover. *Smooth Particle Applied Mechanics: The State of the Art*. World Scientific, Singapore, 2006.
- [37] F. P. Bowden and D. Tabor. *The Friction and Lubrication of Solids*. Oxford University Press, Oxford, 1950.
- [38] S. Eder, A. Vernes, G. Vorlaufer, and G. Betz. Molecular dynamics simulations of mixed lubrication with smooth particle post-processing. *J. Phys.: Condens. Matter*, 23:175004, 2011.

- [39] S. Eder, A. Vernes, G. Vorlaufer, and G. Betz. A post-processing tool for mapping molecular dynamics to continuum. *38th Leeds-Lyon Symposium on Tribology*, Book of Abstracts, XXX (ii), 2011.
- [40] A. Vernes, S. Eder, G. Vorlaufer, and G. Betz. On the three-term kinetic friction law in nanotribological systems. *Faraday Discuss.* 156, 2012. DOI:10.1039/C2FD00120A
- [41] S. Eder, S. Ilincic, and G. Vorlaufer. Numerical modelling of lubricated frictional tribocontacts on the micro- and nanoscale. *17th International Colloquium Tribology—TAE (Ostfildern)*, Conference Proceedings, 10, 2010.
- [42] I. Szlufarska, M. Chandross, and R. W. Carpick. Recent advances in single-asperity nanotribology. *Journal of Physics D: Applied Physics*, 41(12):123001 (39pp), 2008.
- [43] J. Gibson, A. Goland, M. Milgram, and G. Vineyard. Dynamics of radiation damage. *Phys. Rev.*, 120:1229, 1960.
- [44] A. Rahman. Correlations in the motion of atoms in liquid argon. *Phys. Rev.*, 136(2A):A405–A411, 1964.
- [45] L. Verlet. Computer “experiments” on classical fluids. I. Thermodynamical properties of Lennard-Jones molecules. *Phys. Rev.*, 159(1):98, 1967.
- [46] M. Allen and D. Tildesley. *Computer Simulation of Liquids*. Oxford University Press, Oxford, 1987.
- [47] J. M. Haile. *Molecular Dynamics Simulation: Elementary Methods*. Wiley, March 1997.
- [48] D. Frenkel and B. Smit. *Understanding Molecular Simulation: From Algorithms to Applications*. Academic Press, 2002.
- [49] D. C. Rapaport. *The Art of Molecular Dynamics Simulation*. Cambridge University Press, 2004.
- [50] M. Griebel, S. Knappek, and G. Zumbusch. *Numerical Simulation in Molecular Dynamics: Numerics, Algorithms, Parallelization, Applications*. Springer Publishing Company, Incorporated, 1st edition, 2007.
- [51] J. E. Lennard-Jones. Cohesion. *Proc. Phys. Soc.*, 43:461, 1931.
- [52] M. S. Daw and M. I. Baskes. Embedded-atom method: Derivation and application to impurities, surfaces, and other defects in metals. *Phys. Rev. B*, 29(12):6443–6453, 1984.

- [53] M. W. Finnis and J. E. Sinclair. A simple empirical n-body potential for transition metals. *Philosophical Magazine A*, 50(1):45–55, 1984.
- [54] F. Ercolessi, M. Parrinello, and E. Tosatti. Simulation of gold in the glue model. *Philosophical Magazine A*, 58(1):213–226, 1988.
- [55] F. Ercolessi. A molecular dynamics primer. Spring College in Computational Physics, ICTP, Trieste, <http://www.fisica.uniud.it/ercolessi/md/md/>, 1997.
- [56] W. D. Cornell, P. Cieplak, C. I. Bayly, I. R. Gould, K. M. Merz, D. M. Ferguson, D. C. Spellmeyer, T. Fox, J. W. Caldwell, and P. A. Kollman. A second generation force field for the simulation of proteins, nucleic acids, and organic molecules. *J. Am. Chem. Soc.*, 117(19):5179–5197, 1995.
- [57] A. D. MacKerell, D. Bashford, Bellott, R. L. Dunbrack, J. D. Evanseck, M. J. Field, S. Fischer, J. Gao, H. Guo, S. Ha, D. Joseph-McCarthy, L. Kuchnir, K. Kuczera, F. T. K. Lau, C. Mattos, S. Michnick, T. Ngo, D. T. Nguyen, B. Prodhom, W. E. Reiher, B. Roux, M. Schlenkrich, J. C. Smith, R. Stote, J. Straub, M. Watanabe, J. Wirkiewicz-Kuczera, D. Yin, and M. Karplus. All-atom empirical potential for molecular modeling and dynamics studies of proteins. *J. Phys. Chem. B*, 102(18):3586–3616, 1998.
- [58] W. L. Jorgensen, D. S. Maxwell, and J. Tirado-Rives. Development and testing of the OPLS All-Atom force field on conformational energetics and properties of organic liquids. *Journal of the American Chemical Society*, 118(45):11225–11236, 1996.
- [59] D. W. Brenner, O. A. Shenderova, J. A. Harrison, S. J. Stuart, B. Ni, and S. B. Sinnott. A second-generation reactive empirical bond order (REBO) potential energy expression for hydrocarbons. *Journal of Physics: Condensed Matter*, 14(4):783–802, 2002.
- [60] S. J. Stuart, A. B. Tutein, and J. A. Harrison. A reactive potential for hydrocarbons with intermolecular interactions. *The Journal of Chemical Physics*, 112(14):6472–6486, 2000.
- [61] K. Chenoweth, A. C. T. van Duin, and W. A. Goddard. ReaxFF reactive force field for molecular dynamics simulations of hydrocarbon oxidation. *J. Phys. Chem. A*, 112(5):1040–1053, 2008.
- [62] W. L. Jorgensen, J. D. Madura, and C. J. Swenson. Optimized intermolecular potential functions for liquid hydrocarbons. *Journal of the American Chemical Society*, 106(22):6638–6646, 1984.

- [63] E. K. Watkins and W. L. Jorgensen. Perfluoroalkanes: Conformational analysis and liquid-state properties from ab initio and Monte Carlo calculations. *The Journal of Physical Chemistry A*, 105(16):4118–4125, 2001.
- [64] C. Størmer. Méthode d'intégration numérique des équations différentielles ordinaires. *C.R. Congress Internat. Strassbourg 1920*, 243–257, 1921.
- [65] J. B. Delambre. *De l'usage du calcul différentiel dans la construction des tables astronomiques*. 1790.
- [66] M. Tuckerman, B. J. Berne, and G. J. Martyna. Reversible multiple time scale molecular dynamics. *The Journal of Chemical Physics*, 97(3):1990–2001, 1992.
- [67] H. F. Trotter. On the product of semi-groups of operators. *Proc. Am. Math. Soc.*, 10:545, 1959.
- [68] S. S. Sarman, D. J. Evans, and P. T. Cummings. Recent developments in non-Newtonian molecular dynamics. *Physics Reports*, 305:1–92, 1998.
- [69] H. J. C. Berendsen, J. P. M. Postma, W. F. van Gunsteren, A. DiNola, and J. R. Haak. Molecular dynamics with coupling to an external bath. *The Journal of Chemical Physics*, 81(8):3684–3690, 1984.
- [70] S. Nosé. A molecular dynamics method for simulations in the canonical ensemble. *Molecular Physics*, 52(2):255–268, 1984.
- [71] W. G. Hoover. Canonical dynamics: Equilibrium phase-space distributions. *Phys. Rev. A*, 31(3):1695–1697, 1985.
- [72] T. Schneider and E. Stoll. Molecular-dynamics study of a three-dimensional one-component model for distortive phase transitions. *Physical Review B*, 17(3):1302–1322, 1978.
- [73] B. Dünweg and W. Paul. Brownian dynamics simulations without Gaussian random numbers. *Int. J. Mod. Phys. C*, 2:817, 1991.
- [74] S. J. Plimpton. Fast parallel algorithms for short-range molecular dynamics. *J. Comput. Phys.*, 117:1, 1995.
- [75] VMD. <http://www.ks.uiuc.edu/research/vmd/>
- [76] M. I. Mendeleev, S. Han, D. J. Srolovitz, G. J. Ackland, D. Y. Sun, and M. Asta. Development of new interatomic potentials appropriate for crystalline and liquid iron. *Philosophical Magazine*, 83:3977–3994, 2003.
- [77] P. Maranian. *Reducing Brittle and Fatigue Failures in Steel Structures*. American Society of Civil Engineers, 2010.

- [78] B. Park, C. D. Lorenz, M. Chandross, M. J. Stevens, G. S. Grest, and O. A. Borodin. Frictional dynamics of fluorine-terminated alkanethiol self-assembled monolayers. *Langmuir*, 20(23):10007–10014, 2004.
- [79] C. Lorenz, E. Webb, M. Stevens, M. Chandross, and G. Grest. Frictional dynamics of perfluorinated self-assembled monolayers on amorphous SiO₂. *Tribology Letters*, 19(2):93–98, June 2005.
- [80] M. Chandross, C. D. Lorenz, M. J. Stevens, and G. S. Grest. Simulations of nanotribology with realistic probe tip models. *Langmuir*, 24(4):1240–1246, 2008.
- [81] L.-T. Kong, C. Denniston, M. Müser, and Y. Qi. Non-bonded force field for the interaction between metals and organic molecules: a case study of olefins on aluminum. *Phys. Chem. Chem. Phys.*, 11:10195, 2009.
- [82] L. Kantorovich. Generalized Langevin equation for solids. I. Rigorous derivation and main properties. *Physical Review B*, 78(9):094304, 2008.
- [83] L. Kantorovich and N. Rompotis. Generalized Langevin equation for solids. II. Stochastic boundary conditions for nonequilibrium molecular dynamics simulations. *Physical Review B*, 78(9):094305, 2008.
- [84] D. Toton, C. D. Lorenz, N. Rompotis, N. Martsinovich, and L. Kantorovich. Temperature control in molecular dynamic simulations of non-equilibrium processes. *Journal of Physics: Condensed Matter*, 22(7):074205, 2010.
- [85] S. T. Cui, S. A. Gupta, P. T. Cummings, and H. D. Cochran. Molecular dynamics simulations of the rheology of normal decane, hexadecane, and tetracosane. *The Journal of Chemical Physics*, 105(3):1214–1220, 1996.
- [86] A. Jabbarzadeh, J. D. Atkinson, and R. I. Tanner. Effect of the wall roughness on slip and rheological properties of hexadecane in molecular dynamics simulation of Couette shear flow between two sinusoidal walls. *Phys. Rev. E*, 61(1):690–699, 2000.
- [87] J. Gao, W. Luedtke, and U. Landman. Structures, solvation forces and shear of molecular films in a rough nano-confinement. *Tribology Letters*, 9(1):3–13, 2000.
- [88] M. J. Stevens, M. Mondello, G. S. Grest, S. T. Cui, H. D. Cochran, and P. T. Cummings. Comparison of shear flow of hexadecane in a confined geometry and in bulk. *The Journal of Chemical Physics*, 106(17):7303–7314, 1997.
- [89] T. K. Xia, J. Ouyang, M. W. Ribarsky, and U. Landman. Interfacial alkane films. *Phys. Rev. Lett.*, 69(13):1967–1970, 1992.
- [90] A. Ulman. Formation and structure of self-assembled monolayers. *Chemical Reviews*, 96(4):1533–1554, 1996.

- [91] J. J. Monaghan. Smoothed particle hydrodynamics. *Rep. Prog. Phys.*, 68:1703, 2005.
- [92] J.-M. Belley, P. Belley, F. Colin, and R. Egli. Non-smooth kernels for meshfree methods in fluid dynamics. *Comput. Math. Appl.*, 58:1253, 2009.
- [93] C. J. Fennell and J. D. Gezelter. Is the Ewald summation still necessary? Pairwise alternatives to the accepted standard for long-range electrostatics. *J. Chem. Phys.*, 124:234104, 2006.
- [94] M. Unser. Splines: A perfect fit for signal and image processing. *IEEE Signal Processing Mag.*, 16:22, 1999.
- [95] F. M. Richards. Areas, volumes, packing, and protein structure. *Annual Review of Biophysics and Bioengineering*, 6(1):151–176, 1977.
- [96] N. Voss, M. Gerstein, T. Steitz, and P. Moore. The geometry of the ribosomal polypeptide exit tunnel. *Journal of Molecular Biology*, 360(4):893–906, 2006.
- [97] H. Breu, J. Gil, D. Kirkpatrick, and M. Werman. Linear time Euclidean distance transform algorithms. *Pattern Analysis and Machine Intelligence, IEEE Transactions on*, 17(5):529–533, 1995.
- [98] A. Okabe, B. Boots, K. Sugihara, and S. N. Chiu. *Spatial Tessellations: Concepts and Applications of Voronoi Diagrams (2nd Ed.)*. J. Wiley & Sons, Ltd, Chichester, 2000.
- [99] G. Schliecker. Structure and dynamics of cellular systems. *Adv. Phys.*, 51:1319, 2002.
- [100] M. P. Marder. *Condensed Matter Physics*. J. Wiley & Sons, Inc., New York, 2000.
- [101] P. F. B. Goncalves and H. Stassen. Free energy of solvation from molecular dynamics simulation applying Voronoi-Delaunay triangulation to the cavity creation. *J. Chem. Phys.*, 123:214109, 2005.
- [102] L. T. Kong, G. Bartels, C. C. ná, C. Denniston, and M. H. Müser. Implementation of Green’s function molecular dynamics: An extension to LAMMPS. *Computer Physics Communications*, 180(6):1004, 2009.
- [103] K. B. Howell. *Transforms and Applications Handbook*, chapter 2, page 95. CRC and IEEE Press, Boca Raton, 1996.
- [104] S. Mallat. *A Wavelet Tour of Signal Processing, Second Edition (Wavelet Analysis & Its Applications)*. Academic Press, 1999.

- [105] J. Gao, W. D. Luedtke, D. Gourdon, M. Ruths, J. N. Israelachvili, and U. Landman. Frictional forces and Amontons' law: From the molecular to the macroscopic scale. *The Journal of Physical Chemistry B*, 108(11):3410–3425, 2004.
- [106] Y. Mo and I. Szlufarska. Roughness picture of friction in dry nanoscale contacts. *Phys. Rev. B*, 81:035405, 2010.
- [107] M. J. Brukman, G. Oncins, T. D. Dunbar, L. D. Boardman, and R. W. Carpick. Nanotribological properties of alkanephosphonic acid self-assembled monolayers on aluminum oxide: Effects of fluorination and substrate crystallinity. *Langmuir*, 22(9):3988–3998, 2006.
- [108] M. Ruths. Boundary friction of aromatic self-assembled monolayers: Comparison of systems with one or both sliding surfaces covered with a thiol monolayer. *Langmuir*, 19:6788, 2003.
- [109] T. J. Colburn and G. Leggett. Influence of solvent environment and tip chemistry on the contact mechanics of tip-sample interactions in friction force microscopy of self-assembled monolayers of mercaptoundecanoic acid and dodecanethiol. *Langmuir*, 23:4959, 2007.
- [110] E. Barthel. Adhesive elastic contacts: JKR and more. *J. Phys. D: Appl. Phys.*, 41:163001, 2008.
- [111] G. He and M. O. Robbins. Simulations of the kinetic friction due to adsorbed surface layers. *Tribology Letters*, 10(1):7–14, 2001.
- [112] G. He, M. H. Müser, and M. O. Robbins. Adsorbed layers and the origin of static friction. *Science*, 284(5420):1650–1652, 1999.
- [113] R. W. Carpick and M. Salmeron. Scratching the surface: Fundamental investigations of tribology with atomic force microscopy. *Chem. Rev.*, 97:1163, 1997.
- [114] G. He and M. O. Robbins. Simulations of the static friction due to adsorbed molecules. *Phys. Rev. B*, 64(3):035413, 2001.
- [115] W. H. Press, S. A. Teukolsky, W. T. Vetterling, and B. P. Flannery. *Numerical Recipes: The Art of Scientific Computing (3rd Ed.)*. Cambridge University Press, Cambridge, 2007.
- [116] P. H. Hünenberger, A. E. Mark, and W. F. V. Gunsteren. Fluctuation and cross-correlation analysis of protein motions observed in nanosecond molecular dynamics simulations. *J. Mol. Biol.*, 252:492, 1995.
- [117] M. Laberge and T. Yonetani. Molecular dynamics simulations of hemoglobin a in different states and bound to DPG: Effector-linked perturbation of tertiary conformations and HbA concerted dynamics. *Biophys. J.*, 94:2737, 2008.

- [118] O. F. Lange and H. Grubmüller. Generalized correlation for biomolecular dynamics. *Proteins Struct. Funct. Bioinf.*, 62:1053, 2006.
- [119] G. E. Arnold and R. L. Ornstein. Molecular dynamics study of time-correlated protein domain motions and molecular flexibility: Cytochrome P450BM-3. *Biophys. J.*, 73:1147, 1997.
- [120] J. Carlsson and J. Åqvist. Absolute and relative entropies from computer simulation with applications to ligand binding. *J. Phys. Chem. B*, 109:6448, 2005.
- [121] P. H. Nguyen. Estimating configurational entropy of complex molecules: A novel variable transformation approach. *Chem. Phys. Lett.*, 468:90, 2009.
- [122] T. Lazaridis, A. Masunov, and F. Gandolfo. Contributions to the binding free energy of ligands to avidin and streptavidin. *Proteins Struct. Funct. Bioinf.*, 47:194, 2002.
- [123] C. W. Gardiner. *Handbook of Stochastic Methods for Physics, Chemistry and the Natural Sciences*. Springer Verlag, Berlin, 2004.
- [124] J. Carlsson and J. Åqvist. Calculations of solute and solvent entropies from molecular dynamics simulations. *Phys. Chem. Chem. Phys.*, 8:5385, 2006.
- [125] H. Schäfer, A. E. Mark, and W. F. V. Gunsteren. Absolute entropies from molecular dynamics simulation trajectories. *J. Chem. Phys.*, 113:7809, 2000.
- [126] H. Meirovitch. Recent developments in methodologies for calculating the entropy and free energy of biological systems by computer simulation. *Curr. Opin. Struct. Biol.*, 17:181, 2007.
- [127] G. G. Maisuradze, A. Liwo, and H. A. Scheraga. Principal component analysis for protein folding dynamics. *J. Mol. Biol.*, 385:312, 2009.
- [128] I. Andricioaei and M. Karplus. On the calculation of entropy from covariance matrices of the atomic fluctuations. *J. Chem. Phys.*, 115:6289, 2001.
- [129] J. Schlitter. Estimation of absolute and relative entropies of macromolecules using the covariance matrix. *Chem. Phys. Lett.*, 215:617, 1993.
- [130] H. Schäfer, X. Daura, A. E. Mark, and W. F. V. Gunsteren. Entropy calculations on a reversibly folding peptide: Changes in solute free energy cannot explain folding behavior. *Proteins Struct. Funct. Genetics*, 43:45, 2001.
- [131] A. L. Tournier and J. C. Smith. Principal components of the protein dynamical transition. *Phys. Rev. Lett.*, 91:208106, 2003.

- [132] S.-T. D. Hsu, C. Peter, W. F. V. Gunsteren, and A. M. J. J. Bonvin. Entropy calculation of HIV-1 env gp120, its receptor CD4, and their complex: An analysis of configurational entropy changes upon complexation. *Biophys. J.*, 88:15, 2005.
- [133] B. Luan and M. O. Robbins. The breakdown of continuum models for mechanical contacts. *Nature*, 435:929, 2005.
- [134] K. Busuttil, N. Nikogeorgos, Z. Zhang, M. Geoghegan, C. A. Hunter, and G. J. Leggett. The mechanics of nanometre-scale molecular contacts. *Faraday Discuss.* 156, 2012. DOI:10.1039/C2FD00133K
- [135] W. L. Jorgensen. *BOSS, Version 4.6, Biochemical and Organic Simulation System Users Manual*. Department of Chemistry, Yale University, 2004.

List of Publications

Papers in reviewed journals

1. A. Vernes, S. Eder, G. Vorlaufer, and G. Betz, “On the three-term kinetic friction law in nanotribological systems,” *Faraday Discuss.* 156, 2012. DOI:10.1039/C2FD00120A
2. S. Eder, A. Vernes, G. Vorlaufer, and G. Betz, “Molecular Dynamics Simulations of Mixed Lubrication with Smooth Particle Post-Processing,” *J. Phys.: Condens. Matter*, vol. 23, 175004, 2011. DOI: 10.1088/0953-8984/23/17/175004

Invited talks

1. S. Eder, “Simulation in der Tribologie,” Lecture at *International Summer School Lower Austria “Nanotechnologie & Virtual Reality,”* Waidhofen/Ybbs, 24–29 July 2011.
2. S. Eder, “Simulation mit Atomen,” Hands-on tutorial at *International Summer School Lower Austria “Nanotechnologie & Virtual Reality,”* Waidhofen/Ybbs, 24–29 July 2011.
3. S. Eder, S. Ilincic and G. Vorlaufer, “Numerical modelling of lubricated frictional tribocontacts on the micro- and nanoscale,” *17th International Colloquium Tribology—TAE*, Ostfildern (D), 19–21 Januray 2010. Conference Proceedings, p. 10.

Conference contributions

1. A. Vernes, S. Eder, G. Vorlaufer, and G. Betz, “On the three-term kinetic friction law in nanotribological systems,” *Faraday Discussions 156*, Southampton (UK), 2–4 April 2012.

2. S. Eder, A. Vernes, G. Vorlaufer, and G. Betz, "A post-processing tool for mapping molecular dynamics to continuum," in *38th Leeds-Lyon Symposium on Tribology*, Lyon (F), 6–9 September 2011. Book of Abstracts, p. XXX (ii).
3. A. Neacsu, B. Scheichl, S. Eder, and G. Vorlaufer, "Cavitation in Porous Journal Bearings Lubricated with Ionic Liquids," *ECOTRIB 2011—3rd European Conference on Tribology*, Vienna (A) 7–9 June 2011. ISBN: 978-3-901657-38-2, pp. 681–686.
4. S. Eder, A. Vernes, G. Vorlaufer, and G. Betz, "Mapping Atomistic Lubrication to Continuum via a Smooth Particle Approach," *International Nanotribology Forum, The Hoi An Discussions II*, Hoi An (Vietnam), 23–27 May 2011.
5. A. Vernes, S. Eder, G. Vorlaufer, and G. Betz, "Collective Motions of Lubricant Atoms During Sliding in Nanotribological Systems," *International Nanotribology Forum, The Hoi An Discussions II*, Hoi An (Vietnam), 23–27 May 2011.
6. S. Eder, G. Vorlaufer, A. Vernes, and G. Betz, "Identification and analysis of friction regimes due to the failure of thin lubricant films," in *Theoretical Modeling and Experimental Simulation in Tribology*, Institut d'Etudes Scientifiques de Cargèse, Cargèse (F), 22-26 March 2010. Program Booklet, p. 57.
7. A. Vernes, G. Vorlaufer, S. Ilincic, S. Eder and F. Franek, "Ab initio atomic-scale friction of graphene," in *Theoretical Modeling and Experimental Simulation in Tribology*, Institut d'Etudes Scientifiques de Cargèse, Cargèse (F), 22-26 March 2010. Program Booklet, p. 69.
8. S. Ilincic, S. Eder, G. Vorlaufer, A. Vernes and N. Tungkunagorn, "Modelling load and friction in rough tribocontacts using boundary elements and molecular dynamics," *OeTG Symposium*, St. Pölten (A), 26 November 2009. ISBN: 978-3-901657-34-4, pp. 189–194.
9. S. Eder, G. Vorlaufer, F. Franek, and G. Betz, "Molecular Dynamics Simulations of the Tribological Performance of Model Lubricant Additives," *World Tribology Congress 2009—WTC IV*, Kyoto (J), 6–9 September 2009. ISBN: 978-4-9900139-9-8; p. 623.
10. S. Eder, G. Vorlaufer, A. Pauschitz, and G. Betz, "Detailed Study of Additivated Nanotribological Contacts Using Molecular Dynamics Simulations," in *36th Leeds-Lyon Symposium on Tribology*, Lyon (F), 1–3 September 2009. Book of Abstracts, p. IV (iii).
11. S. Eder, G. Vorlaufer, and G. Betz, "Molecular dynamics simulations of boundary lubricant failure," *Advances in Boundary Lubrication and Boundary Surface Films*, Sevilla (E), 29 March – 3 April, 2009.

12. S. Eder, G. Vorlaufer, and G. Betz, “Computational nanotribology of lubricated model friction contacts,” in *35th Leeds-Lyon Symposium on Tribology*, Leeds (UK), 9–12 September 2008. Book of Abstracts, p. XXIV (iii).
13. S. Eder, G. Vorlaufer, S. Ilincic, G. Betz, “Simulation of wear processes using molecular dynamics (MD) simulations,” *OeTG Symposium*, St. Pölten (A), 22 November 2007. ISBN: 978-3-901657-28-3, pp. 105–112.

Teaching

1. Guest lecture and tutorial, “Molecular modeling in tribology”, *Surface engineering and tribology*, FH Wiener Neustadt, 11 November and 15 December 2011.
2. Guest lectures, “Modeling in tribology” and “Classical molecular dynamics in tribology,” *Industrial simulation*, FH St. Pölten, 8 June 2011.

Curriculum Vitae

Stefan Eder

BORN: 27.04.1978 in Vienna, Austria
ADDRESS: Graf Starhemberg Gasse 29/23
1040 Vienna
Austria
PHONE: +43 650 314 88 00
E-MAIL: stefan.j.eder@gmail.com

Education

JANUARY 2004	TECHNICAL PHYSICS DEGREE Diploma Program (Dipl.-Ing.), The Faculty of Technology and Natural Sciences, Vienna University of Technology, Austria
JUNE 1996	HIGH SCHOOL DIPLOMA BG XIII, Fichtnergasse 15, Vienna, Austria

Professional experience

APR. 2007 to present	RESEARCHER, AC ² T research GmbH, Viktor-Kaplan-Straße 2, 2700 Wr. Neustadt, Austria
FEB. 2004 to JAN. 2007	FREELANCE RESEARCHER, KfV, Austrian Road Safety Board, Schleiergasse 18, 1100 Vienna, Austria